

**University of Alberta**

Protection and Power Quality Impact of Distributed Generation on  
Distribution System

by

Hesam Yazdanpanahi

A thesis submitted to the Faculty of Graduate Studies and Research  
in partial fulfillment of the requirements for the degree of

Doctor of Philosophy

in

Power Engineering and Power Electronics

Department of Electrical and Computer Engineering

©Hesam Yazdanpanahi

Spring 2014

Edmonton, Alberta

Permission is hereby granted to the University of Alberta Libraries to reproduce single copies of this thesis and to lend or sell such copies for private, scholarly or scientific research purposes only. Where the thesis is converted to, or otherwise made available in digital form, the University of Alberta will advise potential users of the thesis of these terms.

The author reserves all other publication and other rights in association with the copyright in the thesis and, except as herein before provided, neither the thesis nor any substantial portion thereof may be printed or otherwise reproduced in any material form whatsoever without the author's prior written permission.

## **Abstract**

Distributed Generation (DG) units are relatively small generation plants directly connected to the distribution networks as alternatives for bulky power plants and to integrate renewable energy sources into the power system. Despite their several advantages, DGs have a serious impact on the distribution system. In this thesis, the main focus is on the DGs' impact on the Over-Current (O.C.) protection system's coordination and also on the power quality.

DGs are known to contribute fault currents to their interconnected power system. As a result, DGs may affect the coordination of O.C. protection in a distribution system. This problem is expected to become more acute as industry is moving towards requiring DGs to stay connected during faults (i.e., requiring low voltage ride through capability). This thesis presents its findings on the contributions of DGs to fault currents and their probable impact on the O.C. protection coordination. This thesis also presents techniques to mitigate the impact of Inverter-Based DGs (IBDGs) and Synchronous Machine DGs (SMDGs), as their impact on the O.C. protection, especially for marginal coordination, is more significant than that of other types of DG.

In the discussion of the DG's impact on the power quality, the main focus is on the harmonic modelling and analysis of Doubly-Fed Induction Generator (DFIG)-based wind farms. An accurate modeling method is proposed in this thesis. Also, the harmonic emissions of these DGs are compared to the limits

determined by power quality standards. The findings show that the harmonic emissions of DFIG-based wind farms are too low to concern utility operators.

## Table of Contents

<b>CHAPTER 1</b>	<b>INTRODUCTION</b> .....	<b>1</b>
1.1	DISTRIBUTED GENERATION (DG).....	1
1.2	DG TYPES.....	2
1.3	DGs’ IMPACT ON DISTRIBUTION SYSTEM.....	3
1.3.1	<i>DGs’ impact on the O.C. protection system</i> .....	3
1.3.2	<i>DGs’ impact on power quality</i> .....	6
1.4	THESIS SCOPES AND OUTLINE.....	6
1.5	RESEARCH CONTRIBUTION.....	7
<b>CHAPTER 2</b>	<b>IMPACT OF DG ON THE OVER-CURRENT (O.C.) PROTECTION</b> .....	<b>10</b>
2.1	MISCOORDINATION BETWEEN MAIN AND BACK-UP PROTECTION.....	10
2.2	FAILURE IN FUSE SAVING SCHEME.....	12
2.3	FALSE TRIPPING.....	13
2.4	DESENSITIZATION (REDUCTION IN REACH).....	13
2.5	CONCLUSION.....	14
<b>CHAPTER 3</b>	<b>IMPACT OF INVERTER-BASED DGS ON O.C. PROTECTION</b> .....	<b>15</b>
3.1	INVERTERS’ CONTROL STRATEGIES.....	15
3.1.1	<i>Voltage-controlled voltage source inverters</i> .....	15
3.1.2	<i>Current-controlled voltage source inverters</i> .....	16
3.2	INVERTERS’ O.C. PROTECTION.....	17
3.2.1	<i>DG trip</i> .....	17
3.2.2	<i>Current limiting protection</i> .....	18
3.3	CONTRIBUTION OF IBDGS TO FAULT CURRENT.....	19
3.4	IMPACT OF DG ON FUSE-RECLOSER COORDINATION.....	21
3.5	THE PROPOSED STRATEGY.....	26
3.6	SIMULATION RESULTS.....	28
3.6.1	<i>Performance during low impedance faults</i> .....	28
3.6.2	<i>Performance during high impedance faults</i> .....	35
3.6.3	<i>Performance during non-fault disturbances</i> .....	36
3.7	CONCLUSION.....	39
<b>CHAPTER 4</b>	<b>IMPACT OF SYNCHRONOUS-MACHINE DGS ON O.C. PROTECTION</b> .....	<b>41</b>
4.1	OPERATIONAL REACTANCES AND TIME CONSTANTS.....	43

4.2	SYNCHRONOUS GENERATOR'S FAULT CURRENT .....	46
4.3	CASE STUDIES .....	49
4.3.1	<i>Impact on the main and back-up protection coordination</i> .....	49
4.3.2	<i>Impact on fuse-saving scheme</i> .....	52
4.4	IDEA OF UTILIZING FIELD DISCHARGE CIRCUIT.....	54
4.5	DETAILED ANALYSIS .....	59
4.6	FIELD DISCHARGE CIRCUIT DESIGN PROCEDURE .....	70
4.6.1	<i>Field discharge resistance</i> .....	71
4.6.2	<i>Current and voltage ratings of solid state switches</i> .....	73
4.6.3	<i>Grid fault detection</i> .....	74
4.7	MITIGATION OF SMDG'S IMPACT ON COORDINATION: CASE STUDIES .....	75
4.7.1	<i>Case I: Field discharge circuit design</i> .....	75
4.7.2	<i>Case II: main and back-up relays coordination</i> .....	77
4.7.3	<i>Case III: Fuse-recloser coordination</i> .....	78
4.8	IMPACT OF FIELD DISCHARGE ON VOLTAGE RECOVERY .....	79
4.9	IMPACT OF FIELD DISCHARGE ON GENERATOR'S STABILITY .....	85
4.10	CONCLUSION .....	89
<b>CHAPTER 5 HARMONIC ANALYSIS OF DFIG-BASED WIND FARMS .....</b>		<b>91</b>
5.1	METHODOLOGY.....	92
5.2	SINUSOIDAL PWM SWITCHING TECHNIQUE.....	96
5.3	HARMONIC MODELLING OF DFIG SYSTEM .....	99
5.3.1	<i>Harmonic modelling of GSC</i> .....	100
5.3.2	<i>Harmonic modelling of RSC</i> .....	101
5.4	SIMULATION.....	102
5.4.1	<i>Simulated system</i> .....	102
5.4.2	<i>Simulation results</i> .....	104
5.4.3	<i>Comparison of the results</i> .....	109
5.5	ESTIMATION OF PARAMETERS .....	111
5.5.1	<i>Stator and rotor powers</i> .....	111
5.5.2	<i>Estimation of <math>V_{ac}</math> and <math>M_{GSC}</math></i> .....	113
5.5.3	<i>Estimation of <math>M_{RSC}</math></i> .....	114
5.6	ILLUSTRATIVE EXAMPLE .....	115
5.6.1	<i>Study scenario</i> .....	115
5.6.2	<i>Example</i> .....	116
5.7	NON-CHARACTERISTIC HARMONICS .....	118
5.8	COMPARISON WITH OTHER HARMONIC SOURCES AND STANDARDS .....	120
5.9	CONCLUSION.....	123

<b>CHAPTER 6</b>	<b>CONCLUSIONS AND FUTURE WORK.....</b>	<b>125</b>
6.1	THESIS CONCLUSIONS AND CONTRIBUTIONS.....	125
6.2	SUGGESTIONS FOR FUTURE WORK .....	127
<b>CHAPTER 7</b>	<b>REFERENCES .....</b>	<b>129</b>
<b>APPENDIX A: FAULT CURRENT CONTRIBUTION OF INDUCTION-MACHINE</b>		
<b>DGS</b>	<b>.....</b>	<b>138</b>
A.1	INDUCTION GENERATOR'S FAULT CURRENT .....	138
A.1.1	<i>Singly-Fed Induction Generator (SFIG)</i> .....	139
A.1.2	<i>Doubly-Fed Induction Generator (DFIG)</i> .....	144
A.2	FINDINGS FROM AN EXPERIMENTAL RESEARCH WORK.....	146
A.3	IMPACT ON THE PROTECTION COORDINATION.....	147
A.3.1	PHASE-TO-PHASE FAULTS.....	148
A.3.2	PHASE-TO-GROUND FAULTS .....	149
A.4	CONCLUSION .....	150
<b>APPENDIX B: FAULT CURRENT CONTRIBUTION OF PERMANENT MAGNET</b>		
<b>SYNCHRONOUS GENERATORS .....</b>		
B.1	PMSG'S FAULT CURRENT .....	153
B.2	COMPARISON OF PMSG'S AND WFSG'S FAULT CURRENTS .....	154
B.3	ESTIMATION OF PMSG'S CONTRIBUTION TO FAULT .....	157
B.4	LIMITING PMSG'S FAULT CURRENT.....	158
B.4.1	<i>PM machines with large leakage inductance</i> .....	159
B.4.2	<i>PM machines with auxiliary excitation</i> .....	160
B.4.3	<i>PM machines with mechanically adjustable flux</i> .....	163
B.5	CONCLUSION .....	165
<b>REFERENCES OF APPENDICES.....</b>		<b>167</b>

# List of Tables

Table 3-1: IEEE std. 1547 required response to abnormal voltage conditions.....	27
Table 3-2: Test system parameters .....	37
Table 3-3: Induction machine's parameters.....	37
Table 4-1: Comparison of impedance estimation method with data-based single-point problem [61] .....	46
Table 4-2: Loads and their power factors .....	50
Table 4-3: Relays' settings.....	51
Table 4-4: Fault currents and relays' operation times.....	51
Table 4-5: Operational constants of simulated synchronous machine [62] .....	51
Table 4-6: Sections' lengths.....	53
Table 4-7: Loads and their power factors .....	53
Table 4-8: Field discharge switches' ratings.....	74
Table 4-9: Switches' ratings in the studied case .....	76
Table 4-10: The relays' currents and operation times for fault at F3 and 6.5MW DG.....	78
Table 4-11: CCT for 3-phase solid fault at different busses .....	89
Table 5-1: Sample spectrum for background harmonic voltages in Scenario 1 ...	94
Table 5-2: $V_h/V_{dc}$ in PWM technique with large odd $m_f$ multiple of 3.....	99
Table 5-3: $V_h$ in PWM technique with $m_f = 45$ , $f_{sw} = 2.7\text{kHz}$ , $M = .8$ and $V_{dc} = 1150\text{V}$ .....	101
Table 5-4: Major harmonic components of GSC current .....	107
Table 5-5: Major harmonic components of RSC current.....	107
Table 5-6: Harmonic components at 2580 Hz .....	110
Table 5-7: Harmonic components at 3300 Hz .....	111
Table 5-8: Major harmonic components the example in the worst condition ....	118
Table 5-9: Normalized spectrum of harmonic sources .....	121
Table 5-10: Comparison of the farm's harmonic currents with the limits of IEEE Std. 1547 .....	122

Table 5-11: Comparison of the farm’s harmonic voltages with the limits of IEC  
61000-3 ..... 122

# List of Figures

Figure 1-1: Comparison of power networks: (a) Traditional network, (b) Network with DG.....	2
Figure 1-2: Proposed WECC LVRT standard [14].....	5
Figure 2-1: Sample distribution feeder with main and back-up protection .....	11
Figure 2-2: Time-current characteristic curves of main and back-up devices of Figure 2-1 .....	11
Figure 2-3: Typical response time of O.C. devices versus fault current [21].....	12
Figure 2-4: Impact of the DG on the fuse-recloser coordination .....	13
Figure 2-5: False tripping due to DG's response to fault at adjacent feeder [23].	13
Figure 2-6: Desensitization or reduction in reach. ....	14
Figure 3-1: Voltage-controlled voltage source inverter with its control blocks ...	16
Figure 3-2: Equivalent circuit of voltage-controlled voltage source inverter [27]	16
Figure 3-3: Current-controlled voltage source inverter with its control blocks....	17
Figure 3-4: Equivalent circuit of current-controlled voltage source inverter [27]	17
Figure 3-5: Typical inverter's RMS current during the fault (trip protection) .....	18
Figure 3-6: Typical inverter's RMS current during the fault (current limiting protection) .....	18
Figure 3-7: Response of a commercial inverter with current limiting protection to 3-phase fault [33] .....	20
Figure 3-8: Response of another commercial inverter with current limiting protection to 3-phase fault [[33].....	20
Figure 3-9: Response of inverter with current limiting protection proposed in [31] to 3-phase fault.....	21
Figure 3-10: Fuse-Recloser protection scheme in distribution feeders .....	22
Figure 3-11: Fuse-Recloser time-current characteristic curves .....	22
Figure 3-12: Impact of DG on operation of protection system under low impedance fault situation .....	22
Figure 3-13: Equivalent circuit of a distribution system with inverter-based DG, during a downstream fault. ....	23

Figure 3-14: Voltage and current vector diagram of: a) DG provides active power, b) DG provides reactive power. ....	26
Figure 3-15: Proposed strategy to determine inverter reference current .....	28
Figure 3-16: IEEE 13-Node test feeder system [40].....	29
Figure 3-17: Fuse-recloser coordination in the simulated system .....	29
Figure 3-18: Difference between fuse and recloser operation time after adding DG for 0.01 Ohm fault.....	30
Figure 3-19: Difference between fuse and recloser operation time after adding DG for 0.1 Ohm fault.....	30
Figure 3-20: Intentional phase shift in DG current during voltage sag to support voltage.....	32
Figure 3-21: Difference between fuse and recloser operation time for 0.01 Ohm fault with $\pi/2$ phase shift in inverter current.....	32
Figure 3-22: Difference between fuse and recloser operation time for 0.1 Ohm fault with $\pi/2$ phase shift in inverter current.....	32
Figure 3-23: Difference between fuse and recloser operation time for 0.2 Ohm fault with $\pi/2$ phase shift in inverter current.....	32
Figure 3-24: Difference between fuse and recloser operation time for 0.01 Ohm fault with inverter current reduction control.....	33
Figure 3-25: PCC voltage for 0.01 Ohm fault with DG at 30% penetration level.	33
Figure 3-26: DG output current for 0.01 Ohm fault with DG at 30% penetration level.....	33
Figure 3-27: Fuse current for 0.01 Ohm fault with DG at 30% penetration level.	33
Figure 3-28: Output current of inverter installed at Node 634. ....	34
Figure 3-29: Output current of inverter installed at Node 634. ....	34
Figure 3-30: Fuse current for 1 Ohm fault with DG units at Nodes 634 and 675.	34
Figure 3-31: Output current of inverters for 2-Ohm fault in the middle of 645-646. .....	35
Figure 3-32: Inverter output power for 8-Ohm fault in the middle of 645-646....	35
Figure 3-33: PCC voltage for 8-Ohm fault in the middle of 645-646. ....	36
Figure 3-34: Fuse current for 8-Ohm fault in the middle of 645-646.....	36

Figure 3-35: A distribution network with fuse-saving protection. ....	37
Figure 3-36: A distribution network with fuse-saving protection. ....	38
Figure 3-37: DG output power during motor starting for both traditional and proposed control strategies.....	38
Figure 3-38: Voltage at terminals of IM during motor starting for both traditional and proposed control strategies.....	38
Figure 3-39: Inverter output current during the motor starting transient.....	39
Figure 4-1: SMDG control strategies during grid fault .....	43
Figure 4-2: Synchronous generator's structure .....	44
Figure 4-3: Equivalent synchronous machine with fictitious $d$ - and $q$ -axis windings .....	44
Figure 4-4: Typical synchronous generator's fault current: (a) Complete waveform, (b) first 18 cycles .....	49
Figure 4-5: Single-line diagram of the studied case .....	50
Figure 4-6: Fault current at F3 when a 5MW SMDG is added at substation .....	52
Figure 4-7: Impact of 6.5MW SMDG on relays' operation points.....	52
Figure 4-8: Single-line diagram of sample network .....	52
Figure 4-9: fuse and recloser time-current characteristics curves.....	54
Figure 4-10: Fuse and recloser fault current when a 1600kW SMDG is added at bus 1 .....	54
Figure 4-11: Impact of a 2400kW SMDG on coordination .....	54
Figure 4-12: A synchronous generator with its field discharge circuit.....	56
Figure 4-13: A sample distribution network with synchronous-machine DG .....	57
Figure 4-14: RMS of machine's output current during 3-phase fault at point F ..	57
Figure 4-15: RMS of ac component of machine's output current during 3-phase fault at point F.....	58
Figure 4-16: RMS of machine's output current during 1-phase fault at point F ..	58
Figure 4-17: RMS of ac component of machine's output current during 1-phase fault at point F .....	59
Figure 4-18: Voltage which appears at the field winding during the fault .....	59

Figure 4-19: Synchronous generator's fault current with short circuited field winding, (a) Complete waveform, (b) first 18 cycles .....	62
Figure 4-20: Synchronous generator's fault current with discharge resistance in series with field winding, (a) Complete waveform, (b) first 6 cycles.....	63
Figure 4-21: Accurate estimation of the synchronous generator's fault current with a discharge resistance in series with its field .....	64
Figure 4-22: Synchronous generator's fault current with field discharge operation, (a) Complete waveform, (b) first 9 cycles .....	66
Figure 4-23: A sample distribution feeder with SMDG .....	67
Figure 4-24: RMS ac component of generator's fault current with field discharge operation in the system shown in Figure 4-21 .....	67
Figure 4-25: Reduction in synchronous generator's RMS ac component of fault current due to applying field discharge.....	68
Figure 4-26: Reduction in generator's RMS ac component of fault current for different values of field discharge resistance.....	69
Figure 4-27: Fault current components of synchronous generator, (a) When traditional excitation is applied, (b) when field discharge is applied.....	70
Figure 4-28: Synchronous generator's field current during the three-phase fault at its terminals, with field discharge circuit operation.....	72
Figure 4-29: Rotor's circuit during field discharge circuit operation .....	73
Figure 4-30: Field's current derivative for three different grid disturbances .....	75
Figure 4-31: Field winding's maximum voltage due to discharge circuit operation .....	76
Figure 4-32: Effect of field discharge circuit on eliminating the impact of a 6.5MW SMDG.....	78
Figure 4-33: Fuse and recloser fault current when a 1600kW DG is added at bus 1 .....	79
Figure 4-34: Effect of field discharge circuit to eliminate the impact of a 2400kW DG on coordination.....	79
Figure 4-35: Impact of field discharge on reactive power consumption during and after fault.....	80

Figure 4-36: Impact of field discharge on voltage recovery .....	80
Figure 4-37: A distribution feeder with DG located close to the source .....	81
Figure 4-38: A distribution feeder with DG located far from the source .....	81
Figure 4-39: Reactive power recovery .....	81
Figure 4-40: Terminal voltage recovery .....	82
Figure 4-41: d-axis flux .....	82
Figure 4-42: d-axis flux .....	82
Figure 4-43: SMDG with modified field discharge circuit.....	83
Figure 4-44: Reactive power recovery .....	84
Figure 4-45: Terminal voltage recovery .....	84
Figure 4-46: d-axis flux .....	84
Figure 4-47: Output current .....	85
Figure 4-48: Exciter voltage .....	85
Figure 4-49: Sample distribution network simulated for stability studies .....	86
Figure 4-50: Generator's output current and rotor angle deviation for .1 sec. 3- phase fault at terminals .....	87
Figure 4-51: Generator's <i>d</i> -axis flux during and after fault.....	87
Figure 4-52: Generator's output power and rotor angle deviation for .2 sec. 3- phase fault 8.1 km away from generator.....	88
Figure 5-1: DFIG-based wind farm structure .....	92
Figure 5-2: DFIG's equivalent circuit at fundamental frequency.....	92
Figure 5-3: DFIG's equivalent circuit for harmonic analysis.....	93
Figure 5-4: DC link voltage .....	95
Figure 5-5: Zoomed DC link voltage.....	95
Figure 5-6: Spectrum of DC link voltage .....	95
Figure 5-7: Spectrum of DC link voltage in lower frequencies.....	95
Figure 5-8: Integer harmonics of GSC's terminal voltage.....	96
Figure 5-9: Three-phase voltage source converter's structure.....	97
Figure 5-10: Carrier and reference signals in 3-phase sinusoidal PWM scheme .	97
Figure 5-11: Switching states of S1 during a period.....	97
Figure 5-12: Line-line voltages at converter's terminals.....	97

Figure 5-13: Harmonic spectrum of a 3-phase sinusoidal PWM switching [76] .	99
Figure 5-14: Harmonic modelling of GSC at its $h_{th}$ harmonic.....	100
Figure 5-15: DFIG's equivalent circuit at $h_{th}$ harmonic frequency.....	102
Figure 5-16: Harmonic modelling of RSC at its $h_{th}$ harmonic.....	102
Figure 5-17: Simulated power system .....	103
Figure 5-18: Details of wind farm simulation.....	103
Figure 5-19: DC link voltage .....	105
Figure 5-20: Harmonic spectrum of GSC's current (% of converter's fundamental current) .....	105
Figure 5-21: Harmonic spectrum of GSC's current (% of generator's fundamental current) .....	106
Figure 5-22: Harmonic spectrum of RSC's current (% of converters fundamental current, fundamental frequency=12 Hz).....	106
Figure 5-23: Harmonic spectrum of RSC's current (% of generator's fundamental current) .....	106
Figure 5-24: Harmonic spectrum of stator's current.....	108
Figure 5-25: Harmonic spectrum of $I_4$ .....	108
Figure 5-26: Harmonic spectrum of $I_5$ .....	109
Figure 5-27: Harmonic spectrum of voltage.....	109
Figure 5-28: Equivalent DFIG model .....	110
Figure 5-29: A typical $c_p$ over $\lambda$ curve .....	112
Figure 5-30: Power sharing in a loss-less DFIG system.....	112
Figure 5-31: Equivalent circuit of GSC at fundamental frequency during steady state .....	113
Figure 5-32: Normalized amplitude of $m_f$ -th harmonic for different values of M .....	115
Figure 5-33: Equivalent circuit for calculation of harmonic currents caused by GSC.....	118
Figure 5-34: Equivalent circuit for calculation of harmonic currents caused by RSC.....	118

Figure 5-35: Normalized harmonic components of voltage at GSC terminals, (a) up to 48<sup>th</sup> harmonic, (b) up to 21<sup>st</sup> harmonic..... 119

Figure 5-36: PWM reference signal of GSC..... 120

Figure 5-37: Normalized spectrum of PWM reference signal of GSC..... 120

# List of acronyms

<b>DG</b>	Distributed Generation
<b>IBDG</b>	Inverter-based Distributed Generation
<b>IMDG</b>	Induction-Machine Distributed Generation
<b>SMDG</b>	Synchronous-Machine Distributed Generation
<b>O.C.</b>	Over-Current
<b>IG</b>	Induction Generator
<b>SCIG</b>	Squirrel-Cage Induction Generator
<b>DFIG</b>	Doubly-Fed Induction Generator
<b>LG</b>	Line-to-Ground
<b>SG</b>	Synchronous Generator
<b>PMSG</b>	Permanent Magnet Synchronous Generator

# List of symbols

$v_s$	Instantaneous voltage of stator
$V_s$	RMS voltage of stator
$v_r$	Instantaneous voltage of rotor
$i_s$	Instantaneous current of stator
$i_r$	Instantaneous current of rotor
$\psi_s$	Instantaneous flux of stator
$\psi_r$	Instantaneous flux of rotor
$\omega_s$	Synchronous angular speed
$\omega_r$	Rotor's angular speed
$R_s$	Induction machine's Stator's resistance
$R_r$	Rotor's resistance
$L_s$	Stator's total inductance
$L_r$	Rotor's total inductance
$L_m$	Stator-rotor mutual inductance
$L_{s\sigma}$	Stator's leakage inductance
$L_{r\sigma}$	Rotor's leakage inductance
$L_s'$	Stator's transient inductance
$L_r'$	Rotor's transient inductance
$T_s'$	Stator's transient time constant
$T_r'$	Rotor's transient time constant
$k_s$	Stator's coupling factor
$k_r$	Rotor's coupling factor
$\alpha$	Stator voltage phase angle at fault instance
$\sigma$	Leakage factor
$R_{ext}$	External resistance
$\psi_d$	Total flux linkage of $d$ -axis
$\psi_q$	Total flux linkage of $q$ -axis
$p$	Laplace operator
$\omega_0$	Angular velocity

$R_F$	Field winding resistance
$R_a$	Synchronous machine's Stator resistance
$R_{kd}$	$d$ -axis damper winding resistance
$R_{kq}$	$q$ -axis damper winding resistance
$u_F$	Field excitation voltage
$u_d$	Instantaneous $d$ -axis machine's terminal voltage
$u_q$	Instantaneous $q$ -axis machine's terminal voltage
$U_{md}$	$d$ -axis machine's terminal voltage magnitude
$U_{mq}$	$q$ -axis machine's terminal voltage magnitude
$i_d$	$d$ -axis winding's current
$i_q$	$q$ -axis winding's current
$i_F$	Field winding's current
$i_{a,ac}$	Ac component of generator's current at phase $a$
$I_{a,ac}$	RMS of ac component of generator's current at phase $a$
$\Delta I$	Reduction in RMS of ac component of generator's fault current due to field discharge
$L_d$	$d$ -axis winding's total inductance
$L_{md}$	$d$ -axis winding's mutual inductance
$x_d(p)$	Laplace transform of $d$ -axis winding's reactance
$x_q(p)$	Laplace transform of $q$ -axis winding's reactance
$X_d$	$d$ -axis synchronous reactance
$X_q$	$q$ -axis synchronous reactance
$X_{md}$	$d$ -axis winding's mutual reactance
$X_{mq}$	$q$ -axis winding's mutual reactance
$X_{kd}$	$d$ -axis damper winding's leakage reactance
$X_{kq}$	$q$ -axis damper winding's leakage reactance
$X_a$	Armature leakage reactance
$T'_d$	$d$ -axis transient short-circuit time constant
$T''_d$	$d$ -axis sub-transient short-circuit time constant
$T'_{d0}$	$d$ -axis transient open-circuit time constant
$T''_{d0}$	$d$ -axis sub-transient open-circuit time constant

$T_q''$   $q$ -axis sub-transient short-circuit time constant

$T_{q0}''$   $q$ -axis sub-transient open-circuit time constant

$T_a$  Armature time constant

# Chapter 1

## Introduction

This chapter presents the concepts and definitions that will be frequently referred to in the rest of this thesis, the thesis objectives and outline, and the research contributions.

### 1.1 Distributed Generation (DG)

For decades, the only way to supply customers was to transmit electrical energy from bulky centralized generation plants to the distribution side via transmission lines, and then to deliver this energy to customers through distribution system. Later, Distributed Generation (DG) was introduced into utilities. DG units are relatively small generation plants with capacities lower than 30MW and are directly connected to the distribution networks. Figure 1-1 compares a traditional network with a network in which a DG is embedded. In this figure, the arrows represent the direction of the power flow.

Some of the most important advantages that DG units provide for utilities are as follows:

1. A DG is an alternative for satisfying incremental demand without any need for transmission expansion [1].
2. Since the DG is directly connected to the distribution network, the DG's current does not flow through the transmission line. Therefore, the associated losses are decreased.
3. The DG concept enable renewable energy sources such as PV, wind, and fuel cells to be integrated into the power system [2]. Such integration is a solution for universal concerns about the environment and air pollution and is an alternative for the use of limited risky fossil fuel resources.

4. DG units are capable of providing ancillary services to utilities, including voltage regulation, reactive power compensation and active filtering [3].

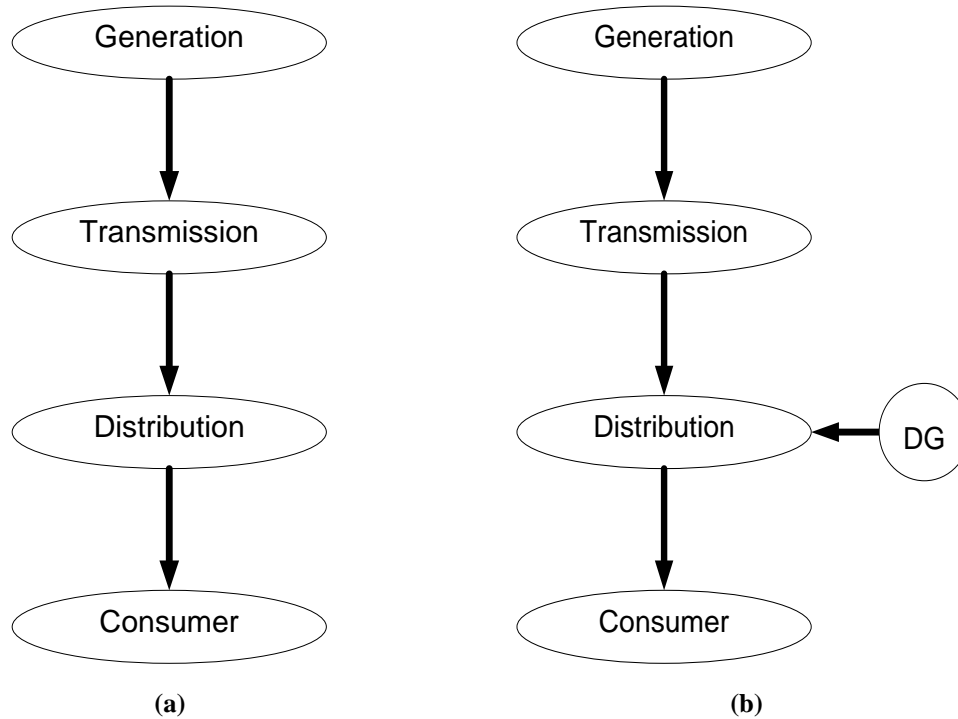


Figure 1-1: Comparison of power networks: (a) Traditional network, (b) Network with DG

## 1.2 DG types

DG units are usually categorized based on their prime movers such as Photovoltaic (PV) systems, diesel-generators, wind energy power plants, and hydro power plants. However, this categorization is not useful for this study because of the fact that the impact of DG units on the distribution system depend mainly on their size and the electrical interfaces integrating them into the network.

In this thesis, DGs are categorized into four different types:

1. Inverter-based DGs (IBDGs): These DGs deliver power to the network through a power electronic inverter and can be PV systems, microturbines, fuel cells, or full-scale converter-based wind systems.

2. Synchronous-Machine DGs (SMDGs): These DGs deliver power to the network through a synchronous generator, and the prime mover can be a diesel engine, gas turbine, hydro turbine or wind turbine.
3. Induction-Machine DGs: These DGs deliver power to the network via an induction generator, and the prime mover can be either a wind or a small hydro turbine.
4. Permanent Magnet Synchronous Generator (PMSG) DGs: In these DGs, the power is transferred to the electrical system via a PMSG. This technology has been used in some small hydro power plants.

### **1.3 DGs' impact on distribution systems**

Despite their undoubted advantages, DG systems have a negative impact on the distribution system. Each utility follows a specific guideline or standard for interconnecting DGs with the grid. Usually, these standards or guidelines include the technical specifications and requirements which a DG must satisfy. Therefore, these requirements should be considered in the study of the impact of DGs on distribution systems. In this thesis, the main focus is on the DGs' impact on the Over-Current (O.C.) protection system's coordination when Low Voltage Ride Through (LVRT) is required by the utility, and also on the DG's impact on the power quality.

#### **1.3.1 Low Voltage Ride Through**

The impact on O.C. protection is one of the most important effects of DGs on the distribution system. Before investigating this impact, one must understand the two different approaches for the DG's operation during the grid faults. In the first approach, the DG interconnection guideline or standard requires the DG to cease operation (to disconnect from the grid) when a fault happens. For example, IEEE Std. 1547 [4] requires DG disconnection within .16 Sec. for Point of Common Coupling (PCC) voltages lower than .5 per unit. Similarly, in some utility companies in Canada such as ATCO Electric [5], Manitoba Hydro [6] and ENMAX Power [7], an instantaneous DG trip is required for PCC voltages lower

than .5 per unit. In this approach, since the DG is disconnected from the grid, the DG has no contribution to the fault current and, consequently, has no impact on the O.C. protection. In fact, this approach has been practiced by many utilities ever since the DG concept was first introduced, to prevent the DG from affecting the protection.

However, after DGs penetrate significantly into some distribution systems, the use of the DG disconnection approach can lead to the disconnection of a major portion of the power generation and, consequently, can jeopardize the grid's stability. As a result, in such systems, grid codes are being modified [8], and in some high and extra-high voltage grid connection standards like [9],[10] the second approach is followed. In this approach, the distributed resources are forced to stay connected to the grid during the fault. This approach has been extended to some medium-voltage ( $1 \text{ kV} < V_{\text{rated}} < 60 \text{ kV}$ ) grids as well [11], [12] and is expected to be the main approach in other guidelines such as IEEE Std. 1547 in the near future [13]; i.e., the DG is required to stay connected during the temporary fault to help maintain grid's stability [14]. This requirement is named Low Voltage Ride Through (LVRT). Figure 1-2 [14] demonstrates the proposed 2009 Western Electricity Coordination Council (WECC) LVRT standard. As this figure reveals, in this standard, for 0% PCC voltage up to .15 Sec., the DG must stay connected to the grid. Although DGs with LVRT capability support the grid's stability, they contribute to the fault current and, consequently, impact on the O.C. protection. This impact, which will be covered in Chapter 2, can cause excessive load loss and decrease service reliability. In fact, the main objective of DG's LVRT requirement is to avoid or minimize load loss by forcing the DG to function similarly to traditional generation units by supporting grid's stability and post-fault voltage recovery. However, the conflict between LVRT and O.C. protection can eventually cause an unnecessary load loss and a decrease in reliability, two outcomes that contradict the LVRT's fundamental objective. The final goal of this thesis is to propose DG-side solutions to mitigate the conflict between DG's LVRT capability and O.C. protection coordination. Mitigating this

conflict will facilitate an increase in DG's penetration and its associated advantages without degrading the service reliability.

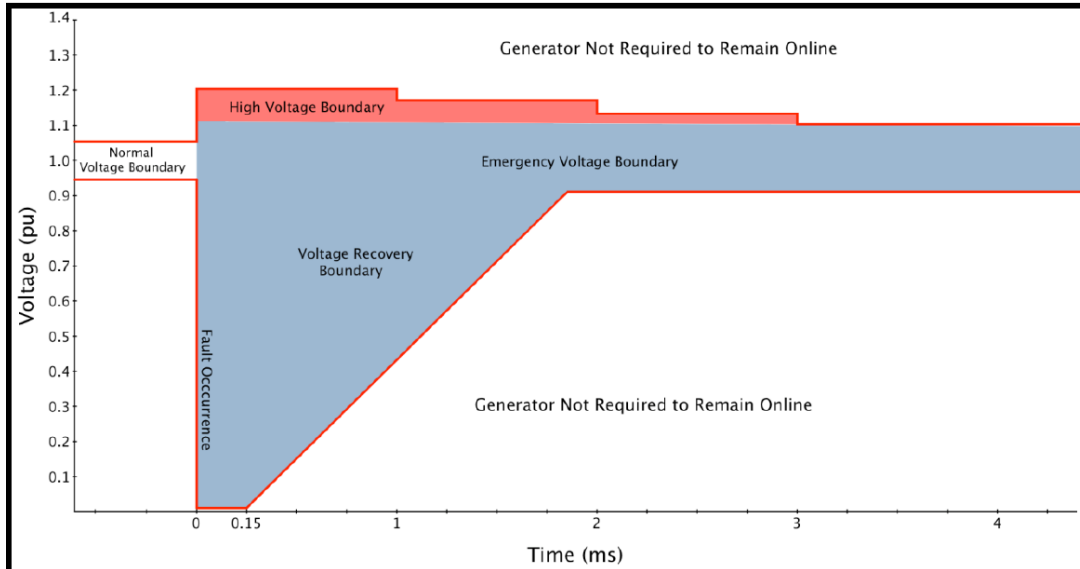


Figure 1-2: Proposed WECC LVRT standard [14]

### 1.3.2 DGs' impact on the O.C. protection system

A distribution network and its protection system are designed based on the assumptions that no generation unit is present in the network and that the network is radial. These assumptions mean that no current source is present in the distribution network; the short circuit level from the substation to the end of feeders has a descending trend; and, for a certain fault at certain location the current flows through the conductors from the substation to the fault location are the same. In addition, these assumptions also mean that the current flow is unidirectional from upstream (from the substation) to downstream. However, adding a DG to a system may violate one or more of these assumptions and, consequently, may cause serious problems in the protection system. Indeed, DGs contribute fault currents to the distribution and, consequently, may affect the coordination of O.C. protection in a distribution system. This issue becomes more critical since utilities are moving towards requiring DGs to stay connected during faults (i.e. low voltage ride through requirement).

### **1.3.3 DGs' impact on power quality**

DGs can cause different problems related to power quality, such as voltage flicker, voltage dip and introducing harmonics into the network [15]-[17]. In this thesis, we are interested in the harmonic modelling and analysis of DGs. The harmonic emissions of SMDGs, IMDG and PMSGs are negligible. In contrast, IBDGs are known as potential harmonic sources in the system. Several studies have covered this subject for full-scale inverter-interfaced DGs [18]-[20]. However, Doubly-Fed Induction Generator (DFIG) based wind farms have not been covered thoroughly. In these systems, a portion of the power is delivered through the DFIG's stator, and the rest is delivered through the inverters connected to the rotor. In this type of DG, in contrast to the other types, two harmonic sources exist. The first one, the converter at the grid side, directly injects harmonic currents into the network, and the second one, the converter connected to the DFIG's rotor, induces harmonic currents in the stator side. Moreover, these two converters share a DC link which makes the analysis more complex. Furthermore, the DFIG is currently the most often used technology in wind power generation. Consequently, the main focus is on the harmonic modelling and analysis of this type of DG.

## **1.4 Thesis objectives and outline**

One objective of this thesis is to determine the impact of different types of DGs on O.C. protection and to propose new strategies to mitigate this negative impact. This objective will be achieved in two stages:

- Investigating the contribution of each type of DG to the fault current and determining if each type can potentially impact the protection coordination.
- Proposing strategies to restrict the DGs' contribution to fault current and, consequently, to mitigate the DG's impact on the protection system's coordination when LVRT is a requirement.

Another objective of this thesis is to analyze and model the harmonic emission of DFIG-based wind farms.

The thesis is organized as follows:

Chapter 2 covers the impact of DG on O.C. protection. Chapter 3 presents our investigation on the contribution of IBDGs to the fault current and proposes a control strategy to restrict the contribution so that the DG does not impact the coordination. The contribution of SMDGs to fault current is presented in Chapter 4, and a strategy is proposed to mitigate the impact of this type of DG on the protection system by limiting the DG's contribution. Harmonic analysis and modelling of DFIG-based wind farms are presented in Chapter 5, which is followed by conclusion in Chapter 6. Finally, Appendices A and B cover the contribution of IMDGs and PMSGs, respectively, to fault current.

### **1.5 Research contribution**

The key research contributions of this thesis can be summarized as follows:

- A thorough investigation is conducted on inverter-based DGs' impact on O.C. protection coordination. It is shown that at high penetration levels or in the case of tight coordination, these DGs can cause miscoordination between the O.C. protection devices. To mitigate this problem, a strategy is proposed and applied to the simulated DG. In this strategy, the inverter's current is restricted to a dynamically adjusted limit. In contrast to the common practices in which a fixed pre-determined current limit is used, this limit is determined based on the severity of the abnormality. Through several case studies, it is shown that this strategy not only mitigates the impact of a inverter-based DG on O.C. protection but also facilitates the DG's ride through short-term disturbances.
- The contribution of synchronous-machine DGs to the fault current is assessed from O.C. protection coordination perspective, and it is shown that among the major DG types, these DGs make the highest contribution to the fault, which lasts long enough to cause miscoordination between O.C. protection devices. To minimize the contribution of these DGs to the fault and, consequently, to mitigate or minimize their impact on O.C. protection coordination, the idea of utilizing the field discharge circuit is

proposed in this thesis. Although field discharge has been utilized for decades, it has been used mainly to protect the synchronous generator and to accelerate the generation unit shut down. However, in this thesis, a new application is proposed for this circuit and is used to mitigate the impact of the DG on the grid. The simulation results show that a well-designed field discharge circuit can significantly increase the maximum allowable DG capacity by reducing its impact on O.C. protection coordination. In addition, a design procedure is proposed for solid-state switch-based field discharge circuits. The field discharge circuit's design procedure has been previously studied in some references. However, in previous studies, this was based on field discharge circuits with DC field breakers. Since the operation of such breakers can take up to .1 sec., they are not fast enough to be useful for the proposed application. As a result, in this thesis a design procedure is proposed for the solid-state switched-based discharge circuits. Since these circuits operate almost instantly and in contrast to the DC field breakers, the arcing phenomenon is not involved in these circuits, so the design procedure differs from those in the published studies.

- For induction-machine DGs, the contribution of different types of induction generators to the fault current is investigated through both mathematical analysis and simulation from the O.C. coordination perspective. The assessments show that the fault current contribution time of these DGs is too short to impact the coordination, so mitigation is unnecessary. As a result, this part of the research is included as an appendix.
- For PMSM DGs, which can be connected directly to the distribution system for some small hydro power plants, their contribution to the fault is assessed through both analysis and simulation. These machines are compared with the traditional wound-field synchronous generators, and it is shown that the fault response of these machines has no transient part. As a result, a machine reaches its steady state fault current only a few cycles

after the fault, and the machine's contribution to the fault current is significantly smaller than the contribution wound-field synchronous machine of the same size. In summary, in this thesis, it is shown that a well-designed PMSM is unlikely to impact on the O.C. protection coordination, and as a result, this part of the research is included as an appendix.

- Regarding the harmonic emission of DFIG-based wind farms, a method is proposed to calculate the harmonic current spectrum of a wind farm. In the proposed method, power electronic converters are replaced with the harmonic voltage sources. As a result, the equivalent circuit contains only impedances and voltage sources, so that the harmonic assessment is very easy. In this part of the thesis, in order to verify the accuracy of the proposed modeling method, a wind farm is simulated and the harmonic analysis results obtained from the simulation are compared with the results obtained from the proposed model. The comparison shows that the model is accurate, and that the assumptions on which the model's development is based are valid. In addition, the harmonic emission of the simulated wind farm is compared with the harmonic emission of more well-known harmonic sources as well as the harmonic limits determined by major power quality standards. The comparison shows that DFIG-based wind farms are not major harmonic sources and that these farms comply with the power quality standards.

## Chapter 2

# Impact of DG on the Over-Current (O.C.) protection

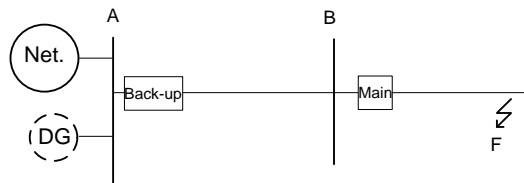
When a fault happens in the distribution system, the adjacent DGs respond to the fault. Depending on the size, type and the distance from the fault location, each DG contributes a certain amount of current in a certain window of time, and then, the DG's current decreases to zero or to a negligible level. Both the contribution level and the contribution time window should be considered during protection studies. This section presents the probable impact of DGs on the O.C. protection system and illustrates how the DGs' contribution levels and contribution time windows play a role in such an impact.

### 2.1 Miscoordination between main and back-up protection

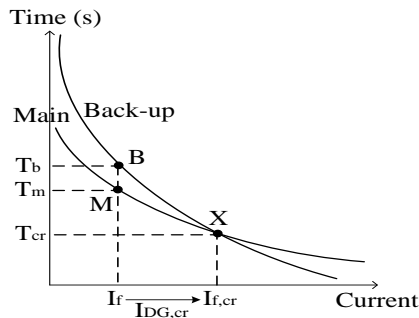
The DG's contribution to the fault current may increase the fault current, which flows through the protection devices and makes them operate faster than what was expected during the protection design. This phenomenon can cause a loss of coordination between the main and back-up protection devices; i.e. the back-up device may operate sooner than the main one. Such a miscoordination results in the undesirable de-energization of the loads located between the back-up and main protection.

Figure 2-1 shows a simple feeder with its protection devices. Figure 2-2 shows the time-current characteristic curves of these devices. When there is no DG, the fault current is equal to  $I_f$ , and, as Figure 2-2 shows, the main device operates at  $T_m$ , and the back-up device operates at  $T_b$ . However, when a DG is

embedded, its contribution to the fault current ( $I_{DG}$ ) is added to  $I_f$ . As Figure 2-2 reveals, if the DG's contribution reaches the critical amount  $I_{DG,cr}$  and remains for the critical time window  $T_{cr}$ , the main and back-up protection devices operate at the same time and cause the de-energization of the whole feeder. In other words, the contribution of the DG to the fault current slides the main and back-up protection devices' operation points from M and B, respectively, to point X in Figure 2-2. In contrast, if the DG's current is not high enough ( $I_{DG} < I_{DG,cr}$ ), the operation points remain at the left side of point X, and the main device operates faster than the back-up one (and the coordination is maintained).



**Figure 2-1: Sample distribution feeder with main and back-up protection**



**Figure 2-2: Time-current characteristic curves of main and back-up devices of Figure 2-1**

In the above system, if the DG's current is equal to (or higher than)  $I_{DG,cr}$  but vanishes sooner than the critical time window  $T_{cr}$ , the operation points of the main and back-up protection devices return from X to M and B, respectively, and the coordination is maintained. Therefore, the time window of the DG's contribution is as important as the amount of current that the DG contributes during the fault.

Figure 2-3 shows the typical characteristic curves of an O.C. device in the protection system [21]. As this figure reveals, if the contribution of the DG ends within three cycles after the beginning of the fault, it will not cause

miscoordination between any protection devices. If the DG's contribution lasts 3 to 6 cycles after the fault, it can cause miscoordination if short-time delay elements or extremely inverse relays are involved in the protection. Finally, if the contribution lasts longer than 18 cycles, it can cause miscoordination between inverse and/or very inverse O.C. relays.

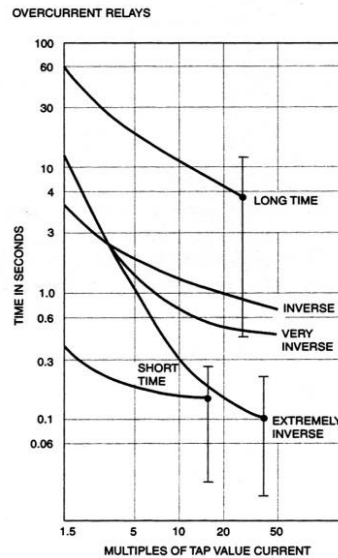


Figure 2-3: Typical response time of O.C. devices versus fault current [21]

## 2.2 Failure in the fuse-saving scheme

Fuses and reclosers are two of the main protection devices in the distribution system, and the fuse-saving scheme is one of the most commonly used schemes in distribution protection. Adding a DG may interfere with this scheme, in which the recloser is supposed to operate faster than the fuse. As Figure 2-4 shows, adding a DG increases the fault current through the fuse and makes it operate faster than the recloser. The importance of this problem has been mentioned in several publications [22]-[26]. Like the main and back-up protection coordination, the DG's contribution level and its contribution time window are key elements. A detailed analysis of this concept will be presented in 3.4.

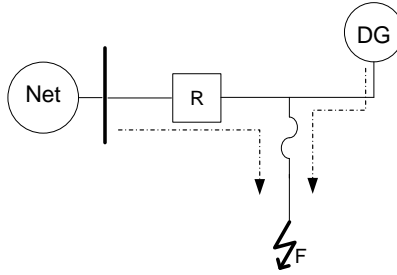


Figure 2-4: Impact of the DG on the fuse-recloser coordination

### 2.3 False tripping

Even when the fault happens on a feeder adjacent to the DG's feeder, the DG may contribute to the fault current, which flows from downstream to upstream (see Figure 2-5 [23]). As mentioned in Chapter 1, the protection system is designed based on the unidirectional current flow assumption, so, the protection device P1 is not equipped with the directional elements. Thus, if the DG's contribution is high enough and lasts long enough, P1 may operate undesirably under the condition shown in Figure 2-5 [23]. In this situation, the power delivery to the DG's feeder will be interrupted. This problem is also known as sympathetic tripping.

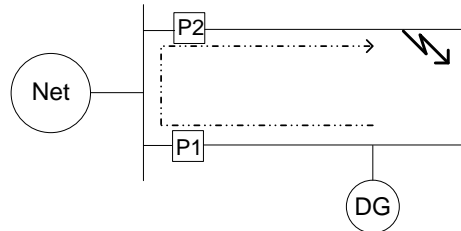


Figure 2-5: False tripping due to DG's response to fault at adjacent feeder [23]

### 2.4 Desensitization (reduction in reach)

According to Figure 2-6, the fault current through element R before and after adding the DG can be calculated by (2-1) and (2-2), respectively:

$$I_R = \frac{E1}{Z_{net} + Z_1 + (R_f + Z_2)} \quad (2-1)$$

$$I_R = \frac{E1}{Z_{net} + Z_1 + (R_f + Z_2) \parallel Z_{DG}} - \frac{E2}{Z_{DG} + (Z_1 + Z_{net}) \parallel (R_f + Z_2)} \frac{(R_f + Z_2)}{(Z_1 + Z_{net}) + (R_f + Z_2)} \quad (2-2)$$

where  $Z_{net}$  and  $Z_{DG}$  are the equivalent impedances of the upstream network and the DG, respectively;  $Z_1$  and  $Z_2$  are the impedances from the substation to the Point of Common Coupling (PCC) and from the PCC to the fault location, respectively; and  $R_f$  is the fault's resistance. The comparison between (2-1) and (2-2) reveals that, after adding the DG, the current through the protection device  $R$  decreases. This result causes protection desensitization or a reduction in reach. In other words, after adding the DG, the fault current through the feeder's main protection may be reduced below its pick-up value for certain fault resistances and, consequently, will no longer respond to these faults.

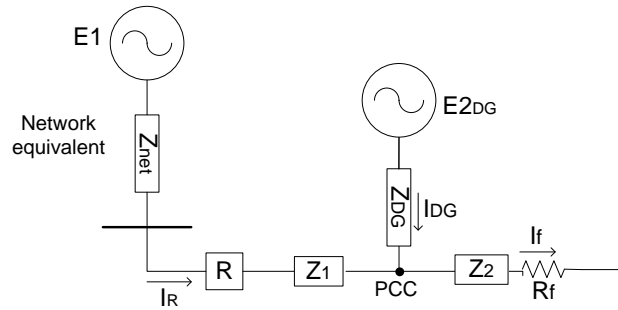


Figure 2-6: Desensitization or reduction in reach.

## 2.5 Conclusion

The potential impact of DGs on the O.C. protection were illustrated in this chapter. The example used were miscoordination between the main and back-up protection devices, failure in the fuse-saving scheme, false tripping and desensitization of the protection. Two parameters must be considered when assessing the impact of DGs on protection: the magnitude of the fault current contributed by a DG, and the time window during which the DG's fault current contribution is significant. If a DG's fault current decays to a low value before the O.C. protection can react, the DG will have little impact on protection coordination even if the DG's initial fault current contribution is large.

# Chapter 3

## Impact of Inverter-based DGs on O.C. protection

Several types of renewable resources are connected to the distribution system through the power electronics inverters. These sources could be PV modules, fuel cells, micro-turbines or full-scale inverter-interfaced wind turbines. With the fast development of power electronics devices, IBDGs are penetrating more and more into the distribution system, and, consequently, the contribution of IBDGs to the fault current must be studied. The main aim of this chapter is to investigate the behaviour of IBDGs during the grid faults and the IBDGs' current contribution to the fault. Because the inverter's response to the grid fault highly depends on its control strategy [27], two main inverter control methods are studied in this chapter. Next, the inverter's O.C. protection levels are introduced, and the inverters' contribution to the fault current in each of these levels is investigated. Then, as an example, the impact of an IBDG on fuse-recloser coordination is studied, and a strategy is proposed to mitigate this impact. Simulation results are provided to support this strategy. Finally, last section of this chapter presents its conclusion.

### 3.1 Inverter control strategies

In the following sub-sections, two main inverter control strategies are presented.

#### 3.1.1 Voltage-controlled voltage source inverters

Figure 3-1 shows a voltage-controlled voltage source inverter with its control blocks. As this figure reveals, in the voltage-controlled scheme, the active and reactive power flows of the inverter are controlled by tuning the amplitude and the

phase of the inverter's output voltage. The inverter, in this control method acts as a three-phase balanced voltage source with its equivalent single-line diagram shown in Figure 3-2 [27]. As this figure shows, this method does not directly control the inverter's output current.

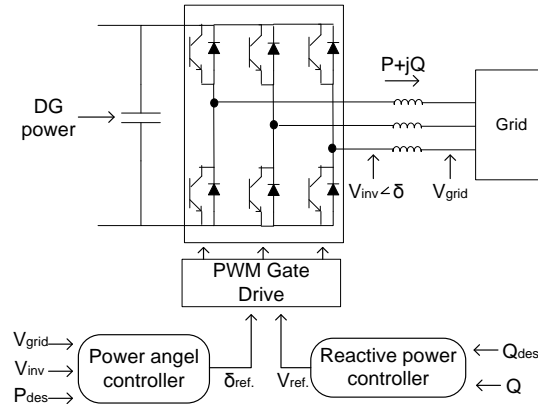


Figure 3-1: Voltage-controlled voltage source inverter with its control blocks

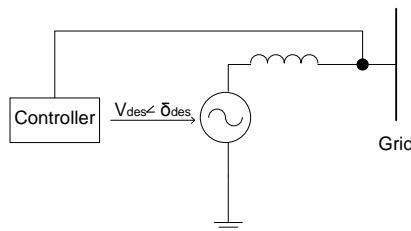
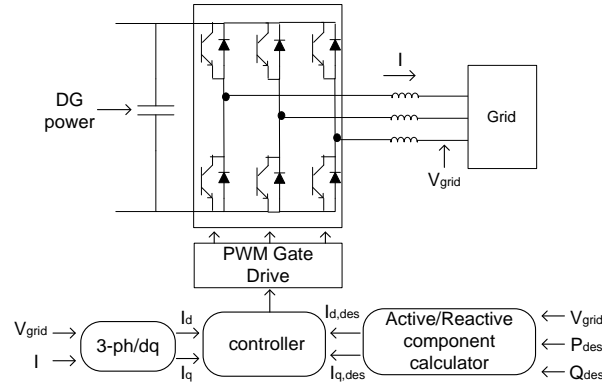


Figure 3-2: Equivalent circuit of voltage-controlled voltage source inverter [27]

### 3.1.2 Current-controlled voltage source inverters

Figure 3-3 shows a current-controlled voltage source inverter with its control blocks. As this figure shows, in the current-controlled scheme, the active and reactive power flows of the inverter are controlled by adjusting its output current [28]. The inverter, in this control method, acts as a three-phase balanced current source. Its equivalent single-line diagram is shown in Figure 3-4 [27]. This scheme has some major advantages in comparison to the voltage-controlled scheme, and the majority of inverters in a network are current-controlled voltage sources [27].



**Figure 3-3: Current-controlled voltage source inverter with its control blocks**

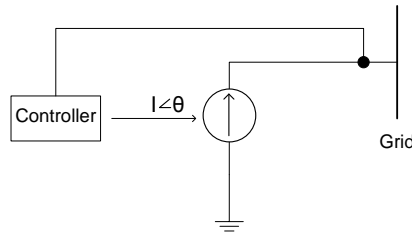


**Figure 3-4: Equivalent circuit of current-controlled voltage source inverter [27]**

## 3.2 Inverters' O.C. protection

The thermal time constants of power electronic switches are very small [28], and the restriction on the temperature of semiconductor junction in these devices makes them very sensitive to an excessive current [29]. Consequently, during the grid faults, the inverter needs a protection mechanism which ceases its switching, or restricts its current as quickly as possible, in order to protect it against severe damage. This scheme can be either DG trip or software protection.

### 3.2.1 DG trip

In this protection scheme, the instantaneous or short-time delay O.C. protection (function 50/51) disconnects the IBDG in the first few cycles or even sub-cycles. In addition, the DG is also equipped with under-voltage protection (function 27) [29]. The inverter's disconnection is obtained simply by stopping the switching signals [28]. The IBDGs in this category do not have LVRT capability and cannot be integrated into the grids with LVRT requirements.

Figure 3-5 shows the RMS output current of a voltage-controlled voltage source inverter with DG trip protection during a grid fault. In this figure,  $I_f$  depends on the impedance between the IBDG and the fault location [30]. In case of close faults, when  $I_f > 1.25$  p.u., the inverter will be ceased in less than half a cycle [27] (e.g. 5 m.sec. [29]). In case of distant faults, when  $I_f > 1.1$  p.u., the IBDG will be disconnected in less than 100 m.sec.

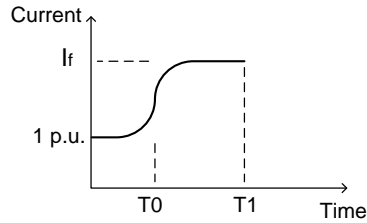


Figure 3-5: Typical inverter's RMS current during the fault (trip protection)

### 3.2.2 Current-limiting protection

In this protection scheme, instead of tripping the inverter, a current-limiting mechanism is embedded in the inverter's control loop and limits the inverter's output current to a predefined threshold during the grid's disturbances. This protection scheme protects the IBDG's semi-conductor switches from excessive currents and facilitates LVRT by avoiding DG trip. Several methods to achieve the current-limiting protection have been introduced in [31]-[32]. Regardless of the limiting method, an inverter with the current limiting protection has a fault response similar to that in either Figure 3-6(a) or Figure 3-6(b).

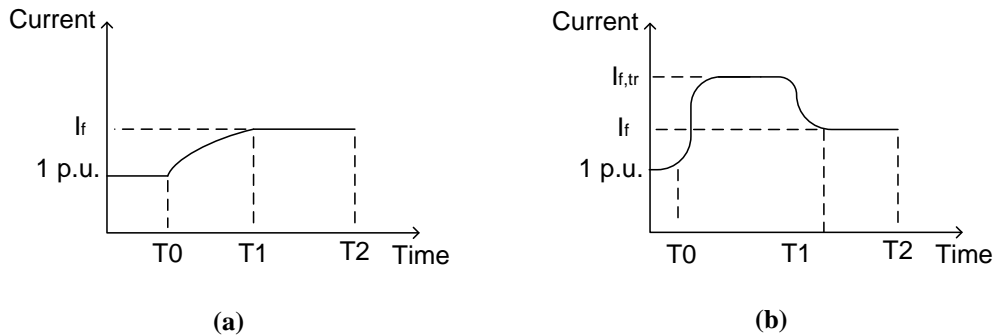


Figure 3-6: Typical inverter's RMS current during the fault (current limiting protection)

As these figures show, the inverter's response can be divided into three periods: transient ( $T0 < t < T1$ ), the steady-state ( $T1 < t < T2$ ) and trip ( $t > T2$ ). In both cases, steady-state fault current  $I_f$  could be as high as 115% of its rated current (in some cases, 150-200%). After  $T2$ , the inverter's under-voltage protection disconnects the inverter from the grid. According to IEEE1547 [4], the period between  $T0$  and  $T2$  could be up to .16 sec (9.6 cycles).

The only difference between Figure 3-6 (a) and Figure 3-6 (b) is that in the latter, the transient fault current is higher than its steady-state value ( $I_{f, tr}$  could be up to 200% of the rated current.) However, this transient fault current lasts for only about 1 cycle; i.e., in Figure 3-6(b),  $T1 - T0 < 17m.sec$ . In other words, in such inverters, output current reaches to 2 p.u. in the first cycle after the fault, and then is limited to 1.15 p.u. for some cycles and then is disconnected. Normally, the voltage-controlled voltage source inverters show such response. In contrast, for inverters with fault responses similar to that in Figure 3-6(a), when the fault occurs, a few cycles are required for the inverter to reach its current limit of 1.15 p.u., and then the current remains at this level for some cycles, and after that, the inverter is disconnected by its under-voltage protection. Normally, current-controlled voltage source converters show such responses.

### 3.3 Contribution of IBDGs to fault current

IBDGs with DG trip protection barely impact on the O.C. protection. Indeed, the contribution time window in these DGs is too short to interfere with the distribution system's protection. For example, in [13], the short circuit test result for a typical 1 kW inverter is provided. In this test, the inverter's maximum peak current was approximately 5 times the pre-fault peak current ( $I_f = 5$  p.u.). However, the inverter's operation was ceased in 0.1 cycle ( $T_1 - T_2 = 1.6 m.sec.$ ) Also, in [13] a manufactured inverter fault current is provided in which the peak fault current reaches 3 times its value during the pre-fault period but lasts for only 4.25 m.sec. The comparison of these time windows and the typical response times of the O.C. devices (Figure 2-3) reveals that these DGs cannot impact on the O.C. protection coordination.

In case of IBDGs with the current-limiting protection, although the magnitude of the current is limited, it can last for several cycles. In such DGs, the control system intentionally restricts the output current to a pre-set value.

For example, in [33], two commercial 3-phase 480V 30kW solar inverters were tested. Both inverters had fault responses similar to Figure 3-6(b). Under the 3-phase to ground fault at the inverters' terminals, the first inverter produced a current about 1.8 p.u. for the first cycle after the fault occurred, and then the current decreased to its rated value. Finally, the inverter shut down 9 cycles after the fault (See Figure 3-7). Likewise, the second inverter produced a current of around 1.2 p.u. in the first cycle after the fault occurred and then, the current decreased to almost its rated value and finally, inverter shut down after 6 cycles (See Figure 3-8).

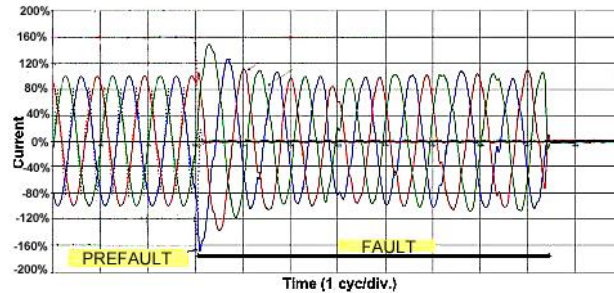


**Figure 3-7: Response of a commercial inverter with current limiting protection to 3-phase fault [33]**

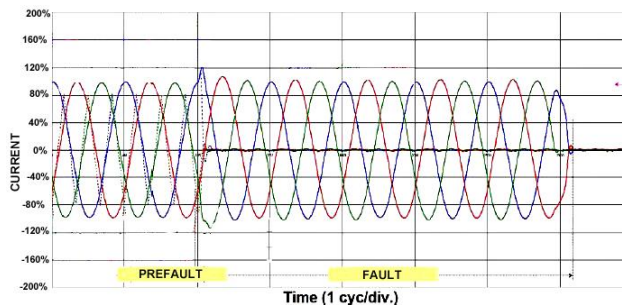


**Figure 3-8: Response of another commercial inverter with current limiting protection to 3-phase fault [[33]]**

Figure 3-9 provides another example showing the experimental result of the short circuit test for a software-protected IBDG [31]. The result shows that the

inverter's response to fault is similar to Figure 3-6 (a) and the current is restricted to the pre-defined threshold more than twice the rated current.

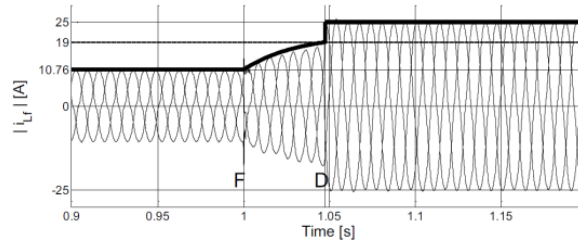


**Figure 3-9: Response of inverter with current limiting protection proposed in [31] to 3-phase fault**

### 3.4 Impact of DG on fuse-recloser coordination

As was discussed in the previous section, IBDGs with DG trip protection are ceased too soon to impact on the protection system. As a result, in this section, the focus is on IBDGs with current-limiting protection. In the following paragraphs, the impact of the IBDG on the fuse-saving scheme is investigated as an example. Finally, a mitigation strategy is proposed, and simulation results are presented.

As was briefly mentioned in section 2.2, in the fuse-saving scheme, when a fault occurs on a lateral like the one shown in Figure 3-10, the recloser R first operates one or more times based on its fast time-current curve. Most of the faults in the distribution system are temporary and are cleared during fast reclosing actions [34]. If the fault is quasi-permanent, the fuse F is supposed to clear the fault instead. The time-delayed operation of the recloser will occur if the fuse fails to interrupt the fault current. Consequently, in case of a permanent fault, the fuse is set to melt between the fast and time-delayed operation of an automatic recloser. Applying the fuse-saving scheme has two main advantages [35]:

1. No interruption in power delivery occurs due to temporary faults.
2. Fuse burning and replacement are needed only if the fault is quasi-permanent.

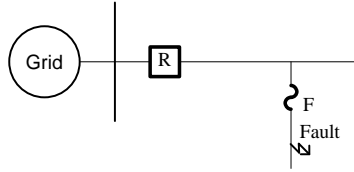


**Figure 3-10: Fuse-Recloser protection scheme in distribution feeders**

For proper coordination, the fuse and recloser curves are selected and set in a way that for all possible faults, the fuse and recloser fault currents remain within the limit shown in Figure 3-11.

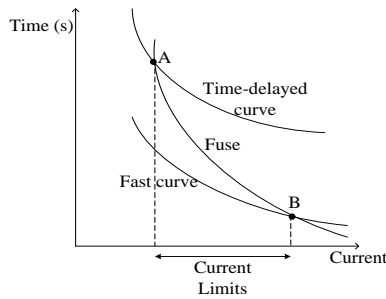


**Figure 3-11: Fuse-Recloser time-current characteristic curves**

Nonetheless, the insertion of a DG changes the fault current experienced by the fuse and recloser. For example, for low-impedance faults, adding a DG to the system may increase the fault current experienced by the fuse. This result pushes the fuse current to the right side of point B as shown in Figure 3-12. In this case, the fuse melts either simultaneously or faster than the operation of the recloser, and an undesirable permanent interruption occurs on the lateral, even for temporary faults.

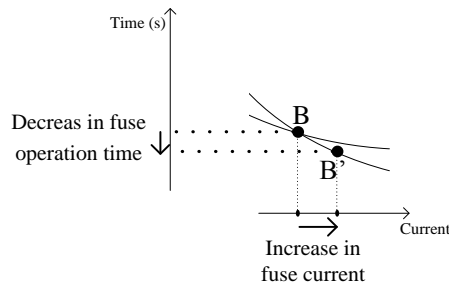


**Figure 3-12: Impact of DG on operation of protection system under low impedance fault situation**

For further analysis, Figure 3-13 shows an equivalent circuit for a system with an inverter-based DG when a fault occurs downstream of the DG. In this figure, the network upstream of the distribution substation is modeled as an equivalent ideal voltage source  $E$ , and an equivalent impedance  $Z_{net}$ . In this model, the loads are neglected (considered as open circuits) during the fault. In addition,  $Z_1$  and  $Z_2$  are feeder impedances from the substation to the PCC, and from the PCC to the fault location, respectively.  $R$  represents the recloser, and  $R_f$  is the fault resistance.

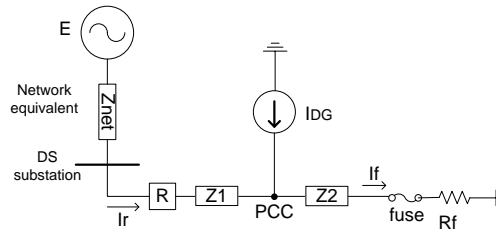


**Figure 3-13: Equivalent circuit of a distribution system with inverter-based DG, during a downstream fault.**

In this system, the three-phase short circuit per-unit current before implementing the DG can be estimated as

$$I_r = I_f = \frac{E}{Z_{net} + Z_1 + Z_2 + R_f} \quad (3-1)$$

After adding the DG, the currents through the recloser and fuse can be obtained as

$$I_r = \frac{E}{Z_{net} + Z_1 + Z_2 + R_f} - I_{DG} \frac{R_f + Z_2}{Z_{net} + Z_1 + Z_2 + R_f} \quad (3-2)$$

$$I_f = \frac{E}{Z_{net} + Z_1 + Z_2 + R_f} + I_{DG} \frac{Z_{net} + Z_1}{Z_{net} + Z_1 + Z_2 + R_f} \quad (3-3)$$

At point B of Figure 3-11, where a low-impedance fault occurs near the PCC ( $R_f + Z_2 \ll Z_{net} + Z_1$ ), the recloser and fuse currents can be approximated as

$$I_r \approx \frac{E}{Z_{net} + Z_1 + Z_2 + R_f} \quad (3-4)$$

$$I_f \approx \frac{E}{Z_{net} + Z_1 + Z_2 + R_f} + I_{DG} \quad (3-5)$$

From (3-4) and (3-5), it can be concluded that adding a DG increases the fuse current in low-impedance faults, while the fault current experienced by the recloser is almost constant. Thus, in this case, the fuse may operate faster than the recloser, leading to a coordination failure. Suppose that before adding the DG, Point B of Figure 3-11 is reached for a fault with resistance  $R_{f1}$ . After adding the DG, point B will be reached for a fault with resistance  $R_{f2}$ , where necessarily  $R_{f2} > R_{f1}$ . Consequently, fuse-recloser protection cannot be applied for faults with resistances between  $R_{f1}$  and  $R_{f2}$ .

On the other hand, for high-impedance faults ( $R_f + Z_2 \gg Z_{net} + Z_1$ ) the recloser and fuse current can be estimated as

$$I_r \approx \frac{E}{Z_{net} + Z_1 + Z_2 + R_f} - I_{DG} \quad (3-6)$$

$$I_f \approx \frac{E}{Z_{net} + Z_1 + Z_2 + R_f} \quad (3-7)$$

(3-6) and (3-7) show that for high-impedance faults (like that represented by point A of Figure 3-11), the current experienced by the recloser is reduced after adding the DG, while the fuse current is almost constant. Under this condition, the fuse operation time remains constant, but the recloser time-delayed operation occurs with an additional delay. However, this delay will not cause miscoordination since the fuse operates sooner than the recloser's time-delayed operation.

Furthermore, analysis of a fault occurring upstream to the DG was also conducted in a similar way. It was found that the situation matched closely with that of a downstream fault. This finding means the location of the faults does not play a significant role in the fuse-recloser coordination. Instead, the DG current and fault impedance will have more impact on the coordination. Moreover, compared to the situation of a high-impedance fault, where the coordination is usually maintained, a low-impedance fault tends to cause more problems. For this reason, low-impedance faults are considered in the rest of this work.

Another important factor to consider is the inverter's power factor. The provision of reactive power has been considered as one of the most important

ancillary services offered by inverter-based DGs [36]-[38]. However, if not controlled and coordinated properly, this reactive power injection may worsen the protection miscoordination. Consider a low-impedance downstream fault as an example, where the fuse current has two parts as shown in (3-5). In active power injection from the DG, the first part of the fuse current  $\frac{E}{Z_{net} + Z_1 + Z_2 + R_f}$  is about  $90^\circ$  out of phase with the PCC voltage, while the second part (the DG current)  $I_{DG}$  is forced to be in phase with the PCC voltage. As a result, the two terms have a phase shift of around  $90^\circ$ , and the relationship in (3-8) can be obtained:

$$\left| \frac{E}{Z_{net} + Z_1 + Z_2 + R_f} + I_{DG} \right| < \left| \frac{E}{Z_{net} + Z_1 + Z_2 + R_f} \right| + |I_{DG}| \quad (3-8)$$

However, in reactive power injection from a DG, both terms in the fuse current ( $\frac{E}{Z_{net} + Z_1 + Z_2 + R_f}$  and  $I_{DG}$ ) are about  $90^\circ$  out of phase with the PCC voltage. Consequently, the relationship in (3-9) is obtained:

$$\left| \frac{E}{Z_{net} + Z_1 + Z_2 + R_f} + I_{DG} \right| \approx \left| \frac{E}{Z_{net} + Z_1 + Z_2 + R_f} \right| + |I_{DG}| \quad (3-9)$$

For further illustration, Figure 3-14 shows the vector diagram of the above voltages and currents (note that the direction of the DG current is to the PCC). Figure 3-14(a) and Figure 3-14(b) show that the fault current through the fuse is larger when the DG provides reactive power. This result means that in comparison to active power injection, reactive power injection worsens the fuse-recloser coordination situation.

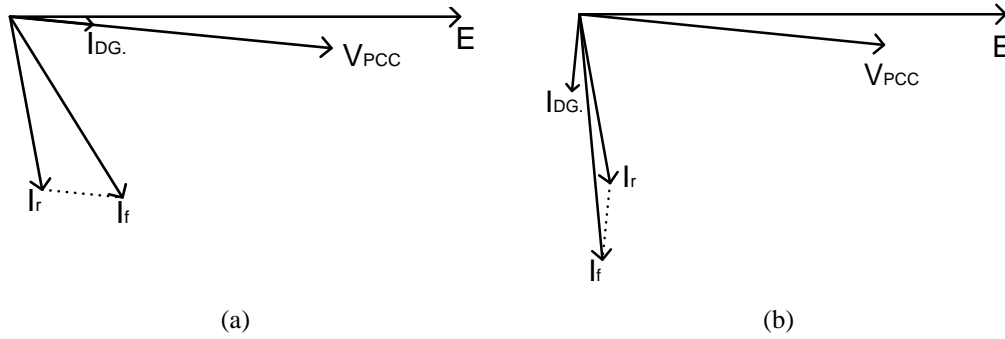


**Figure 3-14: Voltage and current vector diagram of: a) DG provides active power, b) DG provides reactive power.**

As was mentioned in Chapter 1, one aspect of LVRT capability required by grid codes is that the DGs support the grid voltage by injecting reactive power during/after the fault, while another aspect is that the DGs support the continuity of service by providing active power. The above discussion showed how these two aspects could possibly conflict with each other.

### 3.5 The proposed strategy

To mitigate the impact of the DG on the fuse-recloser coordination, a simple and effective DG current control strategy is proposed in this section.

In common practice, the inverter's current during a low-impedance fault is restricted up to twice its nominal current [39]. The ideal way to eliminate the impact of the DG on the protection system is to detect the fault and trip all the converters in that protection zone. However, this method conflicts with the LVRT capability required by some distribution grid codes. As well, converters are unable to differentiate between fault conditions and short-term disturbances such as load switching. Therefore, converter tripping in all abnormal conditions may lead to unnecessary power-delivery interruptions.

One way to ride through short-term disturbances and avoid excessive nuisance tripping is to introduce an allowed time delay, as is shown in Table 3-1. If the abnormal condition remains after the delay, according to IEEE std. 1547 [4], the converter should be tripped and then reconnected 5 minutes after the system has returned to its normal condition.

**Table 3-1: IEEE std. 1547 required response to abnormal voltage conditions [4].**

Voltage at PCC	Maximum tripping time (sec)
$V < 50\%$	.16
$50\% < V < 88\%$	2
$88\% < V < 110\%$	Normal operation
$110\% < V < 120\%$	1
$137\% < V$	.16

Currently, the fast automatic reclosers operate in less than 6 cycles after fault occurrence, so the above time delays may not be effective; i.e., during the reclosing, the DG still contributes to the arching fault. In addition, decreasing these delays may cause excessive nuisance tripping due to short-term disturbances.

One idea to simultaneously solve the miscoordination problem and ride through short-term disturbances is to reduce the converter current according to the severity of the abnormality instead of completely blocking the converter. In this case, the converters near the fault location, which will produce the greatest impact on the protection system, experience the most voltage deviation from the normal boundaries and should significantly decrease their fault current contribution. On the other hand, the more distant DG units, which have no substantial effect on the protection system, can continue their power delivery.

To implement the above-mentioned current-control strategy according to the DG terminal voltage, the DG's reference current can be determined as in (3-10)

$$\begin{cases} I_{ref.} = \frac{P_{desired}}{V_{PCC}} & \text{for } V_{PCC} \geq 0.88 p.u. \\ I_{ref.} = k V_{PCC}^n I_{max} & \text{for } V_{PCC} < 0.88 p.u. \end{cases} \quad (3-10)$$

where  $I_{ref.}$  is the converter reference current,  $I_{max}$  is the maximum output current that happens at  $V_{PCC} = 0.88 p.u.$  (the lower boundary for normal operation according to Table 3-1),  $V_{PCC}$  is the rms voltage at the DG connection node,  $P_{desired}$  is the output desired power, and  $k$  and  $n$  are constants to be determined.

Generally, the value of  $n$  determines the sensitivity of the control scheme to a voltage change. A larger value of  $n$  leads to more obvious output current reduction with a voltage sag. However, a too large  $n$  will cause the control scheme to be overly sensitive to even a small voltage disturbance. Therefore,  $n=3$  is selected in this work. Once the value of  $n$  is chosen, the coefficient  $k$  can be determined in such a way that the reference current in (3-10) remains a continuous function around  $V_{PCC} = 0.88$  p.u.; i.e.,  $k$  can be obtained from (3-11), which gives  $k=1.4674$  when  $n=3$ .

$$k(0.88)^n I_{\max} = \frac{P_{\text{desired}}}{0.88} \Rightarrow k = \frac{P_{\text{desired}}}{(0.88)^{n+1} I_{\max}} \quad (3-11)$$

Figure 3-15 shows the flow chart illustrating the reference current determination procedure.

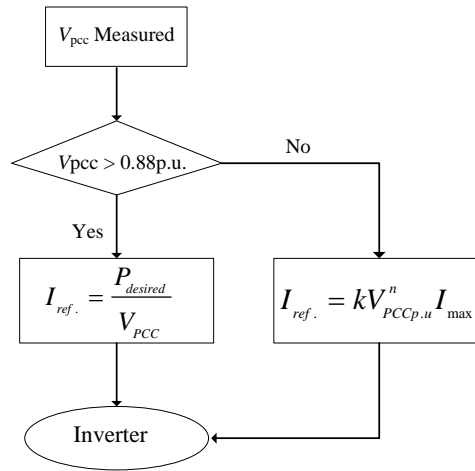


Figure 3-15: Proposed strategy to determine inverter reference current

### 3.6 Simulation results

In order to illustrate the impact of an IBDG on the coordination and to demonstrate the ability of the proposed method to mitigate this impact, several simulations were conducted. The results of these simulations are presented in following sections.

#### 3.6.1 Performance during low-impedance faults

To investigate the ability of the proposed strategy to maintain fuse-saving coordination, a 13-Node Test Feeder system (see Figure 3-16) [40] was

constructed by using MATLAB/SIMULINK. A recloser was mounted at the substation, and an inverter-based DG was connected at node 645. The simple current-controlled voltage source inverter model in [28] is used in this work. The DG's effect on the coordination between the recloser and the fuse on 645-646 was studied for faults in the middle of 645-646. Figure 3-17 shows the time-current characteristic curves of the recloser and fuse used in simulations.

In the simulated system, point B occurs for a fault resistance of 0.01 Ohm, and point A occurs for a fault resistance of 11.5 Ohms. In other words, the fuse and recloser operate properly for fault resistances between 0.01 to 11.5 Ohms. For faults with resistances lower than 0.01 Ohm, the fuse operates faster than the recloser, and the use of the fuse-saving scheme is not feasible. Note that normally, protection engineers try to select the fuse and recloser so that the operation point for a solid fault is located on the left side of point B. However, sometimes either marginal coordination cannot be avoided or the original operation point can slide to the right by network expansion. Therefore, in this study, we considered the worst condition.

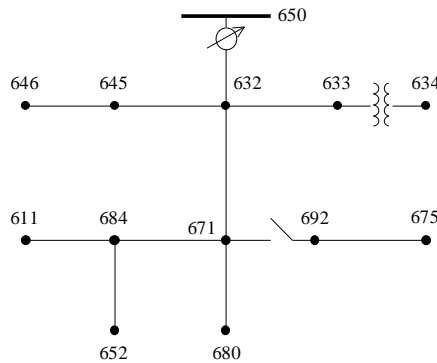


Figure 3-16: IEEE 13-Node test feeder system [40]

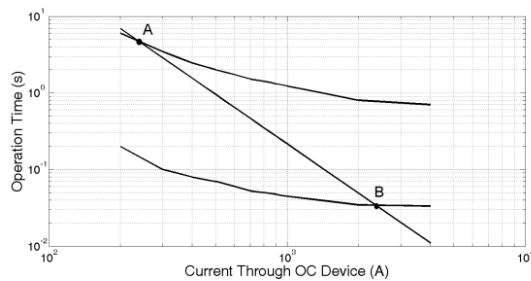
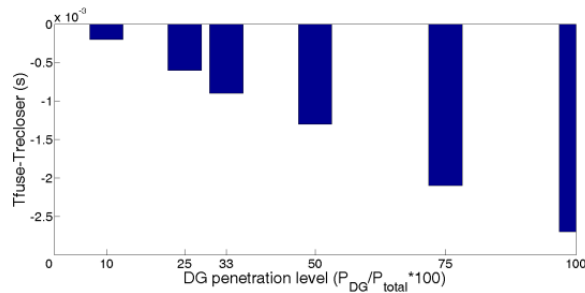


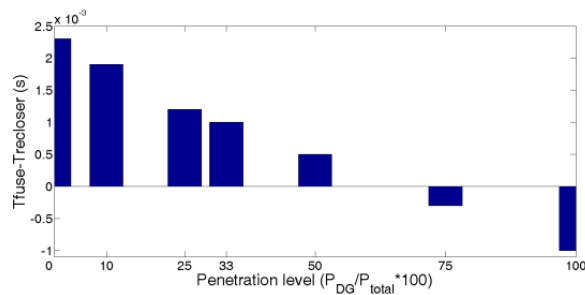
Figure 3-17: Fuse-recloser coordination in the simulated system

Figure 3-18 shows the consequence of adding a DG at different penetration levels (Penetration level= $P_{DG}/P_{load} \times 100$ ) on the O.C. coordination when a 0.01 Ohm fault occurs. As Figure 3-18 reveals, after adding a DG even at low penetration levels, the fuse operates faster than the recloser, and the protection coordination is lost.



**Figure 3-18: Difference between fuse and recloser operation time after adding DG for 0.01 Ohm fault**

This problem will appear in situations with even higher fault resistances. Figure 3-19 shows that miscoordination occurs in a fault with 0.1 Ohm resistance in the presence of a DG at high penetration levels. As this figure reveals, although the fault resistance is higher than the one in point B, adding a DG at penetration levels higher than 70% will cause miscoordination.



**Figure 3-19: Difference between fuse and recloser operation time after adding DG for 0.1 Ohm fault**

To investigate the impact of reactive power injection on the protection coordination and confirm the analysis of the previous sections, the DG control scheme was modified so that the DG provided active power during normal conditions, but injected a fully reactive current when it experienced a voltage sag ( $V_{pcc} < 0.88$  p.u.). Figure 3-20 shows the PCC's voltage magnitude and the DG

current phase angle for a fault occurring at  $t=0.25$  sec. Figure 3-21 shows the difference between fuse and recloser fast operation times under this control scheme, for a 0.01 Ohm fault.

The comparison between Figure 3-18 and Figure 3-21 reveals that the fuse melted sooner when the DG injected reactive power. This impact occurred even in situations with higher fault resistances. Figure 3-22 shows that with reactive power injection, miscoordination occurred for  $R_f=0.1$  Ohm even at low penetration levels like 30% (compared to 70% in Figure 3-18). In addition, Figure 3-23 shows that reactive power injection caused miscoordination in 0.2 Ohm faults for penetration levels higher than 75%. Note that no miscoordination occurred for 0.2 Ohm faults at any penetration level when the DG provided only active power. This example shows how reactive power generation could possibly degrade the reliability even though the original objective was to increase the service reliability.

Finally, Figure 3-24 shows the effect of the proposed control scheme on the protection coordination. As this figure shows, this control scheme successfully solved the miscoordination in low-resistance faults due to DG injection. This figure also reveals that with the proposed control scheme, the DG penetration level had almost no effect on low impedance faults because PCC voltage is very low under a low-impedance fault (see Figure 3-25), and as shown in Figure 3-26, the DG output current decreased to almost zero with the proposed method. As a result, the protection devices did not experience any difference between this system with a DG and the previous system with no DG, and the coordination was maintained (see Figure 3-27). Note that this result contrasts with the case in which traditional control was applied to the inverter. In this case, during voltage sags, the traditional control increased the inverter current until it reached the pre-set current threshold ( $I_{th}$ ), which is normally set to 1.3~2 times the  $I_{rated}$  current. Therefore, the fuse current was increased, and, consequently, miscoordination occurred.

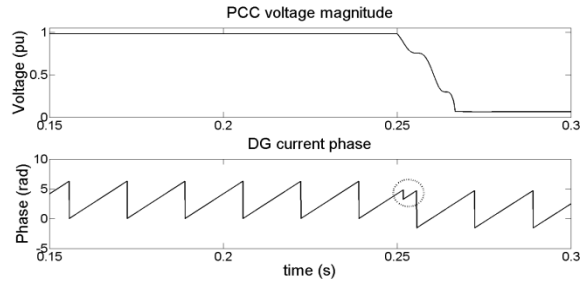


Figure 3-20: Intentional phase shift in DG current during voltage sag to support voltage.

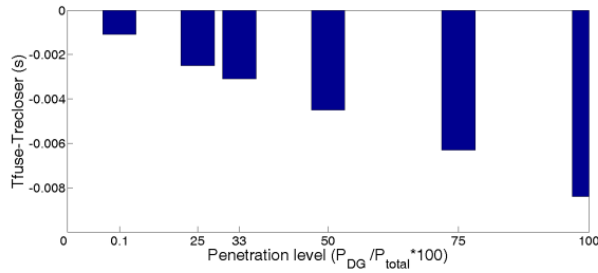


Figure 3-21: Difference between fuse and recloser operation time for 0.01 Ohm fault with  $\pi/2$  phase shift in inverter current.

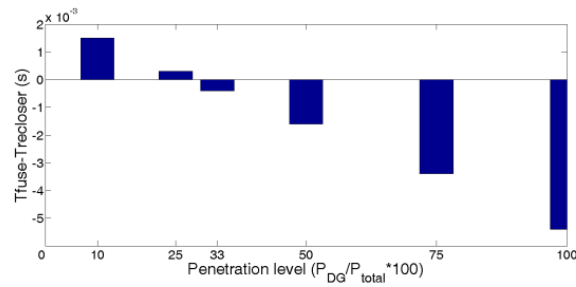


Figure 3-22: Difference between fuse and recloser operation time for 0.1 Ohm fault with  $\pi/2$  phase shift in inverter current.

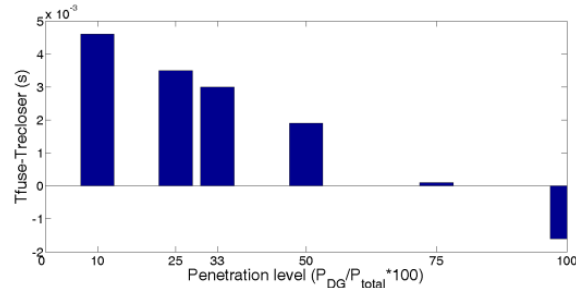
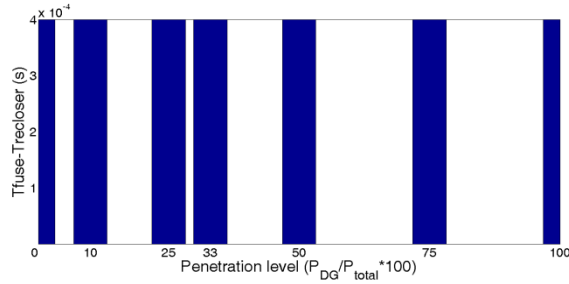
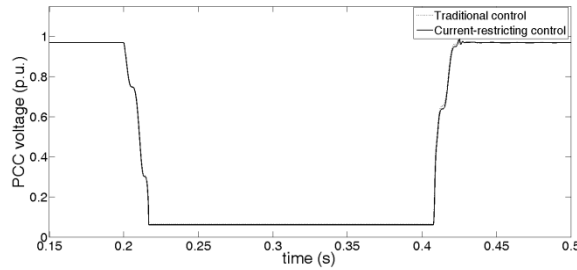


Figure 3-23: Difference between fuse and recloser operation time for 0.2 Ohm fault with  $\pi/2$  phase shift in inverter current.



**Figure 3-24: Difference between fuse and recloser operation time for 0.01 Ohm fault with inverter current reduction control.**



**Figure 3-25: PCC voltage for 0.01 Ohm fault with DG at 30% penetration level.**

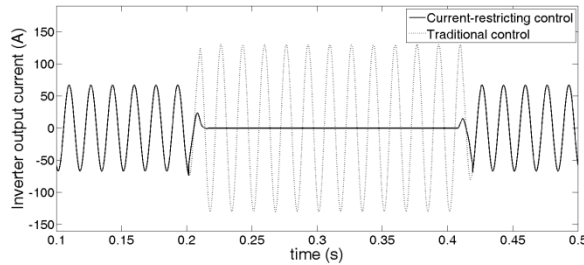


**Figure 3-26: DG output current for 0.01 Ohm fault with DG at 30% penetration level.**

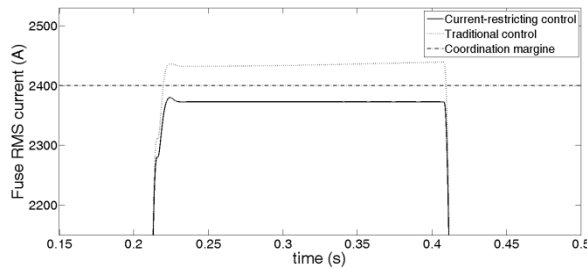


**Figure 3-27: Fuse current for 0.01 Ohm fault with DG at 30% penetration level.**

In the next step, in order to show the effectiveness of the proposed strategy in multiple DG cases, two DG units were used in the test system. One was implemented at Node 634 with a capacity equal to 20% of the total load of the

system. The other was installed at Node 675 with a capacity equal to 60% of the total load of the distribution system. Their effect on the coordination between the recloser and the fuse on 645-646 was studied for a 0.1 Ohm fault occurring in the middle of 645-646. Figure 3-28 and Figure 3-29 show these inverters' output currents when controlled by the proposed strategy. In addition, Figure 3-30 demonstrates the fuse current in both the traditional and current-restricting strategies. As this figure reveals, in contrast to the traditional control, the proposed strategy successfully kept the fuse current below the margin, and consequently maintained the coordination even when multiple DGs with high penetration at different locations were used.

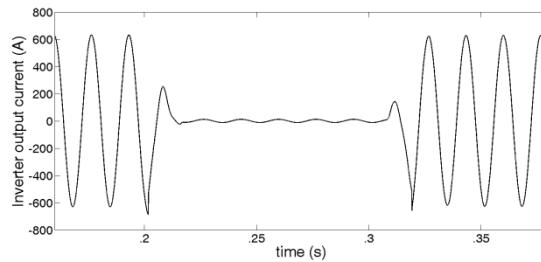


**Figure 3-28: Output current of inverter installed at Node 634.**

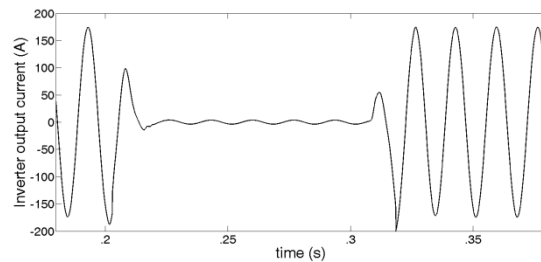


**Figure 3-29: Output current of inverter installed at Node 634.**

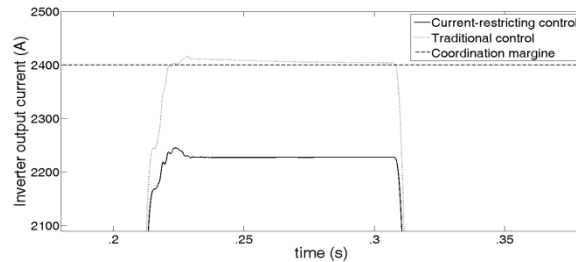


**Figure 3-30: Fuse current for 0.1 Ohm fault with DG units at Nodes 634 and 675.**

### 3.6.2 Performance during high impedance faults

The converter's operation controlled by the proposed strategy during medium- and high-impedance faults was studied in this stage of the simulations. In the first case, three DGs at a 30% total penetration level (10% each) were implemented on Nodes 633, 645 and 675, and a 2-Ohm fault was simulated in the middle of 645-646. Figure 3-31 shows the converters' output current. This figure reveals that the more distant converters experienced lower voltage sags and, consequently, provided more current during a fault.

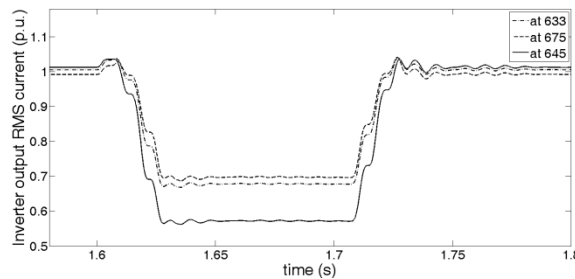


**Figure 3-31: Output current of inverters for 2-Ohm fault in the middle of 645-646.**

In the second case, a DG was installed at Node 634 with a capacity equal to the spot load at this node, and an 8-Ohm fault was simulated from 0.2 sec. to 0.3 sec. in the middle of Nodes 645-646. Figure 3-32 shows the inverter output power in this situation. Figure 3-33 shows the PCC voltage, and Figure 3-34 shows the fuse current. According to these results, the converter with the proposed control strategy can successfully ride through high impedance or distant faults without losing its power delivery capability, and improved the voltages of the local nodes without having any impact on the protection system.

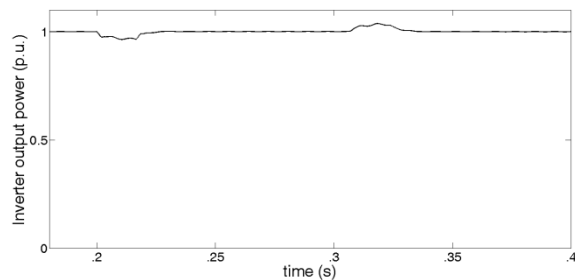


**Figure 3-32: Inverter output power for 8-Ohm fault in the middle of 645-646.**

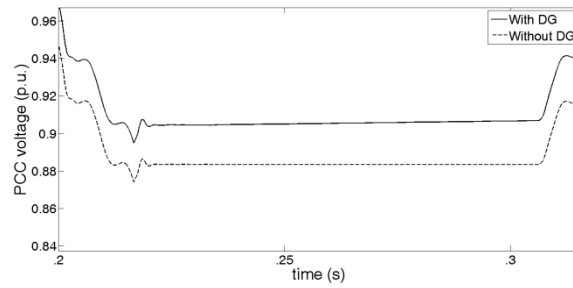


Figure 3-33: PCC voltage for 8-Ohm fault in the middle of 645-646.

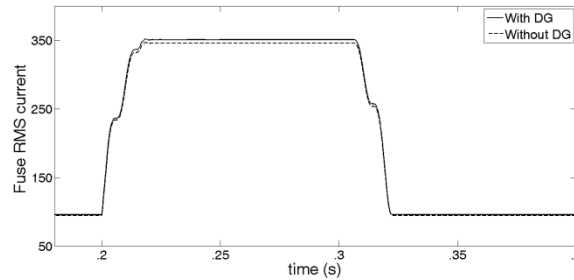


Figure 3-34: Fuse current for 8-Ohm fault in the middle of 645-646.

### 3.6.3 Performance during non-fault disturbances

To test the performance of the proposed control method under a network disturbance other than a fault condition, a distribution feeder with an induction motor load was simulated. The single line diagram of this feeder is shown in Figure 3-35. The distribution system parameters are listed in Table 3-2: Test system parameters. The substation was modeled by a three-phase balanced voltage source and equivalent impedance, and the line was modeled by series R-L branches. As shown in Figure 3-35, this feeder had five laterals, and a recloser was mounted at its middle. F is an 80A fuse, and R is a recloser in conjunction with an IEEE extremely inverse relay, which is the most suitable option for fuse-saving [41].

Figure 3-36 shows the fuse's time-current curve superimposed on the recloser's curve. Point A is the fuse operation point for a three-phase fault at the beginning of L5 before adding an inverter-based DG. Since A is to the left of B, the recloser operates faster than the fuse, and F will be saved in case of temporary faults at L5. In contrast, after adding a 1-MW inverter-based DG, the fuse's

operation point moves from A to C, and fuse saving is no longer practical unless the proposed control strategy is utilized.

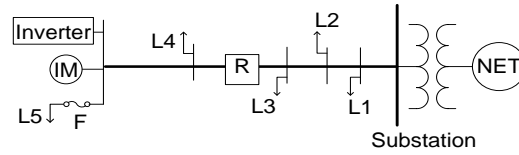


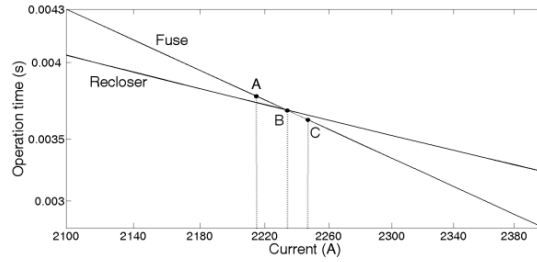
Figure 3-35: A distribution network with fuse-saving protection.

Table 3-2: Test system parameters

Parameter	Value
Main trunk overhead line length	12.00 km
Main trunk underground cable length	10.85 km
Substation short-circuit level	305 MVA
Substation equivalent impedance (including substation transformer)	$Z_{+} = 0.035 + j2.05 \Omega$ $Z_0 = 0.053 + j2.161 \Omega$
Overhead line type	336.4 ACSR
Underground cable type	500Al XLPE 25kV DBUR
Substation grounding resistance	.15 $\Omega$
Total active power load	8.79 MW

Table 3-3: Induction machine's parameters

Parameter	Value
Nominal power	1MW
Stator impedance	0.01965+ j0.0397 p.u.
Rotor impedance	0.01909+ j0.0397 p.u.
Mutual inductance	1.354 p.u.
Inertia constant	0.5 s
Friction factor	0.05479 p.u.
Pole pairs	2



**Figure 3-36: A distribution network with fuse-saving protection.**

To study the response of an inverter-based DG controlled by the proposed strategy during none-fault disturbances, the starting of a 1-MW induction motor (IM) was considered and simulated. The induction motor parameters are listed in Table 3. As demonstrated in Figure 3-37, only a 5% reduction occurs in the DG output power. Such a reduction barely decreases the voltage at the PCC. As Figure 3-38 reveals, the time-voltage curves at the motor terminal match for both the traditional and current-restricting control strategies. Finally, Figure 3-39 shows the inverter output current during this transient. As can be seen, the current limiting control is not enabled, as the inverter terminal voltage is higher than 0.88p.u.

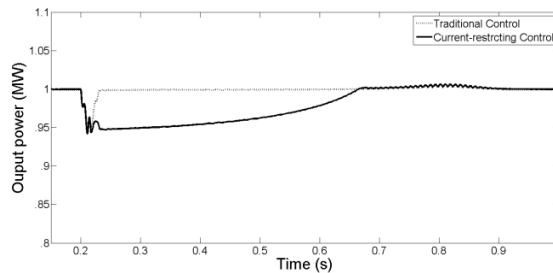


**Figure 3-37: DG output power during motor starting for both traditional and proposed control strategies.**

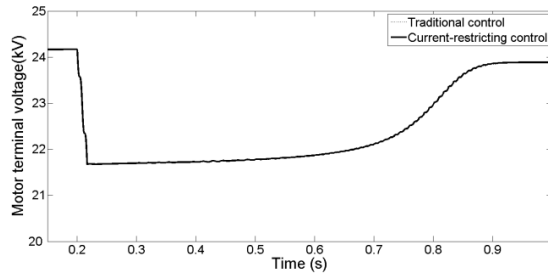


**Figure 3-38: Voltage at terminals of IM during motor starting for both traditional and proposed control strategies.**

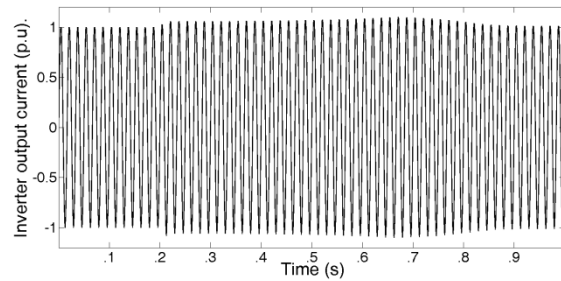


**Figure 3-39: Inverter output current during the motor starting transient.**

These simulation results not only show that the proposed control strategy is appropriate for fuse saving, but also demonstrate the robustness of this strategy against non-fault disturbances. In other words, this strategy reduces inverter output only during low-impedance faults when fuse-burning is possible. In contrast, the DG output power remains almost constant for other network disturbances, and, consequently, it does not cause further voltage reduction.

### 3.7 Conclusion

In this chapter, the contribution of IBDGs to the fault current was analyzed, and their impact on O.C. coordination was investigated. For this reason, IBDGs were categorized as either current-limiting protected or DG tripping ones. Based on this categorization, the following conclusions have been made:

1. With DG trip protection, an IBDG's fault current can reach to 5 p.u. However, the IBDG is ceased in few cycles or even less than one cycle. In this case, the contribution time window is too short to impact the coordination.
2. With current-limiting protection, an IBDG's fault current is limited to a pre-defined threshold and can be continued until the operation of undervoltage protection, which takes up to .16 sec. (9.6 cycles). The threshold can be up to 2 p.u.
3. The simulations showed that IBDGs with current-limiting protection may cause miscoordination when the protection devices are marginally coordinated.

4. To mitigate the impact of IBDGs on coordination, a strategy was proposed in which the threshold was not fixed but adjusted dynamically based on the PCC voltage. The simulation results showed that by using the proposed control strategy, the inverter's current was limited significantly when a fault happened near the PCC. As a result, the IBDG had no contribution to the fault and could not impact on the coordination. Moreover, when this strategy was used, when non-fault disturbances or distant faults occurred (on which the DG had no impact), the IBDG operated normally.

# Chapter 4

## Impact of Synchronous-Machine DGs on O.C. protection

As was mentioned in Chapter 1, DGs can be made to respond in two ways during a fault. First, the DG can be disconnected quickly after the fault, and as a result, the DG has no impact on the O.C. protection. Second, the DG can be required to ride through the low voltages. In previous chapters, it was shown that DG units with the LVRT approach can negatively impact the distribution protection system and result in serious protection malfunctions such as false tripping, relay desensitization, and miscoordination between the main and back-up protection devices [42]-[46]. In this chapter, the focus is on the contribution of SMDGs to the fault current and on mitigating their impact on the O.C. protection. To mitigate the SMDG's impact on the distribution protection system, several methods have been proposed, which can be classified into the following categories:

1. Limiting the DG capacity [47]-[49],
2. Modifying the protection system by using extra breakers or reclosers, reconfiguring the network, or using distance or directional relays [50]-[53],
3. Using adaptive protection [54]-[56], and
4. Utilizing Fault Current Limiters (FCLs) [57]-[59].

Although these methods are effective for mitigating the SMDG impact on the protection system, they have some obvious disadvantages. Limiting the DG capacity is not desirable since doing so also limits the DG penetration level. Modifying the protection system is costly. Moreover, doing so requires utility involvement and makes the protection procedure more complicated. Similarly,

adaptive protection requires new communication infrastructures as well as fast processing units. Finally, utilizing FCLs is also undesirable because of the additional cost that using them imposes on utility or DG owners.

This chapter proposes a strategy to increase the SMDG's compatibility with the distribution network by mitigating the SMDG's negative impact on the protection system. The idea is to establish a method to restrict the DG's contribution to the fault current and, consequently, prevent its impact on the O.C. protection. This idea can be implemented by either re-designing the generator and considering large transient reactances, or controlling the machine's field. In this thesis, the latter approach is followed. The machine's field can be controlled by using either Automatic Voltage Regulator (AVR) or a field discharge circuit. In this thesis, equipping the generator with a solid-state switch-based field discharge circuit is considered as the strategy to mitigate the impact of the SMDG on the O.C. protection. The solid line in Figure 4-1 shows the research direction in this chapter. The main advantage of this approach is that the use of a field discharge circuit is self-contained (because utility involvement is not required) and less expensive. As well, the machine reacts quickly to the operation of this circuit and its use is a known practice with a good chance of being accepted by utility regulators. The other options, utilizing FCLs or protection modification, as was mentioned above, require utility involvement and are more expensive and complex than field discharge. Furthermore, re-considering machine design is challenging since any redesign will affect the machine's overall performance and also is not applicable to machines which are already in use.

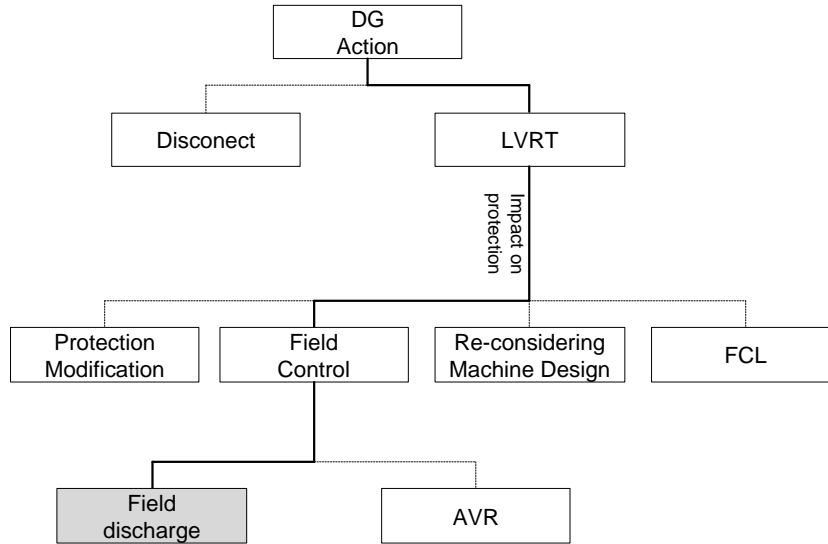
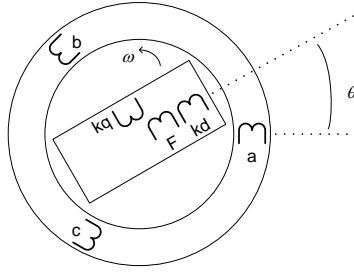


**Figure 4-1: SMDG control strategies during grid fault**

In the following sections, the operational reactances and time constants of a SG are introduced, and the typical values for these parameters are provided. Next, the response of these DGs to the grid faults is investigated. Then, case studies are provided to demonstrate the potential impact of this type of DG on the O.C. protection coordination. Next, the idea of utilizing the field discharge to mitigate this impact is discussed, and a detailed analysis and a design procedure are presented. In the next step, the case studies are re-considered by applying the field discharge to the excitation system, and the effectiveness of the method is demonstrated. Next, the impact of the field discharge on the voltage recovery in the post-fault period is studied. Finally, the impact of the field discharge circuit on the generator’s stability is investigated.

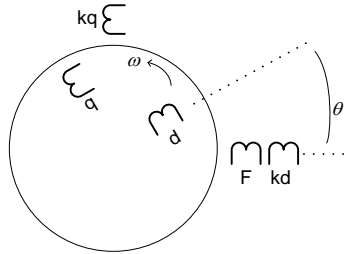
#### 4.1 Operational reactances and time constants

Figure 4-2 shows a 3-phase synchronous machine with phase windings  $a$ ,  $b$ , and  $c$  on the stator, and field winding  $F$  and damper windings  $kd$  and  $kq$  on the rotor. The mathematical relation between the voltages and currents of these windings can be expressed in terms of self and mutual inductances and resistances [60].



**Figure 4-2: Synchronous generator's structure**

The machine's air gap is not uniform, so some inductances are functions of the relative position  $\theta$ . In order to simplify the calculations, the stator parameters can be transformed to a reference frame fixed on the rotor. In this way, two fictitious windings with the same number of turns as those of the phase windings are located on the direct- and quadrature-axes shown in Figure 4-3. Then their currents are defined so that they produce the same mmf wave as that produced by the actual phase currents.



**Figure 4-3: Equivalent synchronous machine with fictitious  $d$ - and  $q$ -axis windings**

The flux linkage in the  $d$ -axis can be written in terms of the  $d$ -axis current and the machine's excitation voltage as follows [60]:

$$\psi_d = \frac{x_d(p)}{\omega_0} i_d + \frac{G(p)}{\omega_0} u_F \quad (4-1)$$

where

$$x_d(p) = \frac{(1+T_d'p)(1+T_d''p)}{(1+T_{d0}'p)(1+T_{d0}''p)} X_d \quad (4-2)$$

A similar equation can be written for the  $q$ -axis

$$\psi_q = \frac{x_q(p)}{\omega_0} i_q \quad (4-3)$$

where

$$x_q(p) = \frac{(1+T_q''p)}{(1+T_{q0}''p)} X_q \quad (4-4)$$

In the above equations,  $T_d'$ ,  $T_d''$ ,  $T_{d0}'$ ,  $T_{d0}''$ ,  $T_q'$ , and  $T_{q0}''$  are the machine's time constants, and as it will be shown in the next sub-section, the latter three constants are used to express the machine's response to the fault.

During a disturbance, the SG's response can be divided into the sub-transient, transient, and steady-state periods. The length of each period depends on the above-mentioned time constants. As well, in each of these periods, the machine's equivalent circuit can be modelled by a voltage source and an operational reactance. During sub-transient condition, the operational reactances are

$$X_d'' = \lim_{p \rightarrow \infty} x_d(p) = \frac{T_d' T_d''}{T_{d0}' T_{d0}''} X_d \quad (4-5)$$

$$X_q'' = \lim_{p \rightarrow \infty} x_q(p) = \frac{T_q''}{T_{q0}''} X_q \quad (4-6)$$

and during the transient condition, the operational reactance is as below

$$X_d' = \frac{T_d'}{T_{d0}'} X_d \quad (4-7)$$

Finally, during the steady state operation of the synchronous machine, the operational impedances are  $X_d(p=0)$  and  $X_q(p=0)$  which are  $X_d$  and  $X_q$ , respectively. Table 4-1 shows the typical values for the SG time constants and operational reactances, which play a role in the machine's response to the grid faults [61].

**Table 4-1: Comparison of impedance estimation method with data-based single-point problem [61]**

Parameter	Typical range	
	Round rotor	Salient rotor
$X_d$	1-2.5 p.u.	1-2 p.u.
$X_q$	1-2.5 p.u.	.6-1.2 p.u.
$X'_d$	.2-.35 p.u.	.2-.45 p.u.
$X''_d$	.12-.25 p.u.	.15-.25 p.u.
$X''_q$	.1-.25 p.u.	.2-.8 p.u.
$T'_d$	1-1.5 s	1.5-2 s
$T''_d$	.03-.1 s	.03-.1 s

## 4.2 Synchronous generator's fault current

In this section, the SG's response to the short circuit at its terminals is studied. Amongst all types of faults, the three-phase solid fault at the terminals results in the highest fault current and, consequently, is the worst case. Besides, its calculation is simpler than those for the other types of faults due to its symmetry. Thus, in following paragraphs, this type of short circuit will be studied. Also, the rotor's speed is considered constant so that the machine's equations can be solved analytically.

For a three-phase solid fault at the generator's terminals, the machine's  $d$ - and  $q$ -axis currents and, subsequently, the phase currents, are obtained by solving the following differential equations:

$$\begin{cases} u_d = p\psi_d + \omega\psi_q + R_a i_d = 0 \\ u_q = p\psi_q - \omega\psi_d + R_a i_q = 0 \end{cases} \quad (4-8)$$

By replacing  $\psi_d$  and  $\psi_q$  with 4(4-1) and (4-2), respectively, and calculating the initial conditions by using the steady state analysis of the pre-fault, (4-8) can be

analytically solved. Briefly, the SG's current at phase a in case of a 3-phase solid fault at the terminals can be expressed as follows:

$$\begin{aligned}
 i_a = & U_{mq} \left[ \frac{1}{X_d} + \left( \frac{1}{X_d'} - \frac{1}{X_d} \right) e^{-\frac{t}{T_d'}} + \left( \frac{1}{X_d''} - \frac{1}{X_d'} \right) e^{-\frac{t}{T_d''}} \right] \cos(\omega_0 t + \theta_0) \\
 & - \frac{U_{mq}}{2} \left( \frac{1}{X_d''} + \frac{1}{X_q''} \right) e^{-\frac{t}{T_a}} \cos(\theta_0) - \frac{U_{mq}}{2} \left( \frac{1}{X_d''} - \frac{1}{X_q''} \right) e^{-\frac{t}{T_a}} \cos(2\omega_0 t + \theta_0) \\
 & - U_{md} \left[ \frac{1}{X_q} + \left( \frac{1}{X_q''} - \frac{1}{X_q} \right) e^{-\frac{t}{T_q''}} \right] \sin(\omega_0 t + \theta_0) + \frac{U_{md}}{2} \left( \frac{1}{X_d''} + \frac{1}{X_q''} \right) e^{-\frac{t}{T_a}} \sin(\theta_0) \\
 & - \frac{U_{md}}{2} \left( \frac{1}{X_d''} - \frac{1}{X_q''} \right) e^{-\frac{t}{T_a}} \sin(2\omega_0 t + \theta_0)
 \end{aligned} \tag{4-9}$$

To obtain the currents at phases *b* and *c*,  $\theta_0$  should be replaced by  $(\theta_0 - 2\pi/3)$  and  $(\theta_0 - 4\pi/3)$ , respectively.

As (4-9) reveals, the fault current consists of three components: the decaying dc, the ac at the fundamental frequency, and the decaying ac at twice the fundamental frequency. The ac component at the fundamental frequency is the most important component in terms of the O.C. protection because most of the O.C. relays filter the other components and operate based on only the 60Hz component of the fault current. This component itself consists of three parts.

### 1. Sub-transient part

$$\begin{aligned}
 i_{sub.} = & U_{mq} \left[ \left( \frac{1}{X_d''} - \frac{1}{X_d'} \right) e^{-\frac{t}{T_d''}} \right] \cos(\omega_0 t + \theta_0) \\
 & - U_{md} \left[ \left( \frac{1}{X_q''} - \frac{1}{X_q} \right) e^{-\frac{t}{T_q''}} \right] \sin(\omega_0 t + \theta_0)
 \end{aligned} \tag{4-10}$$

This part is a decaying part of the 60Hz component with sub-transient time constants in the range of .03-.1 sec. (see Table 4-1). Therefore, this component disappears 2~3 cycles after the fault occurrence. In order to find a typical RMS value for this part, the RMS of (4-10) can be approximated as follows (by ignoring the machine's saliency):

$$i_{sub.,RMS} \approx \frac{1}{X_d'} e^{-\frac{t}{T_d'}} \quad (4-11)$$

After inserting the typical values from Table 4-1 into (4-11), it can be concluded that the maximum RMS of the generator's sub-transient 60Hz component is in the range of 4~8 p.u.

## 2. Transient part

$$i_{tran.} = U_{mq} \left[ \left( \frac{1}{X_d'} - \frac{1}{X_d} \right) e^{-\frac{t}{T_d'}} \right] \cos(\omega_0 t + \theta_0) \quad (4-12)$$

This part is also decaying with a transient time constant in the range of 1-2 sec. (see Table 4-1). Thus, this component lasts for several cycles after the fault occurrence. In order to find a typical RMS value for this part, the RMS of (4-12) can be approximated by the following equation:

$$i_{tran.,RMS} = \frac{1}{X_d'} e^{-\frac{t}{T_d'}} \quad (4-13)$$

After inserting the typical values from Table 4-1 to (4-13), it can be concluded that the maximum RMS of the generator's transient 60Hz component is in the range of 3~5 p.u.

## 3. Steady-state part

$$i_{s.s.} = U_{mq} \left[ \frac{1}{X_d} \right] \cos(\omega_0 t + \theta_0) - U_{md} \left[ \frac{1}{X_q} \right] \sin(\omega_0 t + \theta_0) \quad (4-14)$$

This part does not decay, appears after the transient period, and lasts until the fault is cleared. In order to find a typical RMS value for this part, the RMS of (4-14) can be estimated by using the following equation:

$$i_{s.s.,RMS} \approx \frac{1}{X_d} \quad (4-15)$$

After inserting the typical values from Table 4-1 into (4-15), it can be concluded that the maximum RMS of the generator's steady-state 60Hz component could be less than 1 p.u.

For further illustration, the current waveform of a typical generator in case of a 3-phase solid fault at the terminals at  $t=0.2$  sec. is demonstrated in Figure 4-4.

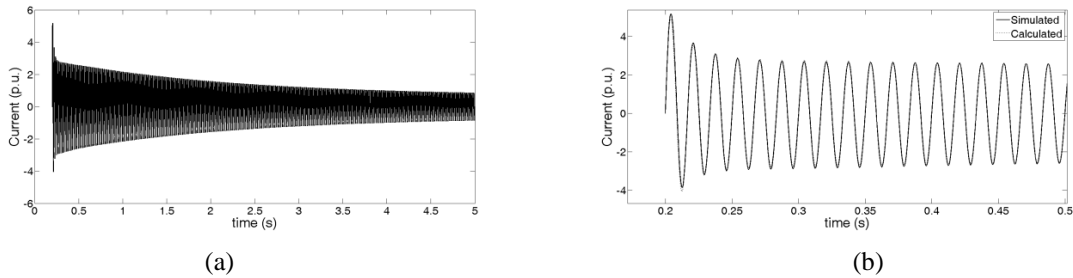


**Figure 4-4: Typical synchronous generator's fault current: (a) Complete waveform, (b) first 18 cycles**

It is useful to compare the synchronous generator's response to the grid fault with the typical characteristics of O.C. protection devices. By comparing Figure 4-4 and Figure 2-3, and considering the generator's typical time constants available in Table 4-1, it can be concluded that the generator's sub-transient response coincides with the operation of the instantaneous and extremely inverse-time relays, while the transient response of the generator (when the generator's output is 3~5 p.u.) coincides with the operation of the short-time delay and the inverse and very inverse-time O.C. relays which provide the majority of the O.C. protection.

### 4.3 Case studies

The main aim of this sub-section is to illustrate the impact of a SMDG on the O.C. protection coordination. Two case studies are provided. In the first one, the impact of a SMDG on the main and the back-up protection coordination is analyzed. In the second one, the impact of a SMDG on the fuse-saving scheme is described.

#### 4.3.1 Impact on the main and back-up protection coordination

In this section, the contribution of a SMDG to 3-phase faults in the distribution system is studied, and the SMDG's impact on the O.C. protection is analyzed. To do so, a sample 25 kV distribution system with its single line diagram shown in Figure 4-5 was simulated. In this system, the upstream network is represented by a Thevenin equivalent of a voltage source and a series

impedance  $Z_{source} = .1396 + j.4800$  p.u. ( $V_{base} = 25$  kV,  $S_{base} = 100$  MVA), and the feeder is composed of 4-wire overhead ACSR conductors. As Figure 4-5 shows, the feeder has four sections, and the positive- and zero-sequence impedance of each section are  $(.12 + j.13)$  Ohm and  $(.24 + j.39)$  Ohm, respectively. This system also has four 3-phase laterals, and the total load of each lateral is shown in Table 4-2.

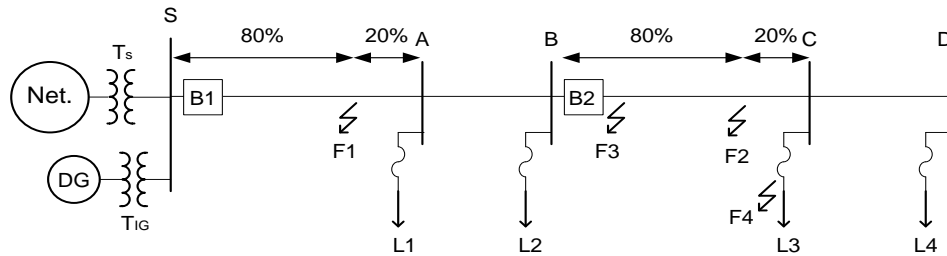


Figure 4-5: Single-line diagram of the studied case

Table 4-2: Loads and their power factors

Load	Active power (kW)	PF
L1	2511	.93
L2	530	.94
L3	4108	.93
L4	3163	.94

As Figure 4-5 shows, the feeder is protected by two breakers, B1 and B2, and the laterals L1 to L4 are protected by fuses. Each breaker is associated with two O.C. relays, one short-time delay and one inverse-time relay. The short-time delay elements are set to protect 80% of their sections, and the inverse-time relays are set to be in coordination with the next protection elements, and act as back-up. For further illustration, the pick-up current of the short-time delay element of B2 is set equal to the fault current at F2, and the pick-up current of the instantaneous relay of B1 is set equal to the fault current at F1. In addition, the Time Setting Multiplier (TSM) of the inverse-time relay of B2 is set so that B2 acts as back-up for the fuse at L3 in case of a fault at F4. Similarly, the TSM of the inverse-time relay of B1 is set to act as back-up for the short-time delay element of B2 in case of a fault at F3. Table 4-3 shows the relays' settings, and

Table 4-4 shows their operation times for different fault locations when no DG is in the system.

**Table 4-3: Relays' settings**

	Inverse-time relay		Short-time delay element	
	$I_{pick-up}$ (A)	TSM	$I_{pick-up}$ (A)	Operation time (s)
<b>B1</b>	320	.2775	4440	.1
<b>B2</b>	240	.1447	4030	.1

**Table 4-4: Fault currents and relays' operation times**

Fault	$I_{R1}$ (A)	$T_{R1}$ (s)	$I_{R2}$ (A)	$T_{R2}$ (s)
<b>F1</b>	4440	.1	-	-
<b>F2</b>	4038	.745	4030	.1
<b>F3</b>	4190	.73	4187	.1
<b>F4</b>	3996	.75	4002	.35

When the SMDG is added in the substation, the SMDG's contribution to the fault increases the fault current which flows through the protection devices. This increase may cause miscoordination between B1 and B2. As an example, consider a fault at F3. When there is no DG, the current through B2 is 4187A which leads to the operation of its instantaneous relay, while the current through B1 is 4190A, which results in the operation of its inverse-time relay. However, when the DG is added, if it increases the fault current at F3 above 4440A (the pick-up current of B1's instantaneous relay), both B1 and B2 operate simultaneously, and the whole feeder is de-energized. Figure 4-6 shows the fault current at F3 for the case with 5MW SMDG with parameters tabulated in Table 4-5. As this figure shows, for SMDGs with higher capacities, the coordination between B1 and B2 will be lost. As an example, Figure 4-7 shows how a 6.5 MW SMDG moves the protection operation points from "A" to "B" and causes miscoordination.

**Table 4-5: Operational constants of simulated synchronous machine [62]**

Time constant (s)	Operational reactance (p.u.)
$T_{d0}'=9.00000$	$X_d=1.55000$
$T_d'=2.03226$	$X_q=1.40000$
$T_{d0}''=.03000$	$X_d'=.35000$
$T_d''=.01543$	$X_d''=.18000$
$T_{q0}''=.04000$	$X_q''=.18000$
$T_q''=.01711$	

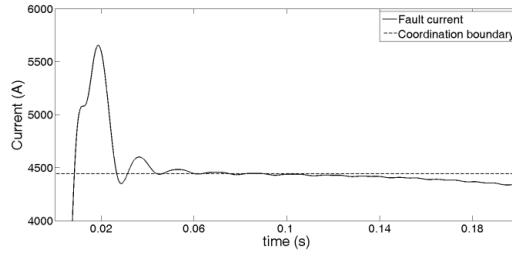


Figure 4-6: Fault current at F3 when a 5MW SMDG is added at substation

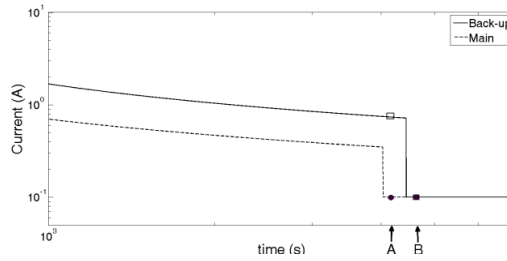


Figure 4-7: Impact of 6.5MW SMDG on relays' operation points

### 4.3.2 Impact on fuse-saving scheme

Figure 4-8 shows a 25-kV distribution system with two feeders. In this system, the upstream network is represented by a Thevenin equivalent of a voltage source and a series impedance  $Z_{source} = .26 + .883j \text{ p.u.}$  ( $V_{base} = 25 \text{ kV}$ ,  $S_{base} = 100 \text{ MVA}$ ). Feeder 1 is composed of 4-wire overhead 336.4 ACSR conductors represented by series impedance  $Z_{feeder1} = .0384 + .0416j \text{ p.u./km}$ , and Feeder 2 is composed of 4-wire overhead 4/0 ACSR conductors represented by series impedance  $Z_{feeder2} = .056 + .074j \text{ p.u./km}$ . The length of each section is shown in Table 4-6. According to Figure 4-8, feeder 1 has three laterals, and feeder 2 has only one lateral. The total load of each lateral is shown in Table 4-7.

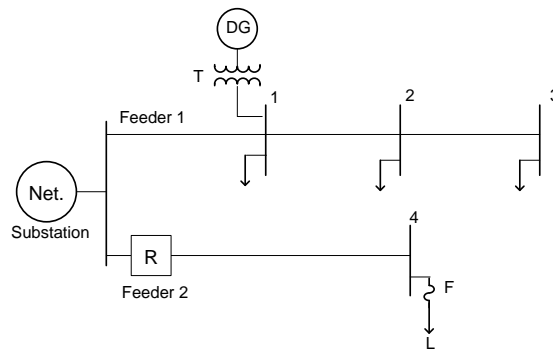


Figure 4-8: Single-line diagram of sample network

**Table 4-6: Sections' lengths**

Section	Length (km)
S1	1
12	3.2
23	5
S4	7.1

**Table 4-7: Loads and their power factors**

Bus	Active power (kW)	PF
1	1600	.97
2	530	.94
3	2400	.96
4	2000	.94

The main purpose for simulating this system is to analyze the impact of the SMDG at bus 1 on the fuse-recloser coordination on feeder 2. As Figure 4-8 shows, the lateral at the end of feeder 2 is protected by the fuse F, and the feeder itself is protected by the recloser R. The coordination between R and F is based on the fuse-saving protection scheme. In this scheme, when a fault occurs on the lateral, the recloser R first operates one or more times based on its fast time-current curve. If the fault is temporary, it will be cleared during fast reclosing actions. Otherwise, the fuse F is supposed to clear the fault. The time-delayed operation of the recloser will occur if the fuse fails to interrupt the fault current. Consequently, in case of a permanent fault, the fuse is set to melt between the fast and time-delayed operation of an automatic recloser. Figure 4-9 shows the fuse and the recloser characteristic curves. The fuse's operating time can be approximated by the following equation:

$$\log(t) = -1.9312\log(I) + 5.1169 \quad (4-16)$$

Also, the recloser's pick-up current is 80A, and its fast and time-delayed curves are based on the IEC inverse-time relay characteristics with TSMs equal to .043 and .796, respectively. When no DG is in the system, the highest current through the fuse is 1450A which is before point "A" of Figure 4-9 at which  $I_{fault}=1475A$ . Therefore, the fuse's operation time is between the recloser's fast and time-delayed operation times, and the use of the fuse-saving scheme is feasible.

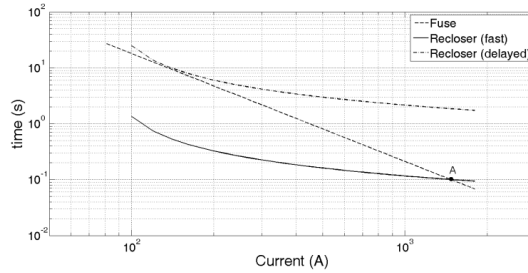


**Figure 4-9: fuse and recloser time-current characteristics curves**

A SMDG is added at bus 1 contributes to the fault and increases the current through the fuse and the recloser. If this DG is larger than 1600 kW (see Figure 4-10), the fault current will be higher than 1475A for more than .1sec. and, consequently, the fuse will melt sooner than the recloser's operation (the DG's parameters are the same as those in Table 4-5). As an example, Figure 4-11 shows the impact of a 2400kW SMDG on the fuse-recloser coordination. As this figure shows, the fault current is higher than the coordination boundary, and the fuse melts sooner than the recloser's operation.

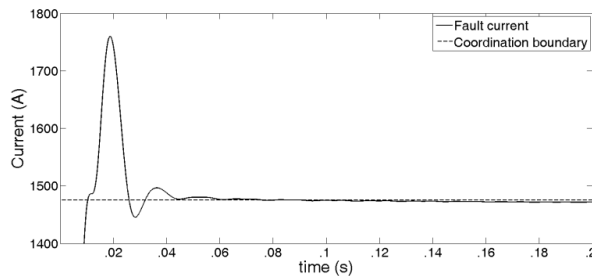


**Figure 4-10: Fuse and recloser fault current when a 1600kW SMDG is added at bus 1**

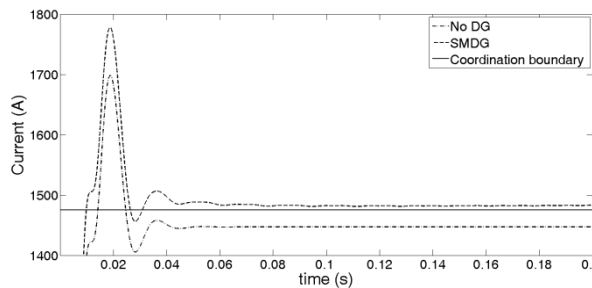


**Figure 4-11: Impact of a 2400kW SMDG on coordination**

#### 4.4 Idea of utilizing field discharge circuit

As was shown in previous sections, the SMDG has a long-lasting high output current during the fault and, consequently, has a potential impact on the O.C.

protection schemes. Basically, the main source of the synchronous generator's output current is the machine's flux linkage, which is established by the field's excitation. As a result, controlling the machine's excitation can lead to controlling the machine's output current. In the case of a fault, discharging the flux linkage could decrease the generator's output current, eliminate its contribution to the fault and, consequently, prevent O.C. protection miscoordination. Moreover, putting an external resistance in series with the field circuit when excitation voltage is being removed can accelerate the machine's discharge process. This procedure is called "field discharge." Briefly, the idea is to use the field discharge circuit to minimize the generator's output current during grid faults and, consequently, to prevent it from impacting on the existing protection system.

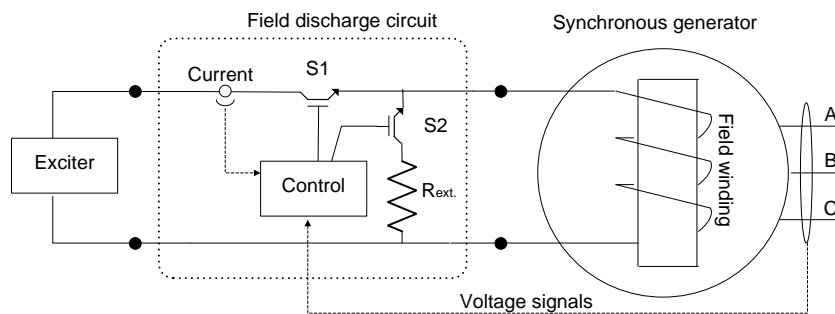
The synchronous generator's field discharge is a mature subject in power system studies. For decades, field discharge mechanisms have been designed and used for the following purposes:

1. Accelerating the generation units' shutdown: when a synchronous generator is shut down, the excitation should be disconnected from the field winding. For this reason, the field current should dissipate the field energy in a path. A field discharge resistor can provide this path and accelerate the shutdown. However, most of new excitation systems can perform normal shut down by absorbing field energy via their converters working in inverter operation mode [63].
2. Providing a path for the negative field current: during certain conditions such as pole slipping, a negative current can be induced in the field circuit. If no path is available for this current to flow through, it will induce very high voltage at the rotor circuit. The field discharge circuit provides such path for negative current [64].
3. Suppression of the shaft torsional torques: some electrical disturbances can cause large torsional stress on the turbine-generator's shaft. In [65] it is shown that the operation of field discharge circuit can effectively reduce such torsional torques.

4. Minimizing the damage due to faults inside the generator's protection zone: when a short circuit occurs prior to the generator's main circuit breaker, no protecting device is available to isolate the fault, so the main breaker will disconnect the generator from the network. However, the generator will feed the fault unless the field winding current and the energy in the machine's magnetic field are reduced to zero. Under such circumstances, a field discharge resistance is put across the field winding to accelerate the energy dissipation process and, consequently, to minimize the damage [66]-[67]. Such faults may occur at generator terminals, stator or rotor windings, or the excitation system [63].

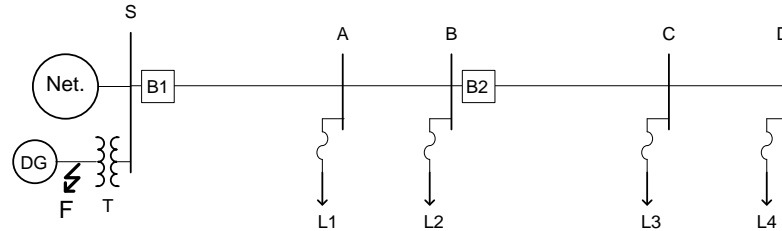
In this thesis, the field discharge circuit is designed for a new purpose: to mitigate the impact of the DG on the distribution network protection. The use of a field discharge circuit, when a fault occurs in the network, can decrease the DG unit's contribution to the fault current and, consequently, increase the maximum allowable DG penetration level by decreasing the DG's impact on the protection.

Figure 4-12 shows a synchronous generator with its solid-state switch-based field discharge circuit, in which S1 and S2 are controllable switches (IGBTs are appropriate candidates). In the proposed application, when a fault is detected, the control unit closes S2 and then opens S1, disconnecting the exciter from the field winding, and putting a discharge resistance in series with it to dissipate the energy stored in the magnetic field.



**Figure 4-12: A synchronous generator with its field discharge circuit**

In order to investigate the effectiveness of this idea, the distribution network shown in Figure 4-13 was simulated in Matlab/SIMULINK. In this system, embedding the DG at any of points S, A or B may cause miscoordination between B1 and B2. In this simulation, the SMDG was arbitrarily embedded at S. The synchronous machine's parameters were collected from [51] and tabulated in Table 4-5.



**Figure 4-13: A sample distribution network with synchronous-machine DG**

Figure 4-14 shows the RMS of the generator's output current during the fault and Figure 4-15 shows the RMS of its ac component. Note that most protection devices such as the O.C. relays filter the dc component of the fault current and operate based on the RMS of the ac component. On the other hand, some other devices such as fuses operate based on the RMS of total current. The factor  $k$  shows the ratio of the total field circuit's resistance, when the field discharge is applied, to its original resistance ( $k = (R_{ext} + R_f) / R_f$ ).

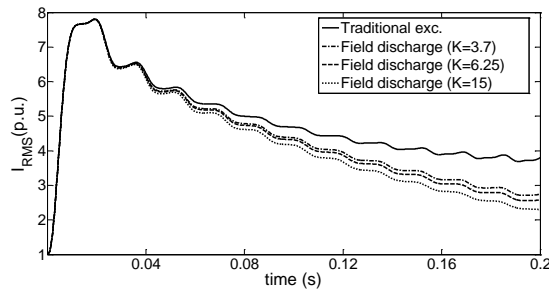


**Figure 4-14: RMS of machine's output current during 3-phase fault at point F**

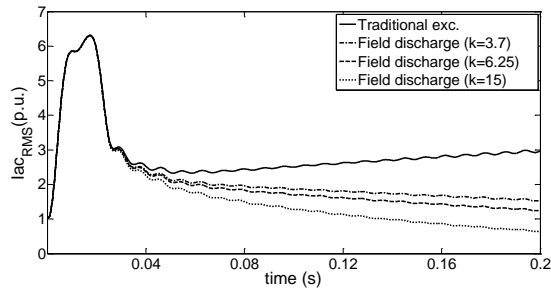


**Figure 4-15: RMS ac component of machine's output current during 3-phase fault at point F**

As Figure 4-15 reveals, except for the synchronous-machine DG with traditional excitation, the ac components of the machine's output currents are decreasing. This figure also shows that applying the field discharge can remarkably decrease the ac component of the synchronous machine's output during the fault. In the studied case, the value of this current .2 sec. after the beginning of the fault is 1.53, 1.25 and 0.64 per-unit for  $k=3.7$ , 6.25 and 15, respectively.

In addition, simulation results showed that utilizing the field discharge circuit could decrease machine's contribution to single phase faults as well as symmetrical faults. Figure 4-16 shows the RMS of the generator's output current at phase  $a$  during the phase  $a$ -to-ground fault and Figure 4-17 shows the RMS of its ac component. As these figures reveal, field discharge circuit can restrict the machine's contribution to single phase faults.

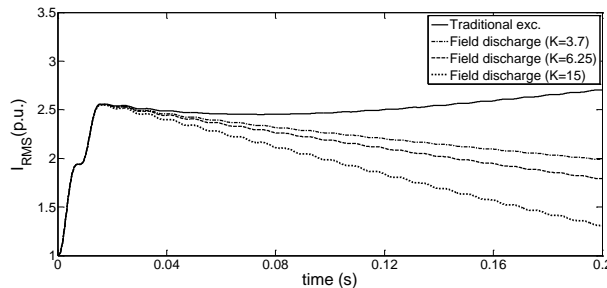


**Figure 4-16: RMS of machine's output current during 1-phase fault at point F**

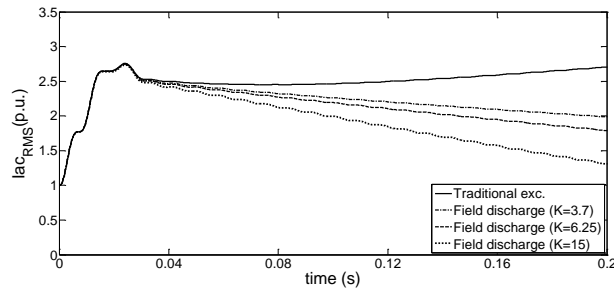


**Figure 4-17: RMS ac component of machine's output current during 1-phase fault at point F**

In addition, from these figures it can be concluded that larger resistances lead to faster decay in the ac component. However, the field discharge resistance causes overvoltage on the field winding (see Figure 4-18). This overvoltage must not be higher than the winding's maximum permissible voltage. In the next sections it will be shown that  $k=3.7$  is the largest resistance that can be used for a DG with 220V field's rated voltage, and that  $k=6.25$  is the largest resistance for a DG with 110V field's rated voltage. Therefore,  $k=15$  is not practical and is just used only to clearly demonstrate the impact of the field discharge resistance.

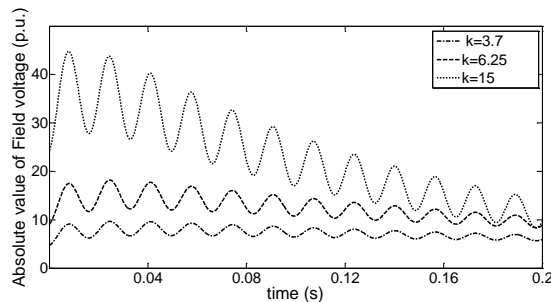


**Figure 4-18: Voltage which appears at the field winding during the fault**

## 4.5 Detailed analysis

In this sub-section, the time constants and operational reactances of a synchronous machine are reviewed, and the effect of the field discharge application on these parameters and, consequently, on the machine's fault current is analyzed.

Note: Although in practical condition, it is more realistic to consider the generator's input power constant during the fault, in the calculations and simulations in this section, the synchronous generator's speed is assumed to be

constant, so that the equations can be solved mathematically. This assumption does not have significant effect on the resultant short circuit current and the conclusion about the effect of field discharge circuit on it.

In 4.1, it was shown that the  $d$ -axis flux linkage of a synchronous machine can be written in terms of the  $d$ -axis current and the machine's excitation voltage as follows [49]:

$$\psi_d = \frac{x_d(p)}{\omega_0} i_d + \frac{G(p)}{\omega_0} u_F \quad (4-17)$$

For detailed analysis,  $x_d(p)$  and  $G(p)$  are written as follows:

$$x_d(p) = \frac{1 + (T_4 + T_5)p + T_4 T_6 p^2}{1 + (T_1 + T_2)p + T_1 T_3 p^2} \omega_0 L_d \quad (4-18)$$

$$G(p) = \frac{1 + T_{kd}p}{1 + (T_1 + T_2)p + T_1 T_3 p^2} \frac{\omega_0 L_{md}}{R_F} \quad (4-19)$$

where

$$T_1 = \frac{1}{\omega_0 R_F} (X_{md} + X_F) \quad (4-20)$$

$$T_2 = \frac{1}{\omega_0 R_{kd}} (X_{md} + X_{kd}) \quad (4-21)$$

$$T_3 = \frac{1}{\omega_0 R_{kd}} \left( X_{kd} + \frac{X_{md} X_F}{X_{md} + X_F} \right) \quad (4-22)$$

$$T_4 = \frac{1}{\omega_0 R_F} \left( X_F + \frac{X_{md} X_a}{X_{md} + X_a} \right) \quad (4-23)$$

$$T_5 = \frac{1}{\omega_0 R_{kd}} \left( X_{kd} + \frac{X_{md} X_a}{X_{md} + X_a} \right) \quad (4-24)$$

$$T_6 = \frac{1}{\omega_0 R_{kd}} \left( X_{kd} + \frac{X_{md} X_a X_F}{X_{md} X_a + X_{md} X_F + X_F X_a} \right) \quad (4-25)$$

$$T_{kd} = \frac{X_{kd}}{\omega_0 R_{kd}} \quad (4-26)$$

In order to obtain the principal time constants of the machine, the operational impedance  $X_d(p)$  should be re-written as (4-2). Then

$$(1+T'_{d0}p)(1+T''_{d0}p) \equiv 1+(T_1+T_2)p+T_1T_3p^2 \quad (4-27)$$

$$(1+T'_d p)(1+T''_d p) \equiv 1+(T_4+T_5)p+T_4T_6p^2 \quad (4-28)$$

By solving (4-27) and (4-28), the principal time constants of  $d$ -axis will be obtained. However, as normally  $R_{kd} \gg R_F$ , following approximations have been accepted in references [60]:

$$T'_d \approx T_4 \quad (4-29)$$

$$T''_d \approx T_6 \quad (4-30)$$

$$T'_{d0} \approx T_1 \quad (4-31)$$

$$T''_{d0} \approx T_3 \quad (4-32)$$

Similarly,  $X_q(p)$  is defined as follows:

$$x_q(p) = \frac{(1+T''_q p)}{(1+T''_{q0} p)} X_q \quad (4-33)$$

where

$$T''_q = \frac{1}{\omega_0 R_{kq}} \left( X_{kq} + \frac{X_{mq} X_a}{X_{mq} + X_a} \right) \quad (4-34)$$

$$T''_{q0} = \frac{1}{\omega_0 R_{kq}} (X_{mq} + X_{kq}) \quad (4-35)$$

During the sub-transient condition, the operational impedances are as follows:

$$X''_d = \lim_{p \rightarrow \infty} x_d(p) = \frac{T'_d T''_d}{T'_{d0} T''_{d0}} X_d \quad (4-36)$$

$$X''_q = \lim_{p \rightarrow \infty} x_q(p) = \frac{T''_q}{T''_{q0}} X_q \quad (4-37)$$

During the transient condition, when the damper windings have no effect, the operational impedance is as follows:

$$X'_d = \frac{T'_d}{T'_{d0}} X_d \quad (4-38)$$

Finally, during the steady state operation of a synchronous machine, the operational impedances are  $X_d (p=0)$  and  $X_q (p=0)$ , which are  $X_d$  and  $X_q$ , respectively.

Now that the operational reactances and time constants of synchronous machine have been reviewed, the effect of the field discharge on these parameters and, consequently, on the machine's fault current can be determined. In the field discharge application, when a fault is detected, the control unit closes S2 and then opens S1. Because the operation time of control unit and switches is much less than the machine's time constants, the field discharge activation is considered to be instantaneous in this thesis. In addition, the field discharge operation can be considered as combining two actions together: (a) removing excitation and (b) increasing the field circuit's resistance. In the following paragraphs, the effects of each of these actions on generator's short circuit current are studied separately, and then, the effect of the field discharge circuit operation is obtained as the superposition of these effects.

The effect of excitation removal is disappearing (4-14) (the steady-state part of the ac component, which is caused by the excitation voltage) from the generator's fault current. Figure 4-19 shows the short circuit current of a synchronous generator, and Table 4-5 lists its parameters, when the field winding was short-circuited (field discharge with zero external discharge resistance). As Figure 4-19 (a) reveals, the steady state value of current is zero. Figure 4-19 (b) shows the first 18 cycles of Figure 4-19 (a).

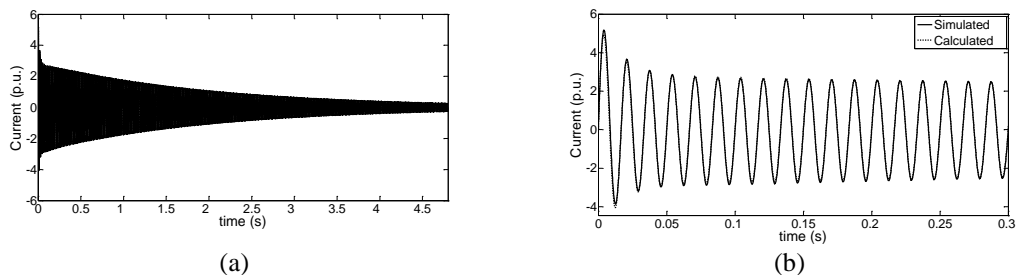


**Figure 4-19: Synchronous generator's fault current with short circuited field winding, (a) Complete waveform, (b) first 18 cycles**

To take the effect of the field discharge resistance into account,  $R_F$  should be replaced with  $R_F + R_{ext}$  in calculating  $T_l$  and  $T_d$  and, consequently, also  $T'_{d0}$  and  $T'_d$  where  $R_{ext}$  is the field discharge resistance. As a result, when the discharge resistance ( $R_{ext} = (k-1)R_F$ ) is added in series to the field winding at the fault instance, the following changes in the machine's time constants are anticipated:

$$T'_{d,new} = \frac{1}{\omega_0 k R_F} \left( X_F + \frac{X_{md} X_a}{X_{md} + X_a} \right) = \frac{T'_d}{k} \quad (4-39)$$

$$T'_{d0,new} = \frac{1}{\omega_0 k R_F} (X_{md} + X_F) = \frac{T'_{d0}}{k} \quad (4-40)$$

Moreover, if (4-39) and (4-40) are substituted into (4-36) and (4-38), the operational reactances are not expected to be changed when a discharge resistance is put in series with the field winding. As a result, the generator's output current is expected to be achieved by substituting  $T'_d$  and  $T'_{d0}$  with  $T'_d/k$  and  $T'_{d0}/k$  in (4-9), respectively. Figure 4-20 shows the generator's output current when a discharge resistance is added to the field circuit at the fault instant.

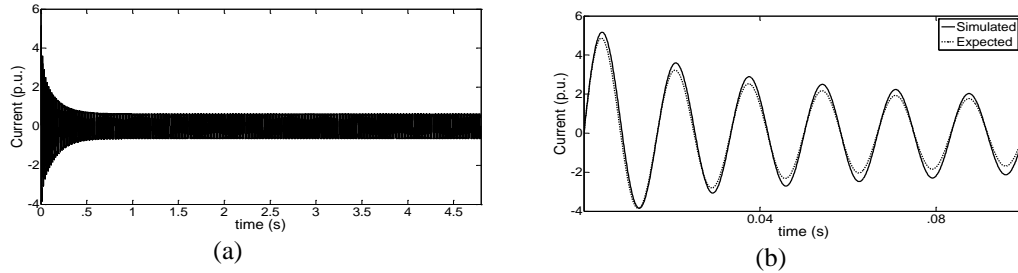


**Figure 4-20: Synchronous generator's fault current with discharge resistance in series with field winding, (a) Complete waveform, (b) first 6 cycles**

If Figure 4-20 (a) is compared with Figure 4-19 (a) it will be obvious that the transition to the steady state in Figure 4-20 is much faster than that in Figure 4-19. As well, Figure 4-20 (b) shows that (4-39) and (4-40) are not accurate enough; i.e., the anticipated time constants are smaller than the real values, and as a result, the expected current is not close enough to the generator's output current because (4-29) to (4-32) are true on the condition that  $R_{kd} \gg R_F$ . However, when a large discharge resistance is added ( $k \geq 3$ ), this assumption is no longer true. Under such

circumstances, the machine's operational parameters should be recalculated as follows:

$$T_{1,new} = \frac{1}{\omega_0 k R_F} (X_{md} + X_F) = \frac{T_1}{k} \quad (4-41)$$

$$T_{4,new} = \frac{1}{\omega_0 k R_F} \left( X_F + \frac{X_{md} X_a}{X_{md} + X_a} \right) = \frac{T_4}{k} \quad (4-42)$$

Next,  $T'_{d,new}$  and  $T'_{d0,new}$  can be obtained by accurately solving the following quadratic equations

$$(1 + T'_{d0,new} p)(1 + T''_{d0} p) \equiv 1 + (T_{1,new} + T_2) p + T_{1,new} T_3 p^2 \quad (4-43)$$

$$(1 + T'_{d,new} p)(1 + T''_d p) \equiv 1 + (T_{4,new} + T_5) p + T_{4,new} T_6 p^2 \quad (4-44)$$

and consequently, the operational reactances can be obtained as follows:

$$X'_{d,new} = \frac{T'_{d,new}}{T'_{d0,new}} X_d \quad (4-45)$$

$$X''_{d,new} = \frac{T'_{d,new} T''_d}{T'_{d0,new} T''_{d0}} X_d \quad (4-46)$$

Figure 4-21 shows how this procedure improves the estimation of the generator's fault current.

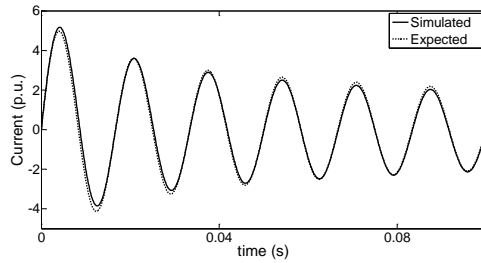


**Figure 4-21: Accurate estimation of the synchronous generator's fault current with a discharge resistance in series with its field**

The effect of the field discharge circuit operation is the superposition of the effect of these two above-mentioned actions; i.e., the generator's current has no steady-state part, and  $T'_d$ ,  $T'_{d0}$ ,  $X'_d$  and  $X''_d$  are replaced by  $T'_{d,new}$  and  $T'_{d0,new}$ ,  $X'_{d,new}$  and  $X''_{d,new}$ , which are obtained from (4-41) to (4-46). Briefly, the

generator's output current for a three-phase solid fault at its terminals when the field discharge circuit operates at the fault instance can be obtained as follows:

$$\begin{aligned}
 i_a = & U_{mq} \left[ \frac{1}{X'_{d,new}} e^{-\frac{t}{T'_{d,new}}} + \left( \frac{1}{X''_{d,new}} - \frac{1}{X'_{d,new}} \right) e^{-\frac{t}{T''_d}} \right] \cos(\omega_0 t + \theta_0) \\
 & - \frac{U_{mq}}{2} \left( \frac{1}{X''_{d,new}} + \frac{1}{X''_q} \right) e^{-\frac{t}{T_a}} \cos(\theta_0) \\
 & - \frac{U_{mq}}{2} \left( \frac{1}{X''_{d,new}} - \frac{1}{X''_q} \right) e^{-\frac{t}{T_a}} \cos(2\omega_0 t + \theta_0) \\
 & - U_{md} \left[ \left( \frac{1}{X''_q} - \frac{1}{X'_q} \right) e^{-\frac{t}{T'_q}} \right] \sin(\omega_0 t + \theta_0) \\
 & + \frac{U_{md}}{2} \left( \frac{1}{X''_{d,new}} + \frac{1}{X''_q} \right) e^{-\frac{t}{T_a}} \sin(\theta_0) \\
 & - \frac{U_{md}}{2} \left( \frac{1}{X''_{d,new}} - \frac{1}{X''_q} \right) e^{-\frac{t}{T_a}} \sin(2\omega_0 t + \theta_0)
 \end{aligned} \tag{4-47}$$

Figure 4-22 shows the effect of the field discharge circuit operation on the generator's output current during the three-phase solid fault at the generator's terminals. By comparing this figure with Figure 4-19, it can be concluded that the field discharge circuit has almost no impact on the sub-transient part of the ac component of the generator's current (first few cycles) because the damper windings and not the field winding play the dominant role during the sub-transient period. In contrast, it accelerates the decrease in the transient component. Also, by comparing this figure with Figure 4-20, it can be concluded that the field discharge circuit removes the steady-state part of the fault current.

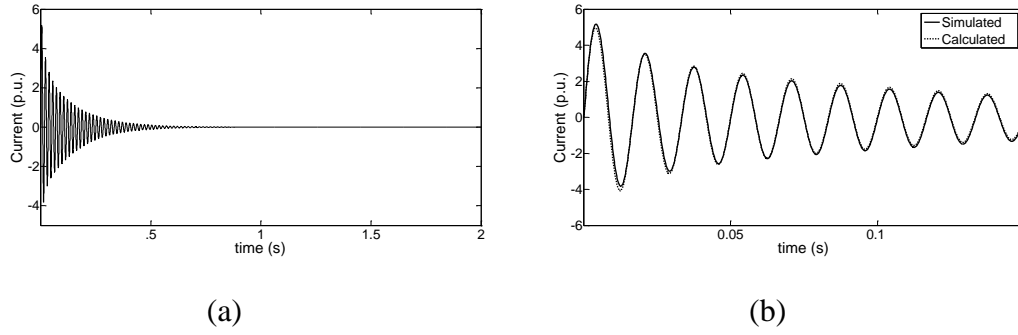


**Figure 4-22: Synchronous generator's fault current with field discharge operation, (a) Complete waveform, (b) first 9 cycles**

For O.C. relay coordination, the DC part of generator's current can be neglected because these relays operate based on the RMS of the ac component of current. Also, the second-order harmonic has a negligible amount. Therefore:

$$\begin{aligned}
 i_{a,ac} = & U_{mq} \left[ \left( \frac{1}{X'_{d,new}} \right) e^{-\frac{t}{T'_{d,new}}} + \left( \frac{1}{X''_{d,new}} - \frac{1}{X'_{d,new}} \right) e^{-\frac{t}{T_d}} \right] \cos(\omega_0 t + \theta_0) \\
 & - U_{md} \left[ \left( \frac{1}{X''_q} \right) e^{-\frac{t}{T_q}} \right] \sin(\omega_0 t + \theta_0)
 \end{aligned} \quad (4-48)$$

Note that  $\theta_0$  is a random variable and depends on the fault instance. Since O.C. relays operate based on the RMS of the ac component of the current, it is advantageous to obtain the RMS of (4-48), which is as follows:

$$I_{a,ac}(t) = \sqrt{A^2 + B^2} \quad (4-49)$$

where

$$A = U_{mq} \left[ \left( \frac{1}{X'_{d,new}} \right) e^{-\frac{t}{T'_{d,new}}} + \left( \frac{1}{X''_{d,new}} - \frac{1}{X'_{d,new}} \right) e^{-\frac{t}{T_d}} \right] \quad (4-50)$$

and

$$B = U_{md} \left[ \left( \frac{1}{X''_q} \right) e^{-\frac{t}{T_q}} \right] \quad (4-51)$$

The operation of O.C. devices normally coincides with the generator's transient response. Consequently, (4-49) can be simplified by neglecting the sub-transient

terms in (4-50) and (4-51). Such an estimation is accurate from the 4th cycle after the fault instance (t=.05 sec.).

$$I_{a,ac}(t) \approx U_{mq} \left( \frac{1}{X'_{d,new}} \right) e^{-\frac{t}{T'_{d,new}}} \quad (4-52)$$

For distant faults, assume that the equivalent impedance from the generator's terminals to fault is

$$Z_{fault} = R_{fault} + jX_{fault} \quad (4-53)$$

In this situation, the generator's contribution can be estimated by making the following modifications:

1. In the calculation of all time constants and operational reactances,  $X_a$  should be replaced by  $X_a + X_{fault}$ .
2. In the calculation of all the time constants and operational reactances,  $R_s$  should be replaced by  $R_s + R_{fault}$ .

As an example, Figure 4-24 shows the RMS ac component of the generator's current, when the fault happens 1.6 km away from the generator's terminals in the sample network shown in Figure 4-23, and the field discharge is applied ( $k=3$ ). The estimated curve is obtained from (4-52) by making the modifications mentioned above.

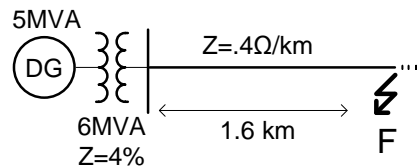


Figure 4-23: A sample distribution feeder with SMDG

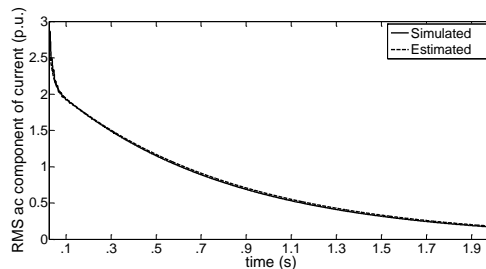
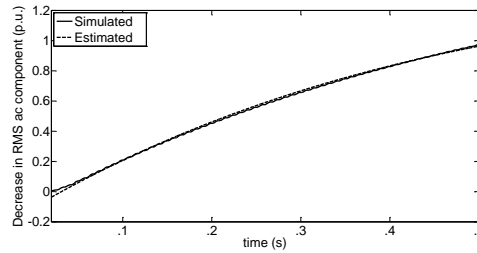


Figure 4-24: RMS ac component of generator's fault current with field discharge operation

The effect of the field discharge in reducing the generator’s RMS ac current can now be evaluated by deducting the RMS of the ac component of (4-9) from (4-52). As a result, the reduction in the RMS ac component of the current due to the field discharge can be expressed as follows:

$$\Delta I(t) = U_{mq} \left[ \frac{1}{X_d} + \left( \frac{1}{X'_d} - \frac{1}{X_d} \right) e^{-\frac{t}{T'_d}} - \left( \frac{1}{X'_{d,new}} \right) e^{-\frac{t}{T'_{d,new}}} \right] \quad (4-54)$$

Figure 4-25 shows the reduction in the RMS ac component of generator caused by the field discharge ( $k=3$ ). The solid curve was obtained from simulation and the dashed curve was obtained from (4-54). As Figure 4-25 reveals, after  $t=.05$  sec. (3 cycles after the fault instance), the estimated result matches the simulated one.



**Figure 4-25: Reduction in synchronous generator’s RMS ac component of fault current due to applying field discharge**

Now, by utilizing (4-54), the effect of the different values of the field discharge resistances in reducing the generator’s fault current can be compared. Figure 4-26 shows the reduction in the RMS ac component of the generator’s fault current for different values of  $k$ . To explain the effect of the field discharge operation on the protection devices’ coordination, this figure is divided into three areas. Typically, instantaneous O.C. devices operate in area 1, extremely inverse-time and short time-delay O.C. devices operate in area 2, and inverse and very inverse time O.C. devices operate in area 3 [21],[68]. As this figure reveals, the maximum reduction in the generator’s contribution due to the field discharge operation is 0.15 p.u in area 1. This result means that means that the field discharge is not as effective in preventing miscoordination when instantaneous devices are involved. In area 2, maximum reduction is .8 p.u. This result means

that the field discharge can be an effective mechanism for preventing miscoordination when extremely inverse-time and short time-delay O.C. devices are involved. Finally, in area 3, the maximum reduction in the generator's contribution could be up to 1.4 p.u. This result means that field discharge is a very effective mechanism when inverse and very inverse time O.C. devices are involved.

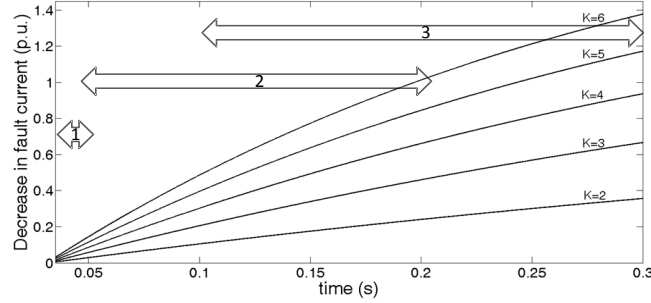


**Figure 4-26: Reduction in generator's RMS ac component of fault current for different values of field discharge resistance**

The above analysis was based on the assumption that the O.C. relays measure only the ac component of the current. However, fuses and some old electromechanical relays operate based on the total current. In such cases, the total RMS current of the synchronous generator should be considered. For phase a, this current can be obtained as follows:

$$I_a = \sqrt{I_{a,ac}(t)^2 + I_{a,dc}(t)^2} \quad (4-55)$$

where

$$I_{a,dc}(t) = -\frac{U_{mq}}{2} \left( \frac{1}{X_d''} + \frac{1}{X_q''} \right) e^{-\frac{t}{T_d}} \cos(\theta_0) + \frac{U_{md}}{2} \left( \frac{1}{X_d''} + \frac{1}{X_q''} \right) e^{-\frac{t}{T_d}} \sin(\theta_0) \quad (4-56)$$

and

$$i_{a,ac}(t) = U_{mq} \left[ \frac{1}{X_d} + \left( \frac{1}{X_d'} - \frac{1}{X_d} \right) e^{-\frac{t}{T_d}} + \left( \frac{1}{X_d''} - \frac{1}{X_d'} \right) e^{-\frac{t}{T_d'}} \right] \cos(\omega_0 t + \theta_0) - U_{md} \left[ \frac{1}{X_q} + \left( \frac{1}{X_q''} - \frac{1}{X_q} \right) e^{-\frac{t}{T_q}} \right] \sin(\omega_0 t + \theta_0) \quad (4-57)$$

According to (4-56), the dc component decays with armature's time constant, and is not a function of field circuit parameters. Therefore, the field discharge has no impact on the dc component ( $I_{a,dc}$ ). However, the field discharge can minimize  $I_a$  by reducing the ac component of the DG's current ( $I_{a,ac}$ ). Figure 4-27 shows the impact of the field discharge application on the DG's fault current components. As Figure 4-27 (a) reveals, when the traditional excitation system is applied, during the transient period the dc component decreases, while the ac component increases due to the excitation's response to the voltage drop. This response results in an almost constant total RMS current around 3 p.u. In contrast, as Figure 4-27 (b) reveals, when the field discharge is applied, both the ac and dc components are decaying. This response results in a decaying total RMS current, which decreases to around 1.4 p.u. in .2 sec. Therefore, when the field discharge is applied, the generator makes a smaller contribution to the total fault current, and a higher DG capacity can be embedded without causing any miscoordination, in contrast to the cases in which the DG utilizes the traditional excitation control during the fault.

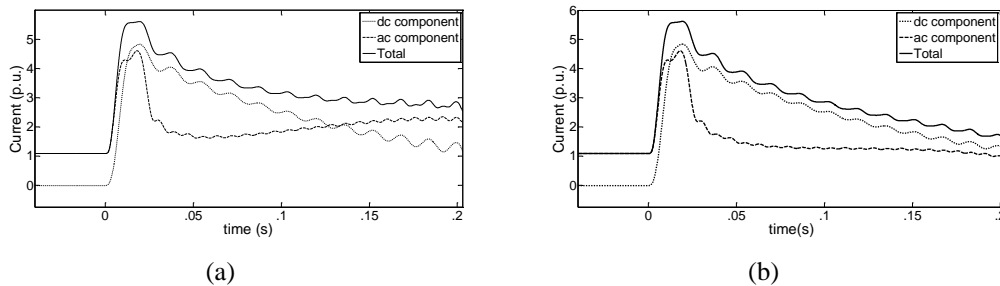


**Figure 4-27: Fault current components of synchronous generator, (a) When traditional excitation is applied, (b) when field discharge is applied**

## 4.6 Field discharge circuit design procedure

As Figure 4-12 reveals, the field discharge circuit is composed of 4 components: discharge resistance, two solid-state switches and a control unit which detects the fault and triggers the circuit. In this section, the maximum allowable field discharge resistance is obtained, and the voltage and current ratings of the switches are determined. Next, a grid fault indicator signal is

introduced which is monitored by control unit to detect the fault and trigger the circuit. For the sake of simplification and due to the very fast operation of solid-state switches, the total field discharge circuit activation process is considered in the design procedure to be instantaneous. Finally, some correction factors are applied to insure the reliability of the designed circuit.

#### 4.6.1 Field discharge resistance

The first step in the design procedure is to determine the discharge resistance. Previously in this chapter, it was shown that a larger discharge resistance leads to a smaller d-axis transient and sub-transient time constants and that, consequently, to a faster decay in generator's output current. In other words, a larger resistance can decrease the machine's contribution to the fault current more quickly than a smaller resistance. However, the discharge resistance causes transient overvoltage across the field winding which is a restricting factor in the selection of the resistance. In the following paragraphs, the field winding's transient current and voltage during the operation of field discharge circuit are obtained, and the maximum allowable field discharge resistance is determined.

The maximum current flows through the field winding when a three-phase solid fault occurs at the machine's terminals. In such condition, when no discharge circuit is applied to the rotor, the field's excessive current due to the fault can be obtained from the following equation [60]:

$$i_f = \frac{L_{md} p(1+T_{kd} p)}{R_f(1+T_{d0}' p)(1+T_{d0}'' p)} i_d \quad (4-58)$$

where  $i_d$  is as (4-59). As a result,  $i_f(t)$  can be expressed as (4-60) [60].

$$i_d(t) = U_{md} \left[ \frac{1}{X_d} + \left( \frac{1}{X_d'} - \frac{1}{X_d} \right) e^{-\frac{t}{T_d'}} + \left( \frac{1}{X_d''} - \frac{1}{X_d'} \right) e^{-\frac{t}{T_d''}} - \frac{1}{X_d''} e^{-\frac{t}{T_a}} \cos(\omega_0 t) \right] \quad (4-59)$$

$$+ U_{mq} \frac{1}{X_q''} e^{-\frac{t}{T_a}} \sin(\omega_0 t)$$

and

$$i_f(t) = i_f(0) + i_f(0) \left[ e^{-\frac{t}{T_d}} - \left( \frac{X_d - X'_d}{X'_d} \right) \left( 1 - \frac{T_{kd}}{T_d} \right) e^{-\frac{t}{T'_d}} - \left( \frac{X_d - X'_d}{X'_d} \right) \frac{T_{kd}}{T_d} e^{-\frac{t}{T_a}} \cos(\omega_0 t) \right] \quad (4-60)$$

Now, for the case with field discharge operation, (4-60) is modified by replacing  $X'_d$  and  $T'_d$  with  $X'_{d,new}$  and  $T'_{d,new}$  (calculations described in 4.5) and decaying the steady-state part of  $i_f$  to zero. Then  $i_f(t)$  after the field discharge activation can be expressed as follows:

$$i_{f,dis.}(t) = i_f(0) \left[ 2e^{-\frac{t}{T'_{d,new}}} - \left( \frac{X_d - X'_{d,new}}{X'_{d,new}} \right) \left( 1 - \frac{T_{kd}}{T_d} \right) e^{-\frac{t}{T'_d}} - \left( \frac{X_d - X'_{d,new}}{X'_{d,new}} \right) \frac{T_{kd}}{T_d} e^{-\frac{t}{T_a}} \cos(\omega_0 t) \right] \quad (4-61)$$

Figure 4-28 shows the real and approximation of a generator's field current for  $k=4$ .

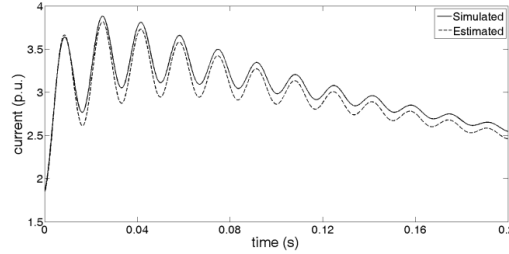


**Figure 4-28: Synchronous generator's field current during the three-phase fault at its terminals, with field discharge circuit operation**

Since  $R_{ext.} = (k-1)R_F$ , Figure 4-29 shows the rotor circuit during the discharge operation. According to this figure, the field winding's voltage in discharge period can be obtained from (4-62), and its maximum value can be obtained from (4-63):

$$v_f(t) = R_{ext.} i_{f,dis.}(t) = (k-1)R_f i_{f,dis.}(t) \quad (4-62)$$

$$V_{f,max} = (k-1)R_f i_{f,Max} \quad (4-63)$$

where  $i_{f,Max}$  is the maximum field current, which occurs either at  $t=.025$  or  $t=.0417$  sec. (the second or third peak of oscillation depending on the  $k$ ). Therefore, to find  $i_{f,Max}$ ,  $t$  is first replaced by  $.025$  in (4-61), and then replaced by  $.0417$ , and from the two obtained currents, the maximum value is selected as  $i_{f,Max}$ .

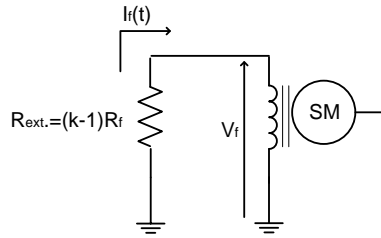


**Figure 4-29: Rotor's circuit during field discharge circuit operation**

Now,  $k$  should be restricted so that  $V_{f,max}$  remains lower than the winding's permissible insulation stress [59]. In other words,  $k$  should satisfy the following inequality:

$$k < \frac{V_{per.}}{CR_f i_{f,Max}} + 1 \quad (4-64)$$

where  $V_{per.}$  is the winding's permissible insulation stress (equal to the standard machine's field dielectric test), and  $C=1.1$  is a safety factor.

Note that  $i_{f,Max}$  itself depends on  $k$ . Consequently, in order to determine the maximum allowable discharge resistance, the field's maximum transient voltage is plotted for different values of  $k$  by using (4-63). The standard manufacturing machine field dielectric test voltage divided by  $C$  on this plot shows the maximum allowable  $k$ .

#### 4.6.2 Current and voltage ratings of solid state switches

Now that the field's transient current during the fault has been obtained, the current rating of the switches can be determined. Switch S1 is in series with exciter. As a result, the maximum current which can flow through this switch is equal to the exciter's ceiling current. Switch S2 is in series with the field during the discharge operation. Consequently, the maximum current which flows through this switch is equal to the maximum field current which is  $i_{f,Max}$ .

When S1 is off, the voltage across it is equal to the field winding's voltage. As a result, rated voltage of S1 should be equal or greater than the standard manufacturing machine's field dielectric test available in [59]. When switch S2 is off, it is in parallel with the exciter. Consequently, the maximum voltage that can

appear across this switch is equal to the exciter's ceiling voltage. Table 4-8 summarizes the switches' ratings.

**Table 4-8: Field discharge switches' ratings**

	$V_{rated}$	$I_{rated}$
<b>S1</b>	standard machine field dielectric test	Exciter's ceiling current
<b>S2</b>	Exciter's ceiling voltage	$i_{f,Max}$

### 4.6.3 Grid fault detection

In the above sections, it was supposed that some mechanism accurately and quickly detects the fault occurrence in the network and triggers the field discharge circuit. In following, this mechanism will be described.

The first and the most important step for the trigger mechanism is fault detection. To detect a fault, one of the generator's local voltage or current signals should be selected and monitored. To be an appropriate grid fault indicator, this signal should have the following properties:

1. Its variation due to the grid faults should be so fast that the fault occurrence is detected as quickly as possible,
2. This signal should have distinctive levels for different grid disturbances so that close grid faults can be distinguished from other disturbances.

Given these necessary properties, the derivative of the field's current is an appropriate indicative signal. For a 3-phase solid fault at the terminals, this signal can be mathematically obtained from (4-61).

Figure 4-30 shows the derivative of the field's current for a typical generator, whose parameters tabulated in Table 4-5, for three different disturbances: 3-phase fault in the generator's neighbourhood, 1-phase fault at one of generator's terminals, and a large sudden load change at generator's node. As this figure reveals, these signals have three distinct levels in the first cycle after the disturbances. As a result, by appropriately defining thresholds, the type of disturbance can be easily and accurately determined. In addition, it can be seen that for 3-phase faults in which the DG unit has the most contribution and also the

most probable impact on the coordination, the indicative signal has an almost instantaneous jump, which helps to detect the fault in a few milliseconds.

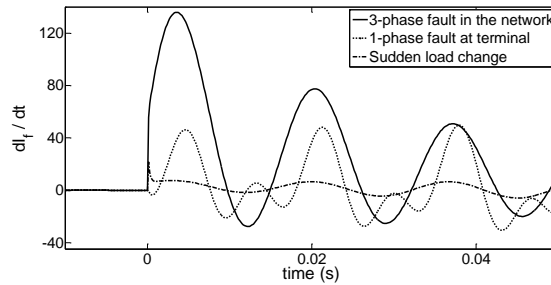


**Figure 4-30: Field's current derivative for three different grid disturbances**

When this method is implemented, the generator's O.C. protection is set so that it protects the generator from damages due to overcurrent/overload. In other words, when the field discharge circuit is implemented, the DG's overcurrent relay is set similarly to relays of the generators connected to the transmission system, and there is no conflict between generator's O.C. protection and the field discharge application. The IEEE Std. C.37.102-2006 can be followed in this case [25].

The last step is detecting the fault clearance and disabling the field discharge circuit, which can be detected by monitoring the generator's terminal voltages.

## **4.7 Mitigation of SMDG's impact on coordination: case studies**

This section presents three case studies. The first case illustrates the field discharge circuit design procedure, the second one focuses on the impact of the field discharge circuit in mitigating the main and back-up relays miscoordination, and the last one shows the ability of field discharge circuit to re-gain the fuse-recloser coordination.

### **4.7.1 Case I: Field discharge circuit design**

In this sub-section, a field discharge circuit is designed for the generator whose parameters are tabulated in Table 4-5. The first step is to determine the field discharge resistance. As it was mentioned in the previous section, in order to determine the maximum allowable discharge resistance, the field's maximum transient voltage with respect to  $k$  is plotted by using (4-63). The cross of the

standard manufacturing machine field dielectric test voltage with this plot shows the maximum allowable  $k$ .

According to [69], the standard field's dielectric test for both 110V and 220V windings, which are options for use in DGs, is 2500V. Figure 4-31 shows the generator's field winding's maximum transient voltage for different values of  $k$ . For  $C=1.1$ , the maximum allowable voltage for 110V and 220V windings is 2200V (20 and 10 p.u., respectively). These voltages occur at  $k=6.25$  and  $k=3.7$ , respectively. If the field winding's rated voltage is 220V, then maximum  $k$  is 3.7, and as a result,  $R_{ext.}=(3.7-1) R_f=2.7R_f$ .

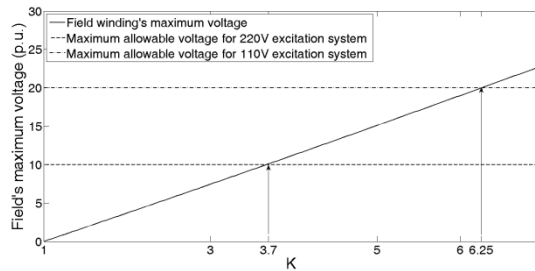


**Figure 4-31: Field winding's maximum voltage due to discharge circuit operation**

The second step is to determine the solid-state switches ratings. To do so,  $i_{f,Max}$  should be determined, which is equal to the current rating of S2. From (4-61),  $i_{f,Max} = 1.56 i_f(0)$ , where  $i_f(0)$  is the excitation current during the generator's full-load steady-state operation. For a typical generator smaller than 30MW,  $i_f(0)$  could be in the range of 15A. Then,  $i_{f,Max} = 1.56 * 15 = 23.4A$ .

In addition to  $i_{f,Max}$ , the exciter's ceiling voltage and current should be obtained from the exciter's data sheet. For a typical SIEMENS SIPOL [70], ceiling current is 20A, which is equal to the rated current of S1, and the ceiling voltage is 1.6 times the rated voltage; i.e.,  $1.6 * 220 = 352V$ , which is equal to the rated voltage of S2. All the switches' ratings are summarized in Table 4-9.

**Table 4-9: Switches' ratings in the studied case**

	$V_{rated}$	$I_{rated}$
<b>S1</b>	2500 V	20 A
<b>S2</b>	352 V	23.4 A

The last step is to design the trigger mechanism. As was mentioned in 5.3, the derivative of field current is an appropriate grid fault indicator. Suppose that the field discharge circuit is desired to operate only if 3-phase faults occur at the distribution system. In this case, the threshold is set to 60p.u./sec. As Figure 4-32 shows, single-phase faults and sudden load changes cannot cause the signal to reach this level. In contrast, the 3-phase faults exceed this level in a few ms. Therefore, the control circuit monitors the indicator signal and triggers the discharge circuit when the signal exceeds the threshold of 60p.u./sec.

#### **4.7.2 Case II: main and back-up relays coordination**

Consider the sample system studied in sub-section 4.3.1 again. It was shown that when a SMDG unit (with its parameters tabulated in Table 4-5) is added in the substation, its contribution to fault increases the fault current which flows through protection devices, and such increase causes miscoordination between B1 and B2 for DGs with higher capacities than 5MW (see Figure 4-6 and Figure 4-7).

Nevertheless, field discharge circuit operation can maintain coordination between B1 and B2 for DG units larger than 5MW. Imagine that the field's rated voltage is 220V. According to previous sub-section, maximum allowable  $k$  is 3.7. Now, consider that a 6.5 MW DG is connected to the substation through a transformer with MVA equal to 130% of DG's, and 6% series impedance. In this system, Figure 4-32 shows the fault current at F3. As this figure demonstrates, when a field discharge resistance ( $k=3.7$ ) is applied to the DG during the fault, it reduces DG's contribution, so that the fault current is decreased below 4440A in less than .1s which blocks the operation of instantaneous relay at B1 and, consequently, maintains the coordination. Table 4-10 shows the protection devices' operation times for fault at F3, and 6.5MW DG with/without field discharge operation at substation.

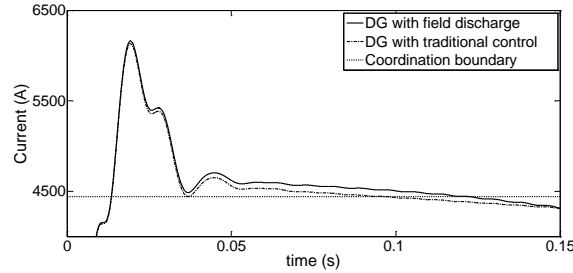


**Figure 4-32: Effect of field discharge circuit on eliminating the impact of a 6.5MW SMDG**

**Table 4-10: The relays' currents and operation times for fault at F3 and 6.5MW DG**

	$I_{R1}$	$T_{R1}$	$I_{R2}$	$T_{R2}$
<b>Without field discharge</b>	4504	.1	4483	.1
<b>With field discharge</b>	4430	.72	4413	.1

As it was shown in this case study, field discharge is able to increase maximum allowable capacity of DG from 5MW, which is equal to 48.5% of total load in distribution system, to 6.5MW which is equal to 63% of total load. However, field discharge is not able to mitigate miscoordination for capacities higher than 63%. Moreover, as Figure 4-32 demonstrates, if the operation time of the instantaneous elements were .04sec. or less, field discharge would have no effect in such short period, and no increase would occur in the DG's maximum capacity.

### 4.7.3 Case III: Fuse-recloser coordination

Consider the system studied in sub-section 4.3.2. It was shown that if a synchronous-machine DG is added at bus 1, this DG contributes to the fault and increases the current through the fuse and the recloser. For a SMDG larger than 1600 kW (see Figure 4-33), the fault current will be higher than 1475A for more than .1s and, consequently, the fuse will melt sooner than recloser's operation (the DG's parameters are the same as those in Case I). However, by utilizing the field discharge, the DG capacity can be larger than 1600kW without losing coordination. Figure 4-34 shows the impact of the field discharge circuit operation on the fault current for the case with 2400kW DG. As this figure shows, when no field discharge is applied, the fault current is higher than the coordination

boundary, and the fuse melts sooner than the recloser's operation. In contrast, when the field discharge is applied, the fault current is reduced below the coordination boundary in less than .1s, and as a result, the recloser operates sooner than the fuse, and the coordination is maintained. This result means that maximum DG capacity can be increased by 50%, from protection prospective, without any need to modify the protection system.

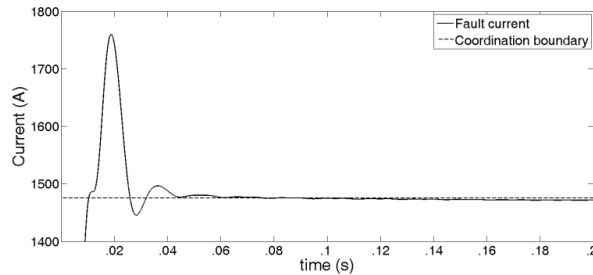


**Figure 4-33: Fuse and recloser fault current when a 1600kW DG is added at bus 1**

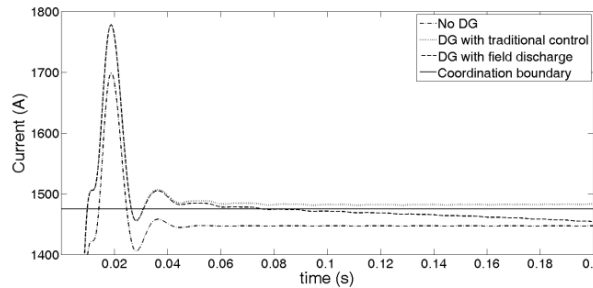


**Figure 4-34: Effect of field discharge circuit to eliminate the impact of a 2400kW DG on coordination**

#### 4.8 Impact of field discharge on voltage recovery

In this section, the post-fault performance of the SMDG when using the proposed field discharge strategy is compared with the performance of SMDG with traditional excitation strategy. The main aim is to demonstrate the impact of the field discharge on the voltage recovery in post-fault period.

Consider the network shown in Figure 4-13 with the SMDG operating at a unity power factor before the fault occurrence. When a three-phase fault happens at point F, the generator's d-axis flux suddenly decreases, and the machine starts absorbing the reactive power (see Figure 4-35,  $t=0 \sim t=.16$  Sec.). When the fault is cleared, another abrupt change in the reactive power happens, and then the

machine decreases its reactive power consumption (see Figure 4-35,  $t > 0.16$  Sec.). As Figure 4-35 reveals, the field discharge application decelerates the reactive power recovery. This result is due to the excessive reduction in machine's d-axis flux in comparison to that in the case using the traditional excitation strategy. This deceleration in the reactive power recovery leads to a slow, undesirable terminal voltage recovery in the post-fault period (see Figure 4-36).

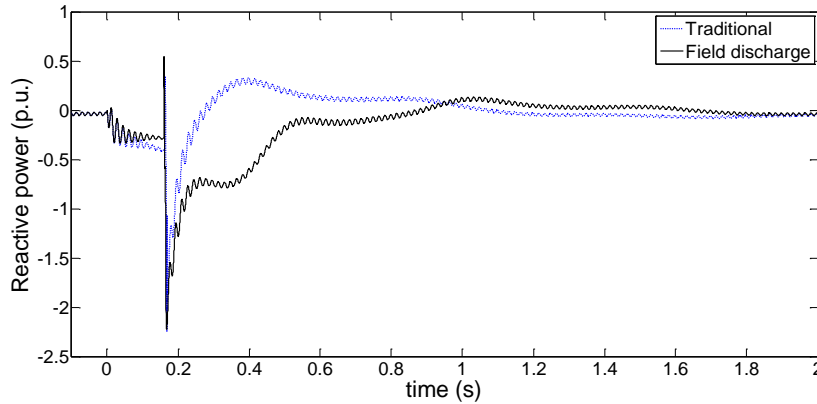


**Figure 4-35: Impact of field discharge on reactive power consumption during and after fault**

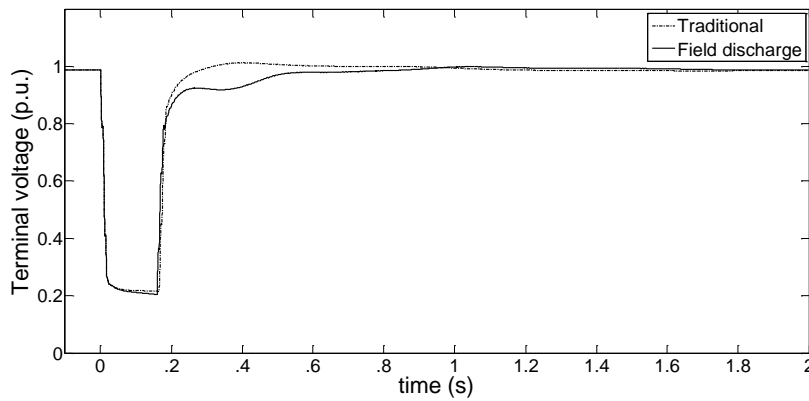


**Figure 4-36: Impact of field discharge on voltage recovery**

For some cases, the trade-off between minimizing the impact on the protection system and lengthening the reactive power recovery is acceptable. For example, in Figure 4-37, since the DG is close to the source, its impact on the feeder's voltage recovery can be negligible. On the other hand, in some other cases such as the one shown in Figure 4-38, although the DG is located far from the source and can significantly impact on the feeder's voltage recovery, the DG has no impact on the coordination, and field discharge is not needed.

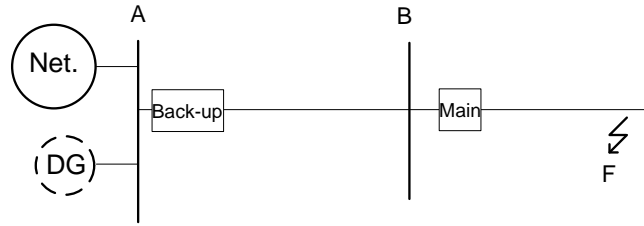


Figure 4-37: A distribution feeder with DG located close to the source

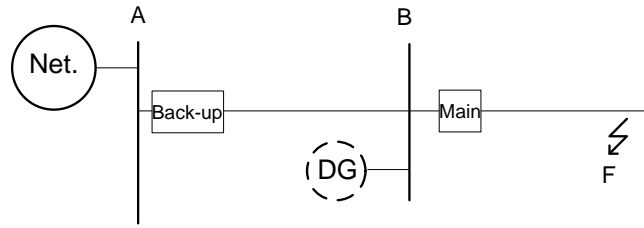


Figure 4-38: A distribution feeder with DG located far from the source

For the cases in which DG has a significant impact on both protection and voltage recovery, one idea to mitigate this impact is to limit the discharge time; i.e., to deactivate the field discharge circuit after a certain time while the fault still exists. The determination of the discharge circuit deactivation instance varies depending on the protection coordination constraints of each distribution system. Figure 4-39 to Figure 4-42 show the voltage recovery and the machine's performance during and after the fault for a .16 sec. fault when the field discharge is active for only .1 sec. As these figures reveal, limiting the discharge time can reduce the delay in the voltage recovery.

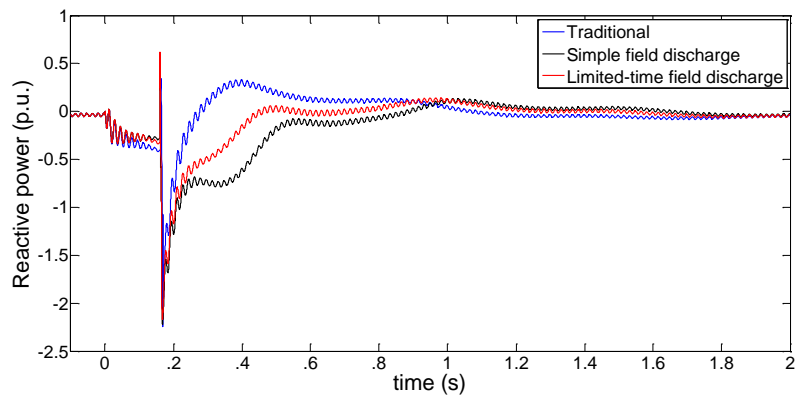
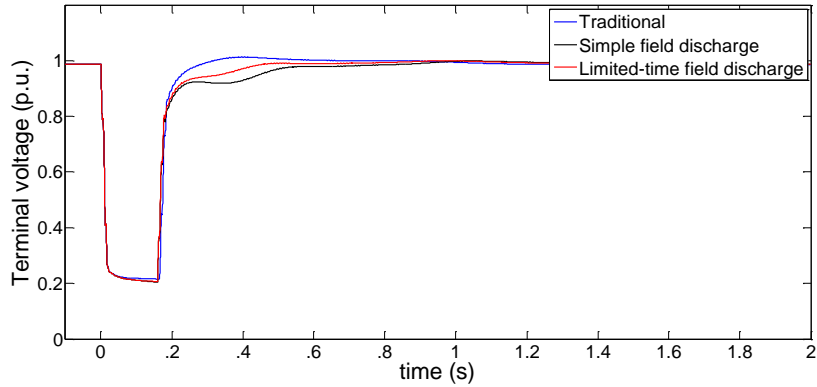
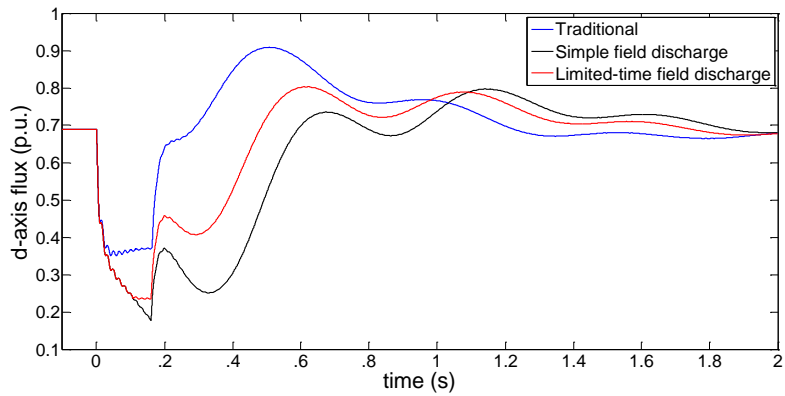


Figure 4-39: Reactive power recovery



**Figure 4-40: Terminal voltage recovery**



**Figure 4-41: d-axis flux**

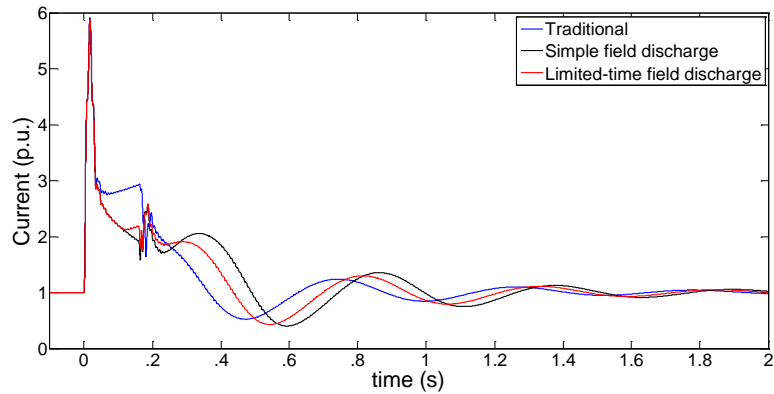


**Figure 4-42: d-axis flux**

Another idea for accelerating the voltage recovery after a fault is to modify the discharge circuit so that it can speed up the flux increase. In the previous subsections, it was shown that a series resistance with the field winding decreases machine's transient time constant. As a result, similar to the discharging process, a series resistance can be temporarily applied to the field circuit after the fault

clearance to accelerate the recovery process. Figure 4-43 shows the SMDG with the modified field discharge circuit.

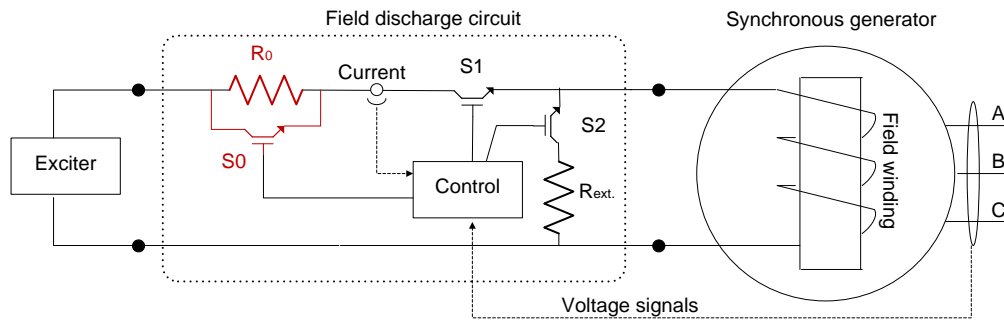


**Figure 4-43: SMDG with modified field discharge circuit**

In this circuit, during normal condition S0 and S1 are close, and S2 is open, so the exciter is directly connected to the field circuit. During the fault, S2 is closed, and S1 is opened to discharge the circuit. When the fault is cleared, S1 is closed, and S2 is opened to connect the exciter. At this moment, S0 is also closed, and S2 is opened to connect the exciter. At this moment, S0 is also opened. By this action, R0 is put in series with the field and exciter, and shortens the machine's transient time constant in order to accelerate building up the flux. After a certain amount of time (T1), S0 is closed, and the circuit returns to its normal condition.

To demonstrate the improvement achieved in the recovery process by modifying the discharge circuit, the system shown in Figure 4-13 was simulated, and the modified field discharge circuit was applied to the SMDG. In this study, the fault starts at  $t=0$  and is cleared at  $t=.16$  Sec. Therefore, ideally, S1 is open from  $t=0$  to  $t=.16$  Sec. In this period, S2 is closed to discharge the field circuit. After  $t=.16$  Sec. both S2 and S0 are open. Finally, S0 is closed at  $t=.25$  sec. Also, in this simulation,  $R_{ext}=R_0=6.25R_{field}$ . As Figure 4-44 reveals, the reactive power recovery is much faster when the modified circuit is applied. Likewise, as Figure 4-45 shows, voltage recovery is much faster in the case with a modified circuit than in the case with a simple discharge circuit. Also, Figure 4-46 shows how the additional resistance accelerates the building up of the flux. Figure 4-47 shows the output current during and after the fault for each excitation method, and finally, Figure 4-48 shows the exciter voltage (for the IEEE type 1 excitation system).

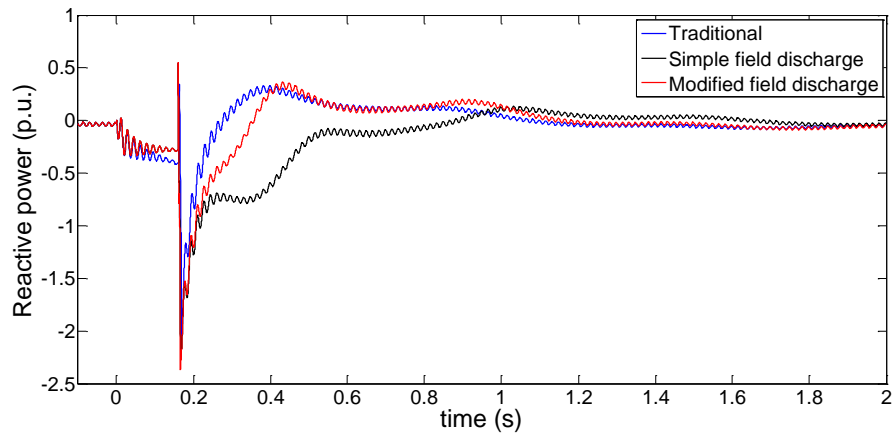


Figure 4-44: Reactive power recovery

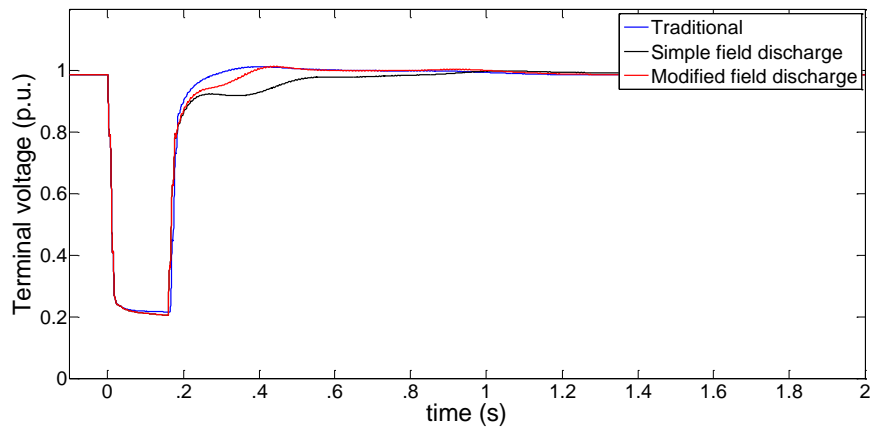


Figure 4-45: Terminal voltage recovery

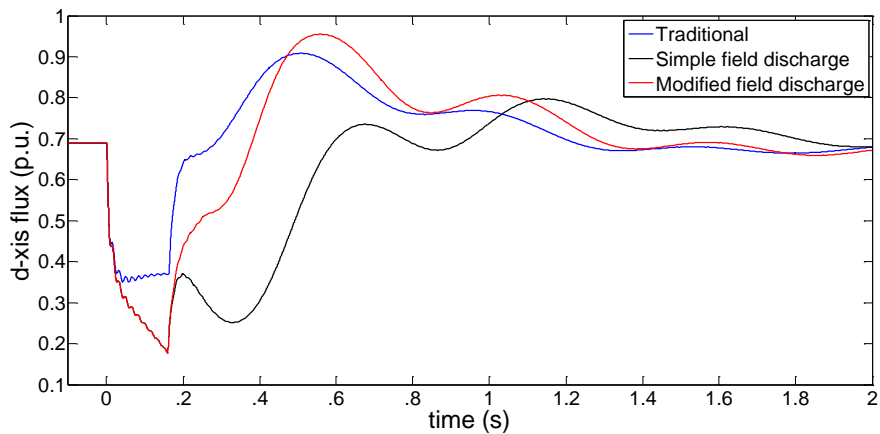


Figure 4-46: d-axis flux

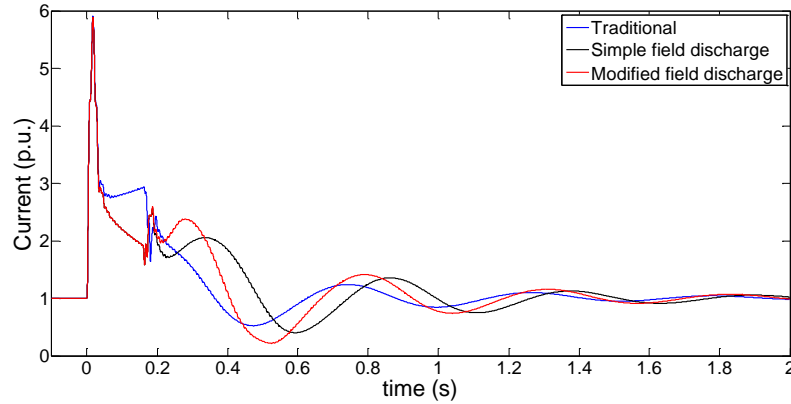


Figure 4-47: Output current

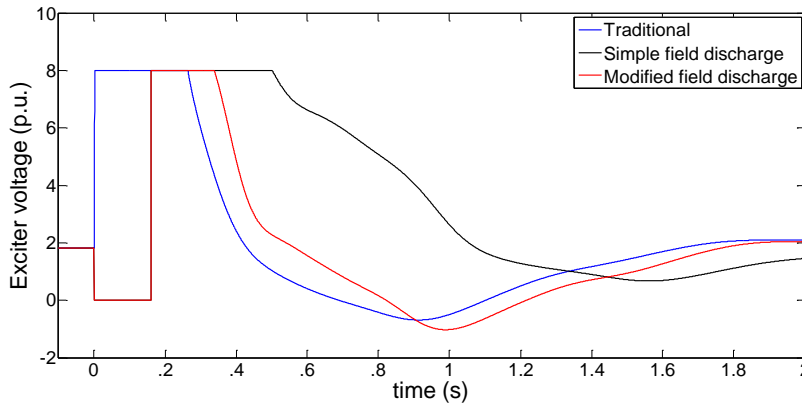


Figure 4-48: Exciter voltage

#### 4.9 Impact of field discharge on generator's stability

In practical conditions, the generator's input power can be assumed to be constant during the fault. Under this condition, the application of the field discharge circuit may or may not increase the rotor angle deviation from its steady-state value in comparison to traditional excitation control. In the following paragraphs, the effect of the field discharge on the rotor angle stability will be discussed.

The rotor angular velocity and, consequently, the rotor angle deviation from the steady state can be obtained from the following equation, which is known as the generator's swing equation [60]:

$$\frac{2H}{\omega_{syn}} \omega_{p.u.}(t) \frac{d\omega(t)}{dt} = P_{mech,p.u.}(t) - P_{elec,p.u.}(t) \quad (4-65)$$

where  $\omega_{p.u.}(t)$  is the rotor's per-unit angular speed,  $P_{mech,p.u.}(t)$  is the per-unit mechanical power of the prime mover (the generator's input power),  $P_{elec,p.u.}(t)$  is the per-unit electric output power of the generator,  $\omega_{syn}$  is the synchronous angular speed, and  $H$  is the inertia constant. Although for the fault cases, this equation can be solved only numerically, it can help in interpreting the sample simulation result and in reaching a conclusion.

For 3-phase faults near the generator, the voltages at the terminals are almost zero. As a result, regardless of the excitation control method, the average of  $P_{elec,p.u.}(t) \approx 0$ , and rotor angle deviations during the fault are the same for the case with the traditional excitation control and the case with the field discharge. For further illustration, the network shown in Figure 4-49 was simulated. This network is a 25 kV distribution system with  $Z_{source} = (1.625 + j5.5187)\Omega$  and  $Z_{line} = (.24 + j.26)\Omega/\text{km}$ . The generator's parameters are the same as those in the previous section, and its inertia constant is 1.5 sec. Figure 4-50 shows the output electric power and rotor angle deviation during and after a .1 sec. 3-phase fault at bus 1. As figure reveals, both the output power and rotor angle deviation match for both cases during the fault ( $t=0 \sim t=.1$  sec.).

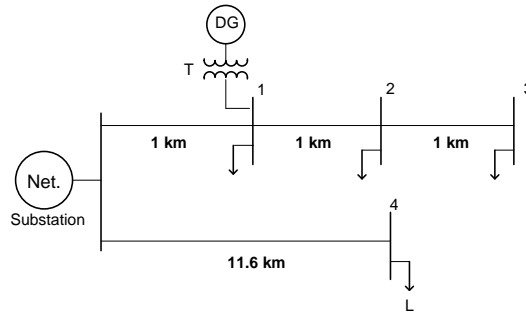


**Figure 4-49: Sample distribution network simulated for stability studies**

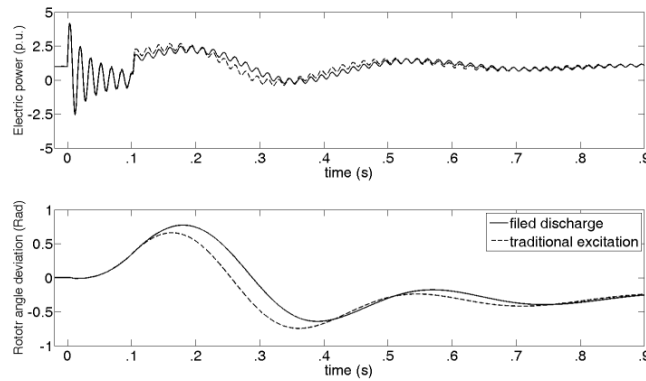


**Figure 4-50: Generator’s output current and rotor angle deviation for .1 sec. 3-phase fault at terminals**

When the fault is distinguished at  $t=.1s.$ , the generator in both cases generates the electric power. However, in the field discharge case, the average of  $P_{elec.,p.u.}(t)$  from  $t=.1s$  to  $t=.2s$  is lower than that in the traditional excitation case. In the field discharge case, after the fault the machine has a lower  $d$ -axis flux linkage (see Figure 4-51) and starts to build it up. Thus, it can produce lower synchronizing power at the beginning of the post-fault period. Consequently, the rotor angle deviation is higher in this case. The lower synchronizing power at the beginning of the post-fault period slightly decreases the Critical Clearing Time (CCT) for the fault near the terminals. For example, for a 5MW generator with  $H=1.5s$ , the CCT for traditional excitation is 145 ms, and for the field discharge with  $k=6.25$ , the CCT is 135ms (10ms reduction).

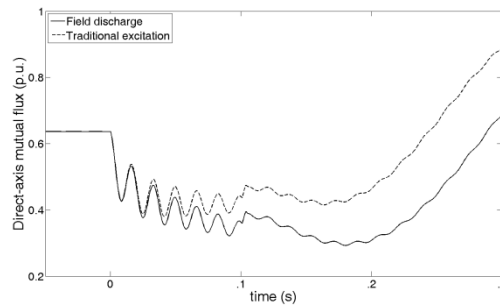


**Figure 4-51: Generator’s  $d$ -axis flux during and after fault**

For farther faults, because the voltages at the terminals are not zero,  $P_{elec.,p.u.}(t) > 0$  during the fault. As a result, the CCTs are higher than those in the

cases in which a fault occurs at the terminals. However, in the case with the field discharge, the machine generates less electric power during the fault than the case with traditional excitation. Consequently, rotor angle deviation during the fault is larger in this case, and the reduction in the CCT due to applying the field discharge is higher than when the fault occurs at the terminals. Figure 4-52 shows the output power and rotor angle deviation of generator when a .2 sec. 3-phase fault occurs at bus 4 (12.6 km away from the generator) of the simulated network. In this case, the CCTs are 365ms and 245ms for the traditional excitation and the field discharge, respectively.

Table 4-11 summarizes the CCTs for the faults at different buses in the simulated system. As this table reveals, in theory, for the farther faults the difference between the CCTs of the constant excitation and field discharge is higher. However, in practice, when the fault is too far from the generator, the DG unit barely contributes to the fault and has no impact on the coordination. Consequently, the field discharge is not applied in such cases.

To sum up, the field discharge is applied for close faults, to which the generator has high contribution. In such faults, the effect of the field discharge application on the CCT is low enough to be tolerated. On the other hand, for farther faults, the generator makes a small contribution. So, the field discharge is not needed. Consequently, the reduction in the CCT due to the application of the field discharge is not a concern with these faults.

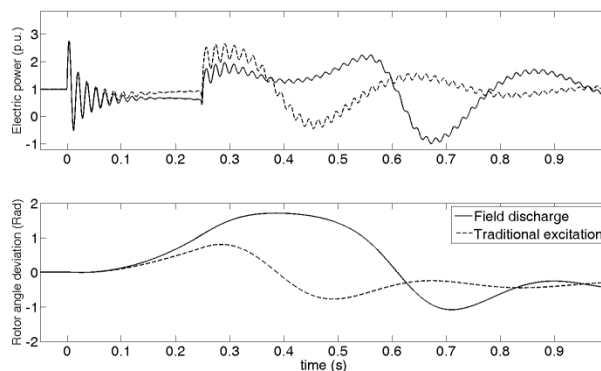


**Figure 4-52: Generator’s output power and rotor angle deviation for .2 sec. 3-phase fault 8.1 km away from generator**

**Table 4-11: CCT for 3-phase solid fault at different busses**

	CCT (ms)	
	Traditional excitation	Field discharge (k=6.25)
<b>Bus 1</b>	145	135
<b>Bus 2</b>	165	145
<b>Bus 3</b>	180	155
<b>Bus 4</b>	365	245

#### 4.10 Conclusion

In this chapter, the contribution of SMDGs to the fault current was analyzed, and their impact on the O.C. coordination was investigated. From both the mathematical analysis and the simulations, the following conclusions are made:

1. During the SMDG's sub-transient response, the machine's fault current is 4~8 p.u. and lasts for up to 3 cycles. The damper windings' parameters are the dominating factors in this period.
2. During the SMDG's transient response, the machine's fault current is 3~5 p.u. This part of the machine's response gradually decays with a transient time constant in the range of 1-2 sec. Field winding's parameters are the dominating factors in this period. This period coincides with the operation of the major O.C. devices in the distribution system, and this part of the machine's response can significantly impact on the coordination.
3. After the transient response, the steady state response appears. The magnitude of the current is around the rated current in this period.
4. In order to restrict the machine's fault current contribution in the transient period and, consequently, to mitigate the impact of the machine on the O.C. protection coordination, the field discharge application was proposed. This circuit disconnected the machine's excitation and decreased the machine's transient time constant. As a result, the machine's fault current decayed faster, and no steady state current existed.

5. It was shown that applying the field discharge circuit sufficiently reduced the generator's contribution to the fault current, and as a result, prevented miscoordination when short time-delay and/or inverse-time O.C. relays were involved.
6. A design procedure was proposed for the field discharge circuit, and this circuit was applied to the simulated SMDG. The case studies showed the proposed method significantly increased the SMDG's compatibility with the distribution system by mitigating its impact on the protection system's coordination.
7. The impact of field discharge application on the post-fault voltage recovery and also on the generator's stability was analyzed. The results showed that the field discharge undesirably delayed the voltage recovery. Therefore, mitigations were proposed to address this concern.

# Chapter 5

## Harmonic Analysis of DFIG-based Wind Farms

In the previous chapters, the impact of DGs on the O.C. protection was discussed, and mitigation methods were proposed. In this chapter, the main focus is on the power quality impact of DGs, specifically wind energy systems. Since the Doubly-Fed Induction Generator (DFIG) is one of the most popular generator types used in the wind energy systems, a harmonic analysis is presented for DFIGs during balanced steady state operation and a harmonic model is proposed for DFIG-based wind farms which can be used instead of their detailed models in power system harmonic studies.

The modelling methodology and its prerequisites are presented in Section 5.1. Next, the sinusoidal Pulse-Width Modulation (PWM) switching technique for 3-phase converters is reviewed in Section 5.2. In Section 5.3, a harmonic modelling method is proposed for DFIG-based wind systems. Section 5.4 covers the simulation results, which verify the modelling. Next, a method to estimate the parameters required for calculating the average harmonic voltages and currents is proposed in Section 5.5. Section 5.6 presents the determination of the worst-case harmonic scenario. Next, the non-characteristic harmonics are introduced and investigated in Section 5.7. Section 5.8 presents a comparison between the harmonic emissions from DFIG-based wind farms and those from other harmonic sources. The conclusions are presented in Section 5.9.

### 5.1 Methodology

Figure 5-1 shows a DFIG-based wind farm. In this figure, one DFIG system is shown in detail while the other DFIG systems are shown as boxes. As this figure reveals, each DFIG system consists of a wound-rotor induction machine and two converters sharing a DC link. Figure 5-2 shows the equivalent circuit of the DFIG at the fundamental frequency. In this figure,  $s$  is the slip at the fundamental frequency and can be calculated by using (5-1).

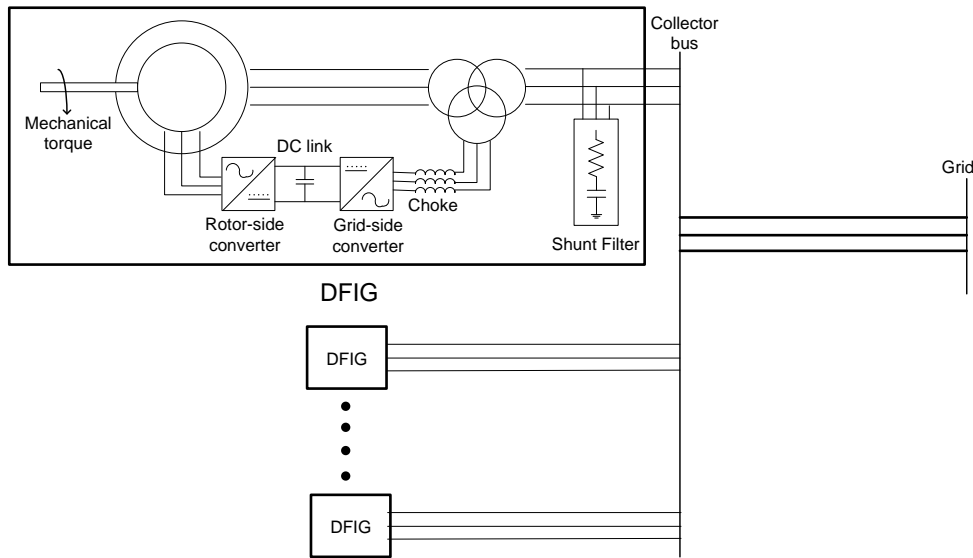


Figure 5-1: DFIG-based wind farm structure

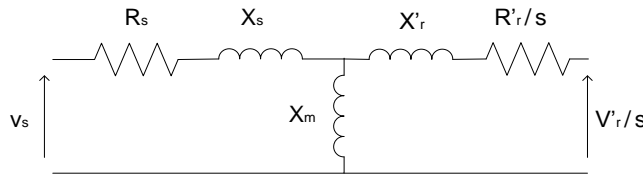


Figure 5-2: DFIG's equivalent circuit at fundamental frequency

$$s = \frac{f_s - f_m}{f_s} \tag{5-1}$$

In a DFIG system, the slip can be in the range of  $\pm 0.3$ . In other words, the DFIG is able to operate at both super- and sub-synchronous speeds (in the wide operation speed range, 70~130% of the synchronous speed). In the super-synchronous speed operation, the power is delivered through both the stator and rotor to the network. During the sub-synchronous speed operation, the power is delivered from the stator to the grid, while the converters inject some power (up to

30% of the stator's power) from the grid into the rotor (see subsection 5.5.1 for further explanation). The power injection/consumption through converters can be up to 30% of DFIG's rated power.

In a DFIG-based wind system, the Rotor-Side Converter (RSC) controls the machine's torque by injecting the appropriate voltage into the rotor at its frequency while the Grid-Side Converter (GSC) keeps the DC link voltage constant. In other words, if the GSC control is ideal, the dc link's voltage is ripple free. Consequently, the converters can be considered as two decoupled sources shown in Figure 5-3. In Section 5.2, it is shown that each source is a periodic PWM pulse train, which can be decomposed to a double Fourier series. Each series includes a fundamental frequency component and harmonic components at the odd sidebands of the converters' switching frequencies and their multiples. The harmonic modelling method presented in this chapter is based on the decoupling of the converters and decomposing each converter's pulse train to a Fourier series.

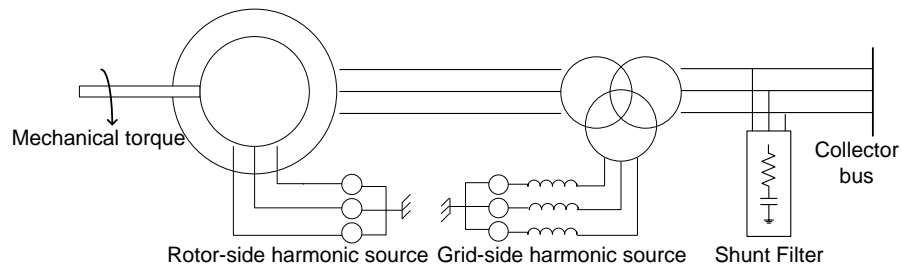


**Figure 5-3: DFIG's equivalent circuit for harmonic analysis**

Usually, the converters' switching frequencies are higher than 1 kHz. As a result, low-order harmonic voltages are not expected to appear at the converters' terminals and converters are not supposed to interact with the grid at low order harmonic frequencies. However, in the simulations these non-characteristic components appeared. Moreover, the DC link voltage was not ripple-free. This results cast doubt on the decoupling assumption, so, it was important to investigate whether or not there any interaction occurred between the grid and converters at low order harmonic frequencies. Hence, the sensitivity of components of DC link voltage and low-order components of the voltages at the

terminals to the changes in the background harmonic voltages at the grid was studied in a sample system (which is fully described in 5.4.1). Four scenarios were simulated. In the first scenario, no background harmonics were present in the grid. In the second scenario, the harmonic spectrum of the voltages measured at a 144kV substation in the Calgary area was used as the grid’s background harmonics (see Table 5-1). In the third scenario, the amplitude of the background harmonics in scenario 2 was decreased by 50%. Finally, in the last scenario, the amplitude of grid’s background harmonic voltages was 130% of those in the second scenario.

**Table 5-1: Sample spectrum for background harmonic voltages in Scenario 1**

<b>Harmonic order</b>	<b>Amplitude (% of rated voltage)</b>	<b>Angle in phase <i>a</i> (degree)</b>
5 <sup>th</sup>	1.16	-258
7 <sup>th</sup>	0.18	-33.7
11 <sup>th</sup>	0.07	-18.2
13 <sup>th</sup>	0.02	-289

Figure 5-4 shows the DC link voltage, Figure 5-5 shows its zoomed-in version, and Figure 5-6 shows the harmonic spectrum of DC link voltage under different scenarios. As Figure 5-6 reveals, the major components are low order (in range of 0~1 kHz, less than that of the switching frequencies). These harmonics are available even in the 0% background harmonic scenario. This result means that these components are caused by the DFIG’s converters and are not from the grid (In fact, they are non-characteristic harmonics. The source of these harmonics is discussed in 0 5.7). Besides, Figure 5-7 reveals the changes in these components due to the changes in the background distortion have an arbitrary pattern.

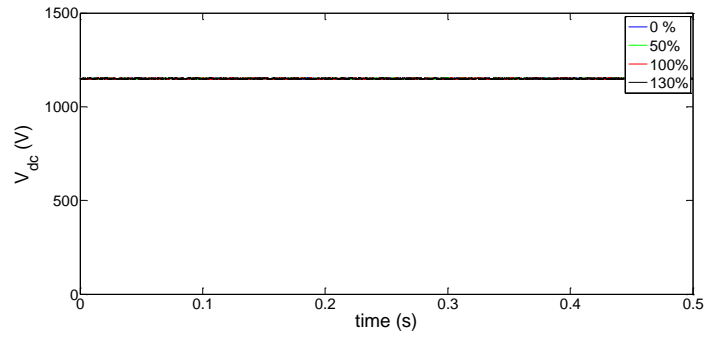


Figure 5-4: DC link voltage

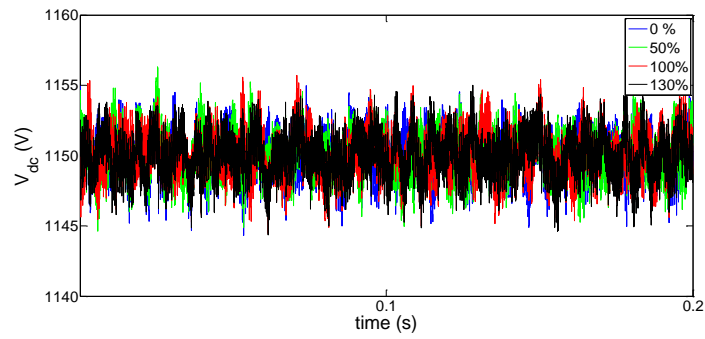


Figure 5-5: Zoomed DC link voltage

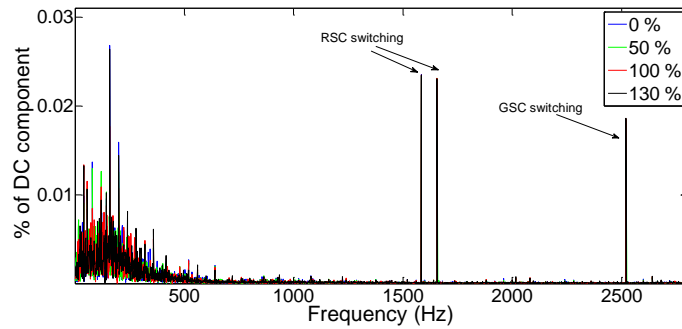


Figure 5-6: Spectrum of DC link voltage

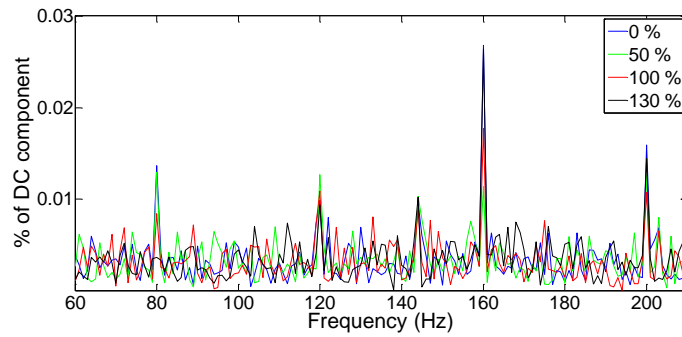


Figure 5-7: Spectrum of DC link voltage in lower frequencies

Figure 5-8 shows the integer harmonics of the voltage at the GSC's terminals (before the choke in Figure 5-1). As this figure reveals, these components show negligible sensitivity to the background harmonics. They were also present in the 0% background harmonic voltages scenario, and their changes were negligible in all scenarios from the 0% scenario to the 130% scenario. In other words, no significant interaction occurred between the converters and the grid at these frequencies. This result means that the DC link can be decoupled and each converter can be modeled as an independent harmonic voltage source.

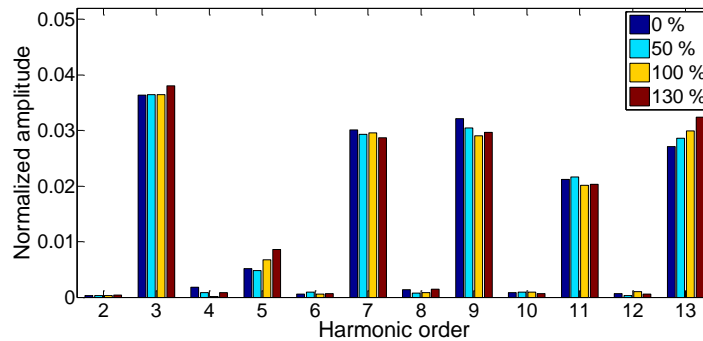
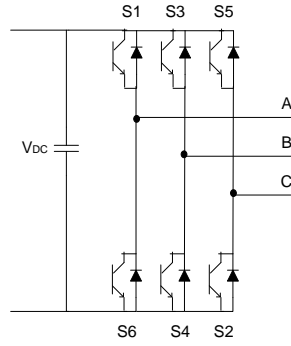


Figure 5-8: Integer harmonics of GSC's terminal voltage

## 5.2 Sinusoidal PWM switching technique

The majority of DFIGs utilize the sinusoidal PWM switching technique for both RSC and GSC. Since the switching technique of converters is a key factor in the harmonic emissions of a wind system, sinusoidal PWM switching for a 3-phase converter is reviewed in the following paragraphs.

Figure 5-9 shows a 3-phase converter, and Figure 5-10 shows its modulation signals. For each phase, when the reference signal is higher than that of the carrier ( $v_{ref} > v_{cr}$ ), the upper switch in Figure 5-9 is on (S1, S3 or S5). Otherwise, the lower switch is on (S6, S4 or S2). Figure 5-11 shows the state of S1 in one cycle. In addition, as Figure 5-10 shows, the reference signals are displaced by  $120^\circ$ . This displacement results in balanced phase-to-phase waveforms at the terminals (see Figure 5-12). In this technique, the phase and amplitude of the fundamental voltage can be controlled directly by adjusting the amplitude and phase of the reference signals.



**Figure 5-9: Three-phase voltage source converter’s structure**

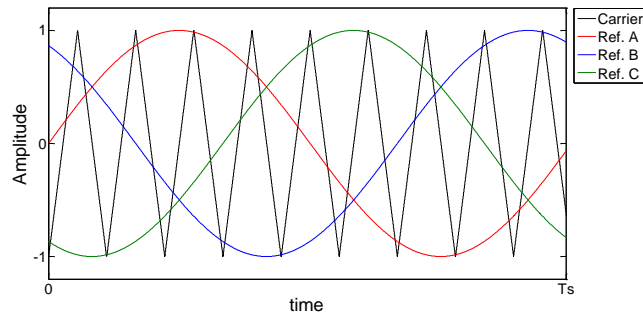


**Figure 5-10: Carrier and reference signals in 3-phase sinusoidal PWM scheme**

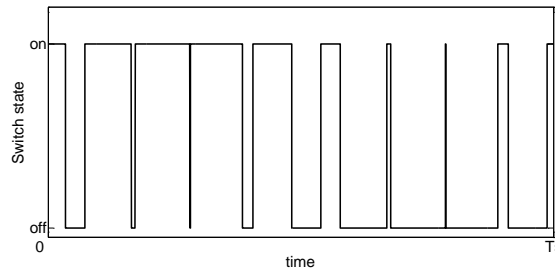


**Figure 5-11: Switching states of S1 during a period**

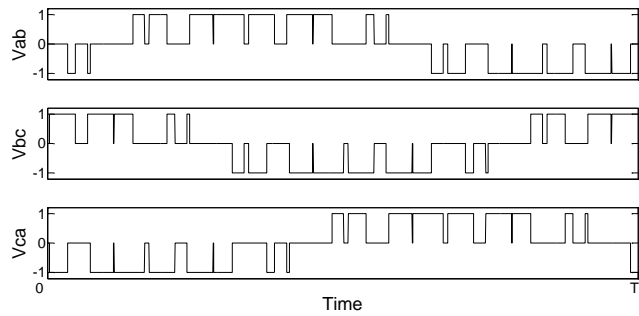


**Figure 5-12: Line-line voltages at converter’s terminals**

In 3-phase sinusoidal PWM switching, the pulse train of S1 can be presented as the Double Fourier series of (5-2) [71]-[75]. For switches S3 and S5,  $\omega_1 t$  should be replaced by  $\omega_1 t - 2\pi/3$  and  $\omega_1 t - 4\pi/3$ .

$$\begin{aligned}
 S1(t) &= \frac{M}{2} \sin(\omega_1 t) \\
 &+ \frac{2}{\pi} \sum_{m=1}^{\infty} J_0(mM \frac{\pi}{2}) \cdot \sin\left(m \frac{\pi}{2}\right) \cdot \sin(m\omega_c t) \\
 &+ \frac{2}{\pi} \sum_{m=1}^{\infty} \sum_{n=-\infty}^{\infty} \frac{1}{m} J_n(mM \frac{\pi}{2}) \cdot \sin\left((m+n) \frac{\pi}{2}\right) \cdot \sin((m\omega_c + n\omega_1)t)
 \end{aligned} \tag{5-2}$$

where  $M$  is the amplitude modulation ratio (the ratio of the peak reference signal to the peak carrier signal),  $J_n$  is the Bessel function of the first kind,  $\omega_1$  is the angular velocity at the fundamental frequency, and  $\omega_c$  is the angular velocity at the carrier's frequency.

For a general DC link voltage  $v_{dc}(t)$ , phase-to-phase voltages can be presented in terms of switch states. For example [73]-[75]

$$\begin{aligned}
 v_{ab}(t) &= v_{dc}(t)(S1(t) - S2(t)) = (V_{dc} + v_{ripp.}(t))(S1(t) - S2(t)) \\
 &= V_{dc} \left[ \frac{-\sqrt{3}M}{2} \sin(\omega_1 t) - \sum_{m=1}^{\infty} \sum_{n=-\infty}^{\infty} \frac{4}{m\pi} J_n(mM \frac{\pi}{2}) \cdot \sin\left((m+n) \frac{\pi}{2}\right) \cdot \sin\left((m\omega_c + n\omega_1)t - \frac{n\pi}{3}\right) \right] \\
 &+ v_{ripp.}(t) \left[ \frac{-\sqrt{3}M}{2} \sin(\omega_1 t) - \sum_{m=1}^{\infty} \sum_{n=-\infty}^{\infty} \frac{4}{m\pi} J_n(mM \frac{\pi}{2}) \cdot \sin\left((m+n) \frac{\pi}{2}\right) \cdot \sin\left((m\omega_c + n\omega_1)t - \frac{n\pi}{3}\right) \right]
 \end{aligned} \tag{5-3}$$

In the above equation,  $v_{dc}(t)$  is decomposed to its DC component  $V_{dc}$  and ripples  $v_{ripp.}(t)$ . For a converter with a well-designed DC link, during balanced normal operation the ripple is negligible in comparison to the DC component (less than 0.005 times the DC component in Figure 5-5). As a result, the phase-to-phase voltage can be approximated as follows:

$$\begin{aligned}
 v_{ab}(t) &= v_{dc}(t)(S1(t) - S2(t)) = (V_{dc} + v_{ripp.}(t))(S1(t) - S2(t)) \\
 &= V_{dc} \left[ \frac{-\sqrt{3}M}{2} \sin(\omega_1 t) - \sum_{m=1}^{\infty} \sum_{n=-\infty}^{\infty} \frac{4}{m\pi} J_n(mM \frac{\pi}{2}) \cdot \sin\left((m+n) \frac{\pi}{2}\right) \cdot \sin\left((m\omega_c + n\omega_1)t - \frac{n\pi}{3}\right) \right]
 \end{aligned} \tag{5-4}$$

Consequently, each converter can be modeled as an independent voltage source.

In a 3-phase converter with sinusoidal PWM switching, the carrier frequency  $f_c$  is usually selected so that the frequency modulation ratio ( $m_f$ ) is odd and a multiple of 3 [76].

$$m_f = \frac{f_c}{f_1} \tag{5-5}$$

As a result, only odd non-triple harmonics exist at the sidebands of  $m_f$  and its multiples (see Figure 5-13) [76]. In this figure, the amplitude of each harmonic component is a function of the amplitude modulation ratio ( $M$ ) and can be calculated by using (5-3). Table 5-2 presents the ratio of the RMS harmonic components to the dc voltage for different values of  $M$ .

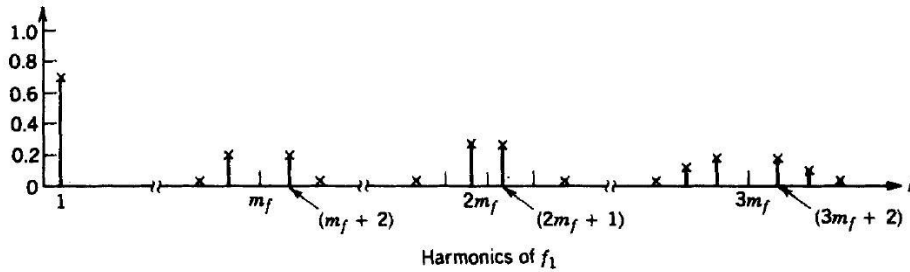


Figure 5-13: Harmonic spectrum of a 3-phase sinusoidal PWM switching [76]

Table 5-2:  $V_h/V_{dc}$  in PWM technique with large odd  $m_f$  multiple of 3

$h$	M				
	.2	.4	.6	.8	1
1	.122	.245	.367	.490	.612
$m_f \pm 2$	.010	.037	.080	.135	.195
$m_f \pm 4$	-	-	-	.005	.011
$2m_f \pm 1$	.116	.200	.227	.192	.111
$2m_f \pm 5$	-	-	-	.008	.020
$3m_f \pm 2$	.027	.085	.124	.108	.038

### 5.3 Harmonic modelling of DFIG system

The model presented in this section is derived under the assumption that the DC link voltage is constant and ripple-free. This assumption is reasonable for the balanced operation of converters during the steady state and will be justified

through simulation in the following sections. If the DC link voltage is assumed to be constant, the converters can be considered as two decoupled harmonic sources. As a result, the harmonic analysis can be conducted in three steps:

1. Only the GSC is modelled and the RSC is neglected. Then the harmonic currents are calculated.
2. Only the RSC is modelled and the GSC is neglected. Then the harmonic currents are calculated.
3. The total harmonic spectrum is obtained as the superposition of the harmonic currents calculated in the first two steps.

### 5.3.1 Harmonic modelling of GSC

The fundamental frequency of GSC is 60 Hz. As a result,  $m_f$  can be calculated as follows:

$$m_{f,GSC} = \frac{f_{sw}}{60} \quad (5-6)$$

The, major harmonic orders can be obtained from Figure 5-13, and the magnitude of the harmonic voltages at the converter's terminals can be obtained from (5-3) for a given set of  $V_{dc}$  and  $M$ . The GSC's equivalent circuit for  $h$ -th harmonic component is as shown in Figure 5-14.

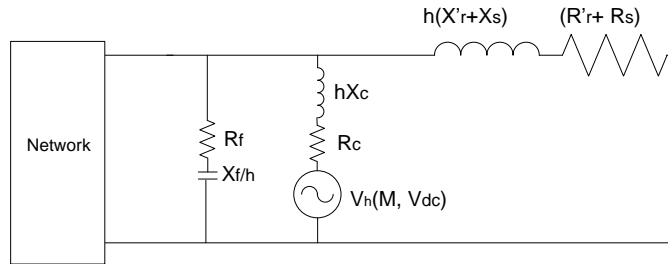


Figure 5-14: Harmonic modelling of GSC at its  $h_m$  harmonic

Note that  $X_f$  and  $R_f$  are the reactance and resistance of the shunt filter, respectively, and  $X_c$  and  $R_c$  are reactance and resistance of the choke, respectively. In this model, the magnetization branch of the DFIG is neglected.

As an example, consider a GSC with  $f_{sw}=2.7\text{ kHz}$ ,  $M=.8$  and  $V_{dc}=1150\text{V}$ . In this case,  $m_f=45$ , and the major harmonic voltages are tabulated in Table 5-3. By

using Table 5-3 and Figure 5-14, the harmonic currents (due to the GSC's operation) can be calculated.

**Table 5-3:  $V_h$  in PWM technique with  $m_f=45, f_{sw}=2.7\text{kHz}, M=.8$  and  $V_{dc}=1150\text{V}$**

$h$	<i>Freq. (Hz)</i>	$V_h$
$1$	$60$	$563.5$
$43^{\text{th}}/47^{\text{th}} (m_f \pm 2)$	$2580/2820$	$155.25$
$41^{\text{st}}/49^{\text{th}} (m_f \pm 4)$	$2460/2940$	$5.75$
$89^{\text{th}}/91^{\text{st}} (2m_f \pm 1)$	$5340/5460$	$220.8$

### 5.3.2 Harmonic modelling of RSC

For the rotor-side converter, the analysis is more complicated. First, the fundamental frequency of the converter is equal to the rotor's frequency ( $f_s \cdot f_m$ ). For example, for a DFIG rotating at 72 Hz and connected to a 60-Hz system, the RSC's fundamental frequency is -12 Hz. Indeed, the converter's fundamental frequency varies for different rotor speeds. Consequently, with a fixed switching frequency,  $m_f$  varies. Thus, in the example, for  $f_{sw}=1620$  Hz,  $m_f$  would be  $1620/12=135$ . Then, the  $133^{\text{rd}}$ ,  $137^{\text{th}}$ ,  $269^{\text{th}}$ , and  $271^{\text{st}}$ , ... harmonic components would exist at the rotor side, i.e., at 1596 Hz, 1644 Hz, 3228 Hz, 3252 Hz, ... When they are referred to the stator, if the machine operates in the sub-synchronous mode, the mechanical frequency should be added to the frequencies of the positive sequence harmonics ( $h=6n+1$ ) or subtracted from the frequencies of the negative sequence harmonics ( $h=6n-1$ ). Otherwise, (if the machine operates in the super-synchronous mode) the mechanical frequency should be subtracted from the frequencies of the positive sequence harmonics ( $h=6n+1$ ) or added to the frequencies of the negative sequence harmonics ( $h=6n-1$ ). Thus, in the above example, the harmonics at the stator side will appear at 1524 Hz ( $1596-72$ ), 1716 Hz ( $1644+72$ ), ... As this example reveals, depending on the mechanical speed, inter-harmonics could exist.

Figure 5-15 shows the equivalent circuit for  $h$ -th harmonic generated by the rotor-side converter referred to the stator side. In this figure,  $s_h$  is the slip at the  $h$ -th harmonic frequency and can be calculated by using (5-7).

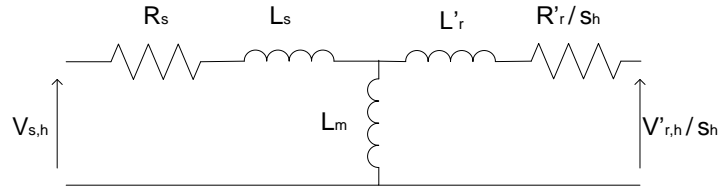


Figure 5-15: DFIG's equivalent circuit at  $h_{th}$  harmonic frequency

$$\begin{cases} s_h = \frac{h-(1-s)}{h}, h = (6k+1) \\ s_h = \frac{h+(1-s)}{h}, h = (6k-1) \end{cases} \quad (5-7)$$

Since  $h$  is relatively large and  $-.3 < s < .3$ ,  $s_h \approx 1$ . Also, the magnetization branch can be neglected. As a result, for harmonic studies, the RSC can be modeled as shown in Figure 5-16. Similar to the GSC, amplitudes of harmonic voltages can be obtained by using (5-2). In addition, when the harmonic voltages are referred to the stator side, their amplitudes should be multiplied by the stator-to-rotor turn ratio.

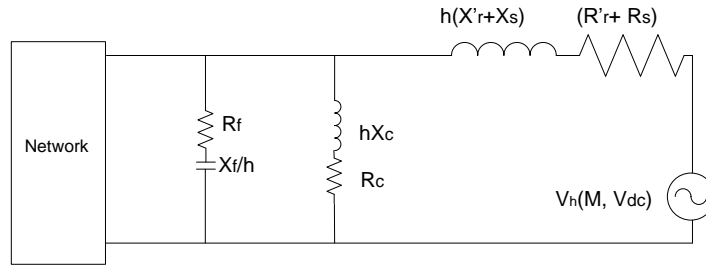


Figure 5-16: Harmonic modelling of RSC at its  $h_{th}$  harmonic

## 5.4 Simulation

In order to investigate the validity of the proposed harmonic model, a power system with a DFIG-based wind farm was simulated in MATLAB/Simulink. In the following paragraphs, the simulated system is introduced, and the simulation results are presented and compared with the results obtained from the harmonic modelling of DFIG.

### 5.4.1 Simulated system

The simulated system was prepared by Hydro-Quebec and presented as a demo in Simulink. Figure 5-17 shows the simulated system, and Figure 5-18

## Chapter 5: Harmonic Analysis of DFIG-based Wind Farms

shows the details of the DFIG wind farm. As Figure 5-17 reveals, the wind farm is connected to a 120 kV system via a 30 km 25 kV feeder. The wind farm consists of 6 DFIGs with rated voltage of 575 V and rated power of 1.5 MW (9MW total). As Figure 5-18 reveals, the GSC is connected to the grid through an inductor while the RSC is directly connected to the rotor. Also, a 120 kVAR shunt filter is connected to the stator's terminals of each DFIG (720kVar total). The main functional of these elements is to filter the high-frequency harmonic current and not to provide reactive power. A detailed representation of power electronics converters is used in this model. The PWM GSC's and RSC's switching frequencies are 2700 Hz and 1620 Hz, respectively. During the simulation, the wind speed is 15 m/s, which rotates the DFIG's rotor at 1.2 time the synchronous speed ( $s=-.2$ ).

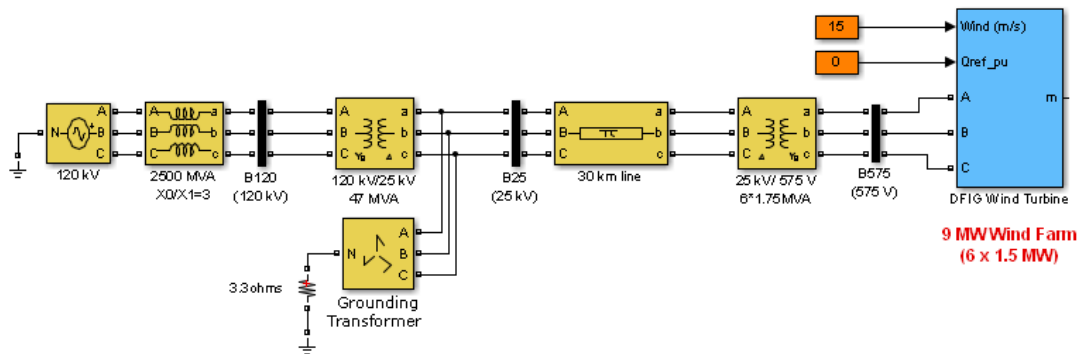


Figure 5-17: Simulated power system

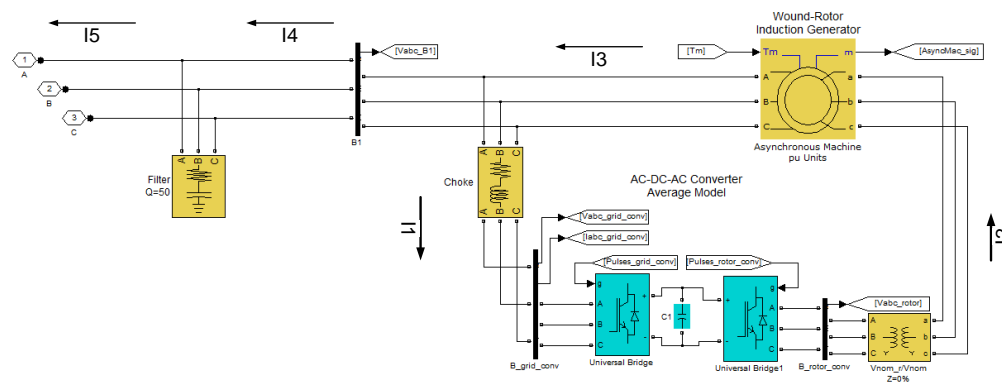


Figure 5-18: Details of wind farm simulation

**120 kV network**

$$Z_1=(.1+j)p.u., Z_0=3 Z_1, S_{base}=2500MVA$$

**120kV/25kV transformer**

$$S_{rated}=47MVA, X_1=X_2=0.08p.u., X/R=30, Yg/D$$

**Grounding transformer**

$$S_{rated} = 100MVA, Z_0=(.025+j0.75)p.u.$$

**25kV feeder**

$$r_1=.1153 \Omega/km, r_0=.413 \Omega/km, l_1=1.05 mH/km, l_0=3.32 mH/km, c_1=11.33 pF/km, \\ c_0=5.01 pF/km, Length: 30 km$$

**Wind farm's transformer**

$$S_{rated} = 10.5MVA, X_1=X_2=0.025p.u., X/R=30$$

**DFIGs**

Wind farm includes 6 parallel 1.5 MW DFIGs. For each DFIG:  $PF_{rated}=.9$ ,  $R_s=.023 p.u.$ ,  $R'_r=.016 p.u.$ ,  $X_s=.18 p.u.$ ,  $X'_r=.16 p.u.$ ,  $X_m=2.9 p.u.$ ,  $R_{choke}=.003p.u.$ ,  $X_{choke}=.3 p.u.$

**Shunt filter for each turbine**

$$Q_{rated}=120kVar, Quality\ factor\left(\frac{Q_{filter}}{P_{filter}}\right)=50,(R=.0551\ Ohm, C=936\mu F\ \omega_c=3kHz.)$$

**5.4.2 Simulation results**

Figure 5-19 shows the DC link voltage obtained from the simulation. As this figure reveals, the DC voltage contains ripples. However, the magnitude of the ripples never exceeds 0.005 of the DC component. Therefore, the assumption of constant DC link voltage was reasonable for the harmonic modelling.

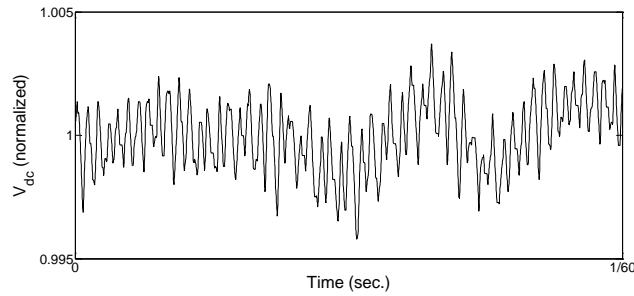


**Figure 5-19: DC link voltage**

Figure 5-20 shows the normalized harmonic spectrum of the GSC's current ( $I_1$  in Figure 5-18). As this figure reveals, the major harmonics are the odd sidebands of the GSC's switching frequency ( $m_f=2700/60=45$ ), which are 43<sup>rd</sup> and 47<sup>th</sup>, and also the sidebands of its multiples, which are 89<sup>th</sup> and 91<sup>st</sup>.

Figure 5-23 shows the normalized harmonic spectrum of the RSC's current ( $I_2$ ). As this figure reveals, the major harmonics are the odd sidebands of RSC's switching frequency ( $m_f=1620/12=135$ ), which are 133<sup>rd</sup> (1596 Hz) and 137<sup>th</sup> (1644 Hz), and also the sidebands of its multiples, which are 269<sup>th</sup> and 271<sup>st</sup>. Note that the fundamental current is at -12 Hz ( $f_{L,rotor}=s*f_{L,system}$ ). Moreover, there is no sign of interaction between the RSC and GSC in the harmonic spectrum.

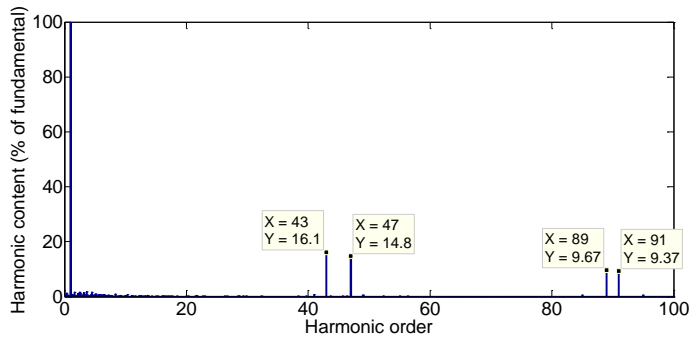


**Figure 5-20: Harmonic spectrum of GSC's current (% of converter's fundamental current)**

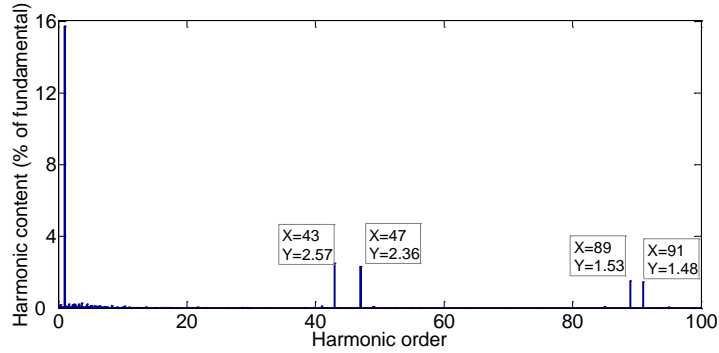


Figure 5-21: Harmonic spectrum of GSC's current (% of generator's fundamental current)

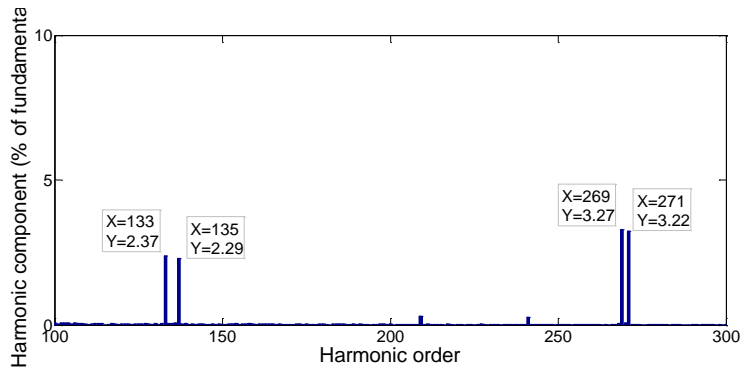


Figure 5-22: Harmonic spectrum of RSC's current (% of converters fundamental current, fundamental frequency=12 Hz)

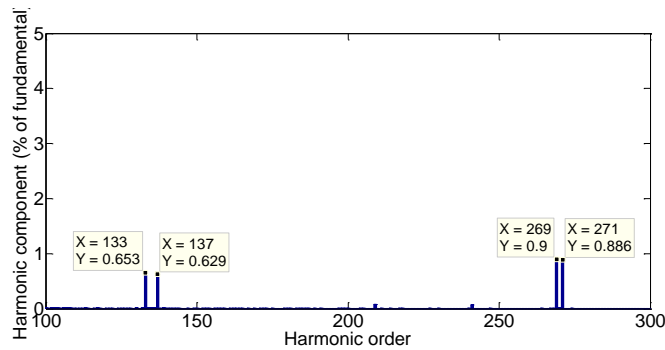


Figure 5-23: Harmonic spectrum of RSC's current (% of generator's fundamental current)

Another way to justify the decoupling of the DC link in the modelling is to compare the simulation results with the case in which the DC link's capacitor is replaced by an ideal DC voltage source in the presence of the background harmonic voltages in the grid. To do so, 1% background 43<sup>rd</sup> and 47<sup>th</sup> harmonic voltages and .5% 89<sup>th</sup> and 91<sup>st</sup> harmonic voltages were embedded in the simulated system. Table 5-4 and

Table 5-5 show this comparison for the harmonic spectra of GSC and RSC, respectively, with and without background harmonics. Diff.1 shows the differences without background harmonics and Diff.2 shows the differences with background harmonic voltages. As these tables reveal, the differences are negligible and, consequently, the assumption that the RSC and GSC are decoupled harmonic sources is valid.

Table 5-4: Major harmonic components of GSC current

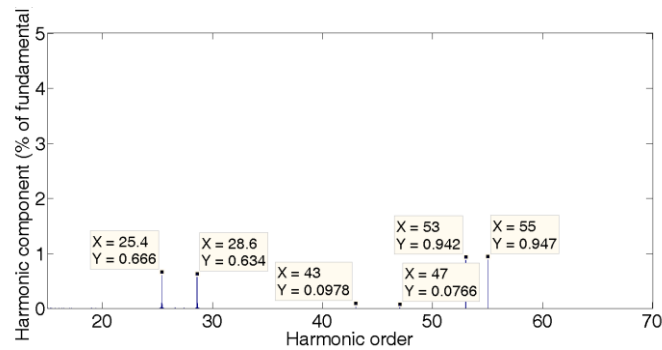
<i>h</i>	Harmonic content (% of converter's fundamental component)				Diff.1 (%)	Diff.2 (%)
	DC link with capacitor		DC link with ideal voltage source			
	no background	With background	no background	With background		
<b>43</b>	16.5	16.6	16.5	16.5	0	.6
<b>47</b>	15.1	14.3	15.3	14.2	1.3	.7
<b>89</b>	9.87	9.94	9.84	1	.3	1
<b>91</b>	9.61	9.73	9.65	9.71	.4	.2

Table 5-5: Major harmonic components of RSC current

<i>h</i>	Harmonic content (% of converter's fundamental component)				Diff.1 (%)	Diff.2 (%)
	DC link with capacitor		DC link with ideal voltage source			
	no background	With background	no background	With background		
<b>133</b>	.649	.652	.65	.652	.1	0
<b>137</b>	.622	.626	.624	.627	0.3	.2
<b>269</b>	.907	.907	.905	.907	0	0.2
<b>271</b>	.901	.903	.901	.901	0.2	0

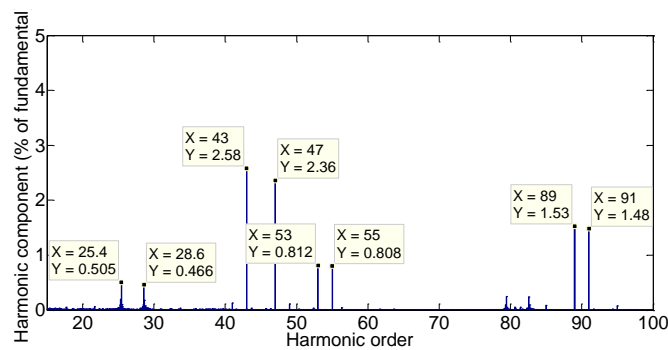
Figure 5-24 shows the normalized harmonic spectrum of the stator's current ( $I_3$ ). As this figure reveals, very small 43<sup>th</sup> and 47<sup>th</sup> harmonics appear in the stator's current, which are the results of the GSC's switching. On the other hand, the major harmonics in the stator currents are 1524, 1716, 3180 and 3300 Hz, which are induced by the RSC. As was explained in the previous section, the 1524 Hz component is the 1596 Hz component of the RSC which is induced to the stator and the rotor's mechanical frequency (72 Hz) is deducted (1524 = 1596-72). Likewise, the 1716 Hz component in the stator's current is actually the 1644 Hz

component of the RSC induced in the stator, and the rotor's mechanical frequency (72 Hz) is added ( $1716 = 1644 + 72$ ).



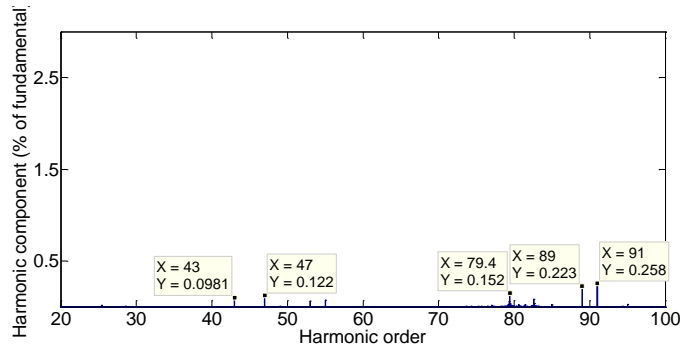
**Figure 5-24: Harmonic spectrum of stator's current**

Figure 5-25 shows the normalized harmonic spectrum of the wind farm's current before the shunt filter ( $I_4$ ). As this figure reveals, this current contains harmonics from the GSC and also from the RSC, induced in the stator.



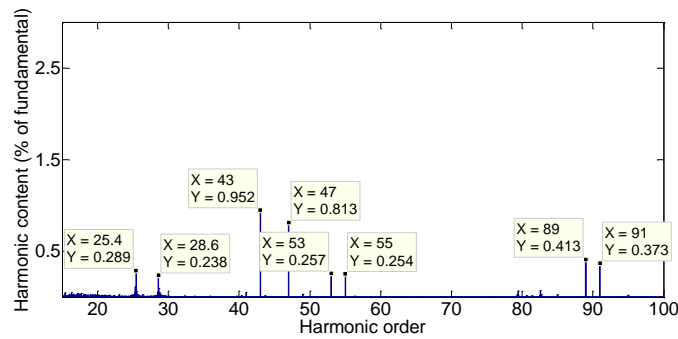
**Figure 5-25: Harmonic spectrum of  $I_4$**

Figure 5-26 shows the normalized harmonic spectrum of the wind farm's output current  $I_5$  (after the shunt filter). As this figure reveals, because of the shunt filter, this current contains very low harmonics components (the largest component is 0.26% of the fundamental).



**Figure 5-26: Harmonic spectrum of  $I_5$**

Figure 5-27 shows the harmonic spectrum of the line-to-line voltage at the wind farm’s connection point (the 575V side of the transformer). As this figure reveals, the magnitude of any harmonic component does not reach 1% of the fundamental component.



**Figure 5-27: Harmonic spectrum of voltage**

### 5.4.3 Comparison of the results

In this subsection, two sets of harmonic components of currents at two frequencies are presented as examples. One set is obtained from the detailed simulation and the other set is obtained from the proposed harmonic model of DFIG (Figure 5-35). These sets are compared to show the validity and accuracy of the proposed harmonic model. Note that for harmonic modelling, the amplitude of harmonic voltage sources in Figure 5-35 should be calculated from (5-2). In this case study,  $V_{dc}=1150V$ ,  $M_{GSC}=.82$ ,  $M_{RSC}=.59$ .

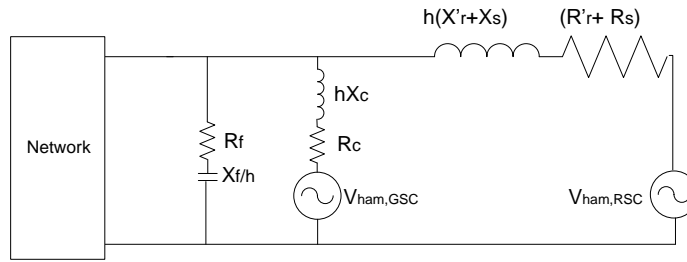


**Figure 5-28: Equivalent DFIG model**

The studied frequencies are 2580 Hz and 3300 Hz. The current components at 2580 Hz  $((m_{f,GSC}-2)*60Hz)$  are caused by the GSC, while the components at 3300 Hz  $((2m_{f,RSC}-1)*12Hz+72Hz)$  are caused by the RSC.

For the 2580 Hz components, since they are caused by the GSC, the model in Figure 5-14 should be used to calculate the currents. From (5-2),  $V_{ll,43th} = 1405 * 1150 = 161.58$  V. Table 5-6 shows the 2580 Hz current components obtained from the simulation and modelling. As this table reveals, the results from the modelling are in close agreement with the results from the simulation.

**Table 5-6: Harmonic components at 2580 Hz**

	RMS Harmonic component (A)	
	Modelling	Simulation
<b>GSC current (I<sub>1</sub>)</b>	165.21	163.01
<b>Stator current (I<sub>3</sub>)</b>	4.77	5.62
<b>Wind farm output current before shunt filter (I<sub>4</sub>)</b>	168.85	167.76
<b>Current injected to the grid (I<sub>5</sub>)</b>	6.34	6.37

For the 3300 Hz components, since they are caused by the RSC, the model in Figure 5-16 should be used to calculate the currents. From (5-2),  $V_{ll,269h} = 0.2268 * 1150 = 260.82$  V, which should be referred to stator side  $V'_{ll,269h} = 260.82$  V \*  $n_s/n_r = 75.94$  V. Table 5-7 shows the 3300 Hz current components obtained from the simulation and modelling. As this table reveals, the results from the modelling are in close agreement with those from the simulation.

**Table 5-7: Harmonic components at 3300 Hz**

	RMS Harmonic component (A)	
	Modelling	Simulation
<b>GSC current (<math>I_1</math>)</b>	1.5525	2.4
<b>Stator current (<math>I_3</math>)</b>	50.78	50.62
<b>Wind farm output current before shunt filter (<math>I_4</math>)</b>	51.56	52.32
<b>Current injected to the grid (<math>I_5</math>)</b>	4.51	4.47

## 5.5 Estimation of parameters

In previous sections, it was shown that all harmonic voltages and currents caused by a DFIG-based wind farm can be calculated by knowing  $V_{dc}$  and the amplitude modulation ratios of the DFIG's converters ( $M_{GSC}$  and  $M_{RSC}$ ). The main aim of this section is to propose methods to estimate typical values for  $V_{dc}$ ,  $M_{GSC}$  and  $M_{RSC}$  in a DFIG-based wind system. For this purpose, the stator and rotor powers in the steady state operation of DFIG systems must be estimated. In the following sub-sections, the steady state operation of DFIG systems is studied, and estimations for  $V_{dc}$ ,  $M_{GSC}$  and  $M_{RSC}$  are presented.

### 5.5.1 Stator and rotor powers

The mechanical power extracted by a wind turbine at wind speed  $v$  can be expressed as follows [77]:

$$P_{mech} = c_p(\lambda) \frac{\rho}{2} A v^3 \quad (5-8)$$

where  $\rho$  is specific air mass,  $A$  is the circular swept area, and  $c_p$  is the power coefficient. As (5-8) reveals,  $c_p$  is a function of the tip speed ratio  $\lambda$ , which is the ratio of the circumferential velocity of the turbine's blade tips and the wind speed. Figure 5-29 shows a typical  $c_p$  over  $\lambda$  curve. As this figure reveals, there is a tip speed ratio at which  $c_p$  has its maximum value. In other words, from this curve, we can find a rotor speed/slip at which the turbine produces maximum power at a certain wind speed. After determining this rotor speed, the optimum turbine torque can be obtained from (5-9). One of the main functions of the RSC

controller is to control the rotor voltage so that machine operates at this torque to ensure maximum wind power extraction.

$$\tau_{em} = \frac{P_{max}}{\omega_{mech}} \quad (5-9)$$

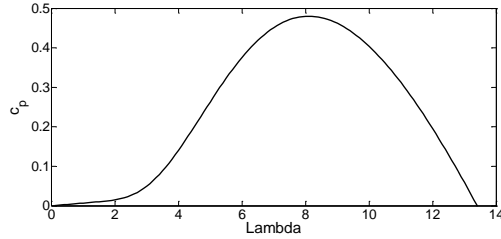


Figure 5-29: A typical  $c_p$  over  $\lambda$  curve

Figure 5-30 shows the power sharing between the stator and rotor in the DFIG system where the losses are neglected [77]. As this figure reveals, the stator power ( $P_s$ ) and rotor power ( $P_r$ ) can be obtained as follows:

$$P_r = sP_s \quad (5-10)$$

and

$$P_{mech} = P_s - P_r = (1-s)P_s \quad (5-11)$$

As a result,

$$P_s = \frac{1}{(1-s)} P_{mech} \quad (5-12)$$

and

$$P_r = \frac{s}{(1-s)} P_{mech} \quad (5-13)$$

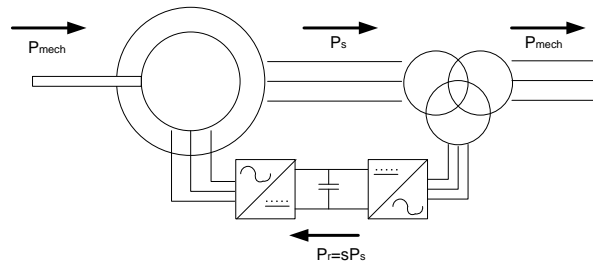
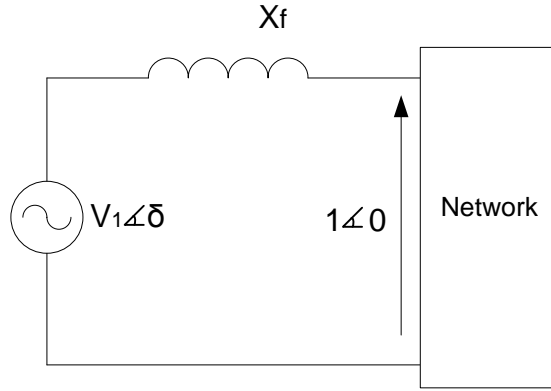


Figure 5-30: Power sharing in a loss-less DFIG system

### 5.5.2 Estimation of $V_{dc}$ and $M_{GSC}$

The main function of the GSC is to maintain the dc link voltage at a constant level by controlling the active power exchange between the network and DC link. Figure 5-31 shows the equivalent circuit of the GSC at the fundamental frequency during steady state. Note that in this figure, the series filter's resistance is neglected.



**Figure 5-31: Equivalent circuit of GSC at fundamental frequency during steady state**

The active and reactive powers transferred to the network can be expressed as

$$P_{GSC} = \frac{V_1}{X_f} \sin \delta \quad (5-14)$$

$$Q_{GSC} = \frac{V_1 \cos \delta - 1}{X_f} \quad (5-15)$$

For unity power factor operation,  $Q_{GSC} = 0$ . therefore:

$$\delta = \cos^{-1} \frac{1}{V_1} \quad (5-16)$$

From (15) and (17)

$$V_1 = \sqrt{(X_f P_{GSC})^2 + 1} \quad (5-17)$$

and since at steady state  $P_{GSC} = P_r$

$$V_1 = \sqrt{(X_f P_r)^2 + 1} \quad (5-18)$$

Thus, at an average wind speed, the GSC's fundamental voltage is obtained from (5-18). On the other hand,

$$V_1 = \frac{\sqrt{3}}{2\sqrt{2}} M_{GSC} V_{dc} \quad (5-19)$$

Therefore,

$$V_{dc} = \frac{2\sqrt{2}}{\sqrt{3}} \frac{\sqrt{(X_f P_r)^2 + 1}}{M_{GSC}} \quad (5-20)$$

As (5-20) reveals, there is only one equation for the two unknowns,  $V_{dc}$  and  $M_{GSC}$ , so, one of these parameters can be selected freely. For  $M_{GSC}$ ,  $0 < M_{GSC} < 1$ , and a higher  $M_{GSC}$  results in a lower dc link voltage (and, therefore, simpler and less costly implementation). However, an  $M_{GSC}$  close to 1 should be avoided to minimize the chance of overmodulation. As a result,  $M_{GSC} \approx 0.8$  is a reasonable assumption. Then,  $V_{dc}$  is obtained from (5-20).

### 5.5.3 Estimation of $M_{RSC}$

In subsection 5.5.1, the optimum torque (at which maximum power extraction happens) was obtained. Now, the rotor voltage referred to the stator side at this torque is obtained as follows [79]:

$$V_r^2 = \omega_r^2 \left[ \left( \frac{\omega_s \tau_{em} \sigma L_s L_r}{3pV_s L_m} \right)^2 + \left( \frac{V_s L_r}{\omega_s L_m} - \frac{Q_s \sigma L_s L_r}{3V_s L_m} \right)^2 \right] \quad (5-21)$$

where  $L_s$  and  $L_r$  are the stator and rotor inductances, respectively;  $L_m$  is the mutual inductance; and  $\sigma$  is the leakage factor ( $\sigma = 1 - \frac{L_m^2}{L_s L_r}$ ).

At the unity power factor operation

$$V_r = \omega_r \sqrt{\left[ \left( \frac{\omega_s \tau_{em} \sigma L_s L_r}{3pV_s L_m} \right)^2 + \left( \frac{V_s L_r}{\omega_s L_m} \right)^2 \right]} \quad (5-22)$$

Now, the voltage at the RSC can be obtained as follows:

$$V_{RSC} = \omega_r \left( \frac{N_r}{N_s} \right) \sqrt{\left[ \left( \frac{\omega_s \tau_{em} \sigma L_s L_r}{3pV_s L_m} \right)^2 + \left( \frac{V_s L_r}{\omega_s L_m} \right)^2 \right]} \quad (5-23)$$

Finally, from the PWM principles,  $M_{RSC}$  can be obtained as follows:

$$M_{GSC} = \frac{2\sqrt{2}}{\sqrt{3}} \frac{V_{RSC}}{V_{dc}} \quad (5-24)$$

Now all the parameters required to calculate the harmonic voltages and currents are available. By calculating these parameters at an average wind speed and using them in the method proposed in the modelling section, the typical harmonic spectra of the voltages and currents can be obtained for a DFIG-based wind farm.

## 5.6 Illustrative example

### 5.6.1 Study scenario

In the previous section, a method was proposed to estimate the average harmonics in a DFIG-based wind system. However, an average wind speed and a  $c_p$  over  $\lambda$  curve were required for that method. In this sub-section, rough estimations for  $M_{GSC}$  and  $M_{RSC}$  are provided to determine the worst case in terms of harmonics. In contrast to previous section, there is no need to have wind speed or turbine specifications data.

In the worst case, both the GSC and RSC produce maximum harmonic voltages at the lowest harmonic frequencies, which are the first sidebands of the switching frequencies ( $m_f \pm 1$ ). Figure 5-32 shows the normalized amplitude of these components for different values of the amplitude modulation ratio in a sinusoidal PWM switching scheme. This figure is obtained from (5-3).

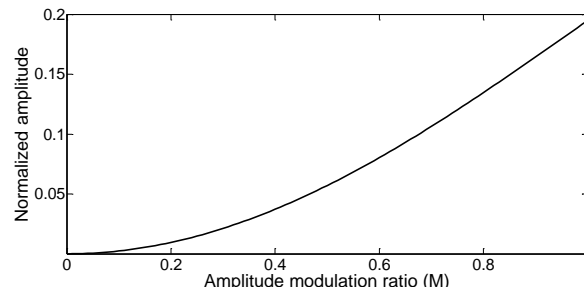


**Figure 5-32: Normalized amplitude of  $m_f-1$ -th harmonic for different values of M**

As Figure 5-32 reveals, the amplitude of the lowest-frequency harmonic is increased by increasing the amplitude modulation ratio. As a result, for estimating the worst case,  $M_{GSC} = 1$  and  $M_{RSC} = 1$  can be considered.

### 5.6.2 Example

In this sub-section, an example is provided to illustrate the procedure for determining the major harmonic components in the worst-case scenario.

In this example, it is known that 6 DFIGs (1.5 MW each, PF=.9) are connected to a collector bus. The desirables are the major harmonic current components injected into the grid by GSC in the worst-case scenario. The estimation procedure consists of the following steps:

0. The following parameters should be known:
  - a. The converter's switching frequencies (in this example,  $f_{sw}=2.7kHz$ )
  - b. The DC link voltage (in this example  $V_{dc}=1150V$ )
  - c. The ratio of the stator and rotor rated voltages (or stator-to-rotor turn ratio)
  - d. The machine's total rotor and stator resistances and reactances (in this example  $R_s + R'_r = (.023 + 0.016)$  p.u. and  $X_s + X'_r = (.18 + .16)$  p.u.)
  - e. The choke's reactance and resistance (in this example,  $R_C = .003$  p.u. and  $X_C = .3$  p.u. Note that normally,  $R_C \ll X_C$ , so  $R_C$  may be neglected.)
  - f. Filter's resistance and capacitor (in this example  $R_f = .0551 \Omega$  and  $C_f = 936\mu F$ )
1. Calculate the impedances in the equivalent circuit of Figure 5-33 from the known parameters listed in the previous step:

$$S_{base} = \frac{6 \cdot 1.5}{PF} = 10MVA \text{ (for 6 parallel DFIGs)}$$

$$Z_{base} = \frac{V_{base}^2}{S_{base} \text{ (total turbines)}} = \frac{575^2}{10^6} = .0331 \text{ Ohm}$$

$$R_s + R'_r = (.023 + 0.016) * Z_{base} = 1.29e - 3 \text{ Ohm}$$

$$X_s + X'_r = (.18 + .16) * Z_{base} = .0113 \text{ Ohm}$$

$$R_C = .003 * Z_{base} = 9.92e - 5 \text{ Ohm}$$

$$X_C = .3 * Z_{base} = 9.92e - 3 \text{ Ohm}$$

$$R_f = .0551/6 = 9.2e - 3 \text{ Ohm (equivalent for 6 parallel filters)}$$

$$C_f = 936\mu F * 6 = 5.616e - 3 F \text{ (equivalent for 6 parallel filters)}$$

2. Determine the harmonic order and amplitudes for harmonic voltage source of Figure 5-33:

- a. Determining frequency modulation ratio:  $m_f = \frac{f_{sw}}{60Hz} = 45$ ,
- b. Determining harmonic orders: these components are sidebands of  $m_f$  and  $2m_f$ , i.e.,  $h=m_f \pm 2$  ( $43^{rd}$  and  $47^{th}$ ), and  $h=2m_f \pm 1$  ( $89^{th}$  and  $91^{st}$ )
- c. Determining harmonic voltage amplitudes: in 5.2, it was shown that  $V_{lb,h} = k V_{dc}$  where  $k$  is the coefficient of double Fourier series and can be obtained from either equation 5.4 or by using Table 5-2, which is repeated below. In this example,  $V_{dc}=1150V$  is multiplied by .195 to obtain  $V_{lb,43}$  and  $V_{lb,47}$ . Therefore,  $V_{lb,43} = V_{lb,47} = .195*1150 = 224.25$  V. Similarly,  $V_{dc}$  is multiplied by .111 to obtain  $V_{lb,89}$  and  $V_{lb,91}$ . Therefore,  $V_{lb,89} = V_{lb,91} = .111*1150 = 127.65$  V.

**$V_h/V_{dc}$  in PWM technique with large odd  $m_f$  multiple of 3**

$h$	<b>M</b>				
	<b>.2</b>	<b>.4</b>	<b>.6</b>	<b>.8</b>	<b>1</b>
<b>1</b>	.122	.245	.367	.490	.612
<b><math>m_f \pm 2</math></b>	.010	.037	.080	.135	<b><u>.195</u></b>
<b><math>m_f \pm 4</math></b>	-	-	-	.005	.011
<b><math>2m_f \pm 1</math></b>	.116	.200	.227	.192	<b><u>.111</u></b>
<b><math>2m_f \pm 5</math></b>	-	-	-	.008	.020
<b><math>3m_f \pm 2</math></b>	.027	.085	.124	.108	.038

3. Calculate the harmonic currents: for each harmonic order  $h$ , the corresponding  $V_{lb,h}$  obtained in the previous step is considered in the equivalent circuit of Figure 5-33, and the current injected into the network ( $i_h$ ) is calculated. Table 5-8 shows the harmonic current spectrum of this example.

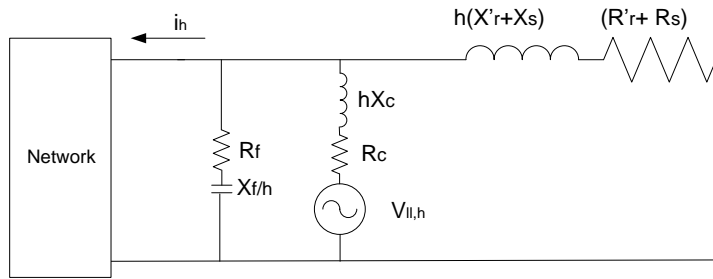


Figure 5-33: Equivalent circuit for calculation of harmonic currents caused by GSC

Table 5-8: Major harmonic components the example in the worst condition

Harmonic order (h)	Harmonic content (% of fundamental)
43	.147
47	.1762
89	.4906
91	.578

Note that to calculate the harmonic current caused by the RSC, the procedure is similar except for two slight differences: (a) in Step 2, the harmonic voltages should be multiplied by the ratio of the stator’s rated voltage to the rotor’s rated voltage or the stator-to-rotor turn ratio (in order to convert the harmonic voltage source from the rotor circuit to the stator circuit), and (b) instead of using equivalent circuit of Figure 5-33, the equivalent circuit shown in Figure 5-34 should be used.

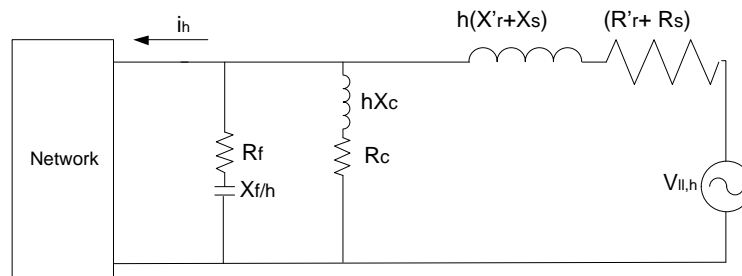


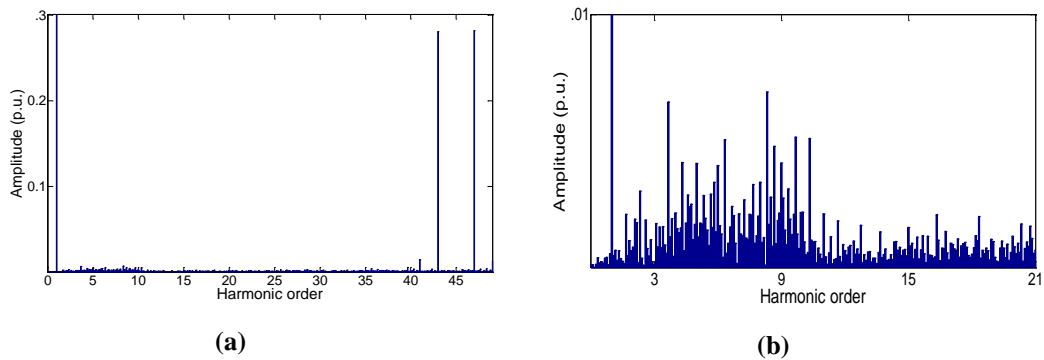
Figure 5-34: Equivalent circuit for calculation of harmonic currents caused by RSC

### 5.7 Non-characteristic harmonics

In the modelling, the DC link voltage was considered to be ripple-free and, consequently, only the harmonics due to the ideal PWM switching was considered

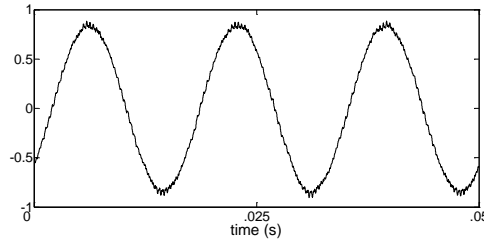
in the model. However, in 5.1 it was shown that low-order non-characteristic harmonics are also present in the converters' terminal voltages. This section will demonstrate the source of these components.

Figure 5-35 (a) shows the normalized harmonic contents of the GSC's terminal voltage. As this figure reveals, the main components are the sidebands of the switching frequency (the 43<sup>rd</sup> and 47<sup>th</sup> order harmonics). However, small but non-zero components exist at lower frequencies. Figure 5-35 (b) reveals that these components have magnitudes of less than 0.8% of the fundamental component's magnitude. These results were achieved when no background distortion was present in the distribution system. Consequently, they are caused by the converters and their control system.



**Figure 5-35: Normalized harmonic components of voltage at GSC terminals, (a) up to 48<sup>th</sup> harmonic, (b) up to 21<sup>st</sup> harmonic**

Figure 5-36 shows the reference signal generated by the GSC's controller, and Figure 5-37 shows its harmonic spectrum. As these figures reveal, the converter's controller fails to generate a purely sinusoidal reference signal, and this signal contains harmonics which are modulated with the carrier signal and appear in the converter's voltages. Nevertheless, as was mentioned above, the magnitude of these harmonics is very small, and the main aim of this section was to demonstrate only the origin of these components.



**Figure 5-36: PWM reference signal of GSC**

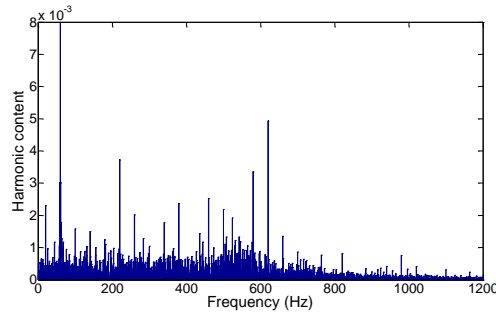


**Figure 5-37: Normalized spectrum of PWM reference signal of GSC**

## 5.8 Comparison with other harmonic sources and standards

It is advantageous to quantitatively compare the harmonic emissions of DFIG-based wind farms with those of more well-studied and well-characterized harmonic sources and also with the harmonic limits suggested by power quality standards. Such comparisons will provide a better understanding of the amount of harmonics emitted by DFIG-based wind farms.

In [80] the equivalent-CFL indexing method is proposed to compare harmonic emissions of home appliances. In this method, the current harmonics of CFLs are considered as a “relative harmonic injection benchmark” for comparing the harmonic injections of other home appliances [80]. Then, the equivalent CFL index is calculated for each appliance. The CFL index of each appliance expresses the harmonic emissions of that appliance as the number of CFLs its harmonic emissions are equivalent to. The procedure to obtain the equivalent CFL index is as following [80]:

1. For each harmonic order, the ratio of appliance’s current ( $I_{h,appliance}$ ) to the CFL’s current ( $I_{h,CFL}$ ) is calculated:

$$Ratio_{h,appliance} = \frac{I_{h,appliance}}{I_{h,CFL}} \tag{5-25}$$

2. The ratios are aggregated to one value as follows:

$$Equivalent\ CFL = \sqrt{\sum_{h=3}^H (w_h * Ratio_{h,appliance})^2} = \sqrt{\frac{\sum_{h=3}^H I_{h,appliance}^2}{\sum_{h=3}^H I_{h,CFL}^2}} \tag{5-26}$$

where the weighting factor  $w_h$  is the individual harmonic distortion of the CFL’s current [80].

Although the equivalent CFL indexing is an appropriate method for comparing the low frequency harmonic injection of relatively small appliances but not wind farms, the idea can be borrowed, and larger harmonic sources such as Plug-in Hybrid Electric Vehicle (PHEV) chargers, service transformers, and DC drives can be used as benchmarks instead of CFLs. In the following paragraphs, by using (5-26), the harmonic emissions of the simulated DFIG-based wind farm are quantitatively compared to above mentioned sources. Note that this method has been established for low-frequency harmonics and only the low-frequency harmonic components of the benchmarks’ spectra are available for comparison. Nevertheless, such comparison provides a useful insight into the level of the wind farm’s non-characteristic harmonics.

**Table 5-9: Normalized spectrum of harmonic sources**

Source	I <sub>h3</sub>	I <sub>h5</sub>	I <sub>h7</sub>	I <sub>h9</sub>	I <sub>h11</sub>	I <sub>h13</sub>	I <sub>h15</sub>	I <sub>h17</sub>	I <sub>h19</sub>	I <sub>h21</sub>	I <sub>h23</sub>	I <sub>h25</sub>	I <sub>h27</sub>	I <sub>h29</sub>
PHEV	0.0424	0.0012	0.0019	0.0012	0.0015	0.0024	0.0041	0.0021	0.0015	0.0005	0.0008	0.0018	0.0015	0.0011
ST*	0	0.1315	.057	0	0.019	0.0156	0	0.008	0.0039	0	0.0061	0.0031	0	0.0011
DCD**	0.023	0.017	0.008	0.005	0.0734	0.0421	0.003	0.007	0.0055	0.0031	0.0124	0.0132	0.003	0.0028

\* ST: Service transformer

\*\* DCD: DC drive

Table 5-9 shows the normalized spectra of a type-2 PHEV charger, a 37 kVA service transformer and a 12-pulse DC drive obtained from measurements. These values are used in (5-26) instead of the CFL’s harmonic currents. As a result,

three indices are obtained for the wind farm, which are .085 in comparison to the PHEV charger, 0.0254 in comparison to the service transformer and 0.04 in comparison to the DC drive. These values are all smaller than 1. Therefore, the wind farm is not a significant source of harmonic emissions in comparison to these three sources. For further illustration, consider a 9MW wind farm and a 3-kW type-2 PHEV charger. The wind farm’s power is 3000 times the charger’s power while its harmonic injection is equal to only  $3000 \times .085 = 255$  of the PHEV chargers’ injections. Similarly, the wind farm’s power is almost 243 times that of the service transformer (which normally feeds  $243 \times 10$  house/transformer=2430 houses) while its harmonic injection is equal to only  $243 \times .0254 = 6.17$  of the service transformers’ (62 houses’) injection.

In this part of the research, the harmonic emissions of wind farms were also compared with the harmonic limits specified in the major power quality standards, IEEE Std. 1547 and IEC 61000-3. In contrast to the equivalent CFL indexing, the comparison of the DFIG’s harmonic spectrum with the limits determined in these standards provides the opportunity to assess the high-frequency harmonic emissions of the wind farms. Table 5-10 shows the comparison between the current harmonic emissions from the simulated wind farm with the limits determined in IEEE Std. 1547. As this table reveals, the simulated wind farm complies with the limits in the standard.

**Table 5-10: Comparison of the farm’s harmonic currents with the limits of IEEE Std. 1547**

Source	$I_{h5}$ (%)	$I_{h7}$ (%)	$I_{h11}$ (%)	$I_{h13}$ (%)	$I_{h17}$ (%)	$I_{h19}$ (%)	$I_{h23}$ (%)	$I_{h25-33}$ (%)	$I_{h>33}$ (%)*
DFIG	.34	.04	.07	.02	.005	.004	.001	-	.258
IEEE Std. 1547	4	4	2	2	1.5	1.5	.6	.6	.3

\* According to Figure 5-26 for  $h > 33$ , the highest harmonic content of the simulated wind system is 0.258%

Table 5-11 shows the comparison between the voltage harmonics at the wind farm’s PCC with the limits specified by IEC 61000-3. As this table demonstrates, the wind farm’s operation complies with IEC 61000-3.

**Table 5-11: Comparison of the farm’s harmonic voltages with the limits of IEC 61000-3**

Source	V <sub>h5</sub> (%)	V <sub>h7</sub> (%)	V <sub>h11</sub> (%)	V <sub>h13</sub> (%)	V <sub>h17</sub> (%)	V <sub>h19</sub> (%)	V <sub>h23</sub> (%)	V <sub>h25</sub> (%)	V <sub>h43</sub> (%)	V <sub>h47</sub> <sup>*</sup> (%)
DFIG	.06	.02	.02	.15	.22	.04	.01	.06	.952	.813
IEC 61000-3	5	4	3.5	3	2	1.5	1.5	1.5	.96	.89

\* For  $h > 25$ , the IEC 61000-3 limit is calculated as  $0.2 + 1.3 * (25/h)$ . For the simulated system, harmonic components for  $h > 47$  also comply with IEC 61000-3.

## 5.9 Conclusion

In this chapter, the harmonic emissions of DFIG-based wind farms were analyzed, and a harmonic modelling method was proposed. The following points are the main conclusions of this chapter.

1. An accurate model was presented based on a double Fourier series of the sinusoidal PWM pulse train, and validated by using time-domain simulations. The model contains only voltage sources and impedances and can be used instead of a detailed power electronic model for harmonic analysis.
2. It was shown that DFIG-based wind systems generated both harmonics and inter-harmonics. The frequency of inter-harmonics depends on the rotor's speed, which is a function of wind speed.
3. In PWM switching, the harmonics appear in the odd sidebands of the converters' switching frequencies. The simulations and analysis showed that DFIGs converters generated large characteristic harmonic currents and voltages. However, the DFIG is equipped with a filter which prevents the propagation of harmonics in the network. As an example, in the simulated case, the normalized amplitude of the harmonic currents injected to the PCC is less than .3%, and the normalized amplitude of each harmonic voltage at PCC was less than 1%.
4. The detailed simulations showed that non-characteristic harmonics can appear in the DFIG's output, which are caused by converters' control systems. These non-characteristic harmonic components appear in the lower frequencies (lower than 1kHz).

5. The sensitivity analysis showed that these non-characteristic harmonics were changed arbitrarily by the change in the power system's background harmonic spectrum. Especially, referring to Figure 5-8, the low-order integer-harmonics which are the most important components in harmonic studies, show almost no sensitivity to the background harmonics.
6. Finally, the characteristic and non-characteristic harmonic components of a DFIG system have very low magnitudes. As a result, these components can barely be considered as harmonic sources in the power system. This finding was confirmed by the quantitative comparison of the harmonic emissions of the DFIG-based wind farms with those of other harmonic sources.

# Chapter 6

## Conclusions and Future Work

In this chapter, the main findings of the thesis are summarized, and suggestions for future work are presented.

### 6.1 Thesis conclusions and contributions

This thesis investigated the impact of DGs on the O.C. protection system's coordination and also on DG's harmonic emissions. The conclusions and contributions are as following:

- The potential impact of DGs on the O.C. protection were illustrated. This impact causes miscoordination between the main and back-up protection devices, failure in the fuse-saving scheme, false tripping, and desensitization of the protection. As well, the magnitude of the fault current contributed by a DG and the time widow during which the DG's fault current contribution is significant were identified as two key factors which should be considered during an investigation of the impact of each DG type on the coordination.
- DGs were categorized into four types based on their electrical interface with the power system. The early stages of the research showed that Induction-Machine DGs (IMDG) and Permanent Magnet Synchronous Generators (PMSGs) had a negligible impact on the O.C. coordination. The findings on these two types are available in the appendices. Consequently, the main focus was on the IBDGs and SMDGs and finding methods to mitigate their impact on the O.C. coordination.
- Regarding IBDGs, it was shown that IBDGs with DG trip protection cannot impact on the coordination. In contrast, IBDGs with current-limiting

protection may impact on the marginal coordinations, especially at relatively high penetration levels. In order to mitigate this impact, a strategy was proposed in which the inverter's current limit is not fixed but adjusted dynamically based on the PCC voltage. The simulation results showed that, by using the proposed control strategy, the inverter's current was limited significantly when a fault happened near the PCC. As a result, the simulated IBDG had no contribution to the fault and could not impact on the coordination. In addition, by this strategy when non-fault disturbances or distant faults occurred (where DG has no impact), IBDG operated normally. In summary, this strategy can be implemented easily and can mitigate the probable impact of IBDGs on coordination successfully without causing any abnormal operation during the power system's normal operation or non-fault disturbances.

- It was shown that among all types of DGs, SMDGs had the highest and the longest contribution to the fault current. The machine's response was divided into three periods, and it was shown that during the transient period, machine's fault current was 3~5 p.u. which gradually decayed with a transient time constant in the range of 1-2 sec. This period coincided with the operation of major O.C. devices in distribution system, and this part of machine's response seriously impacted on the coordination. Next, in order to restrict the machine's fault current contribution in this period and, consequently, to mitigate the impact of the machine on the O.C. protection coordination, a field discharge application was proposed. The mathematical analysis and simulation result showed that this circuit removed the steady state part of machine's current by disconnecting its excitation and decreased the machine's transient time constant by increasing field circuit's resistance. As a result, the machine's fault current decayed faster. In addition, it was shown that applying the field discharge circuit could sufficiently reduce the generator's contribution to the fault current so that this circuit prevented miscoordination when short time-delay and/or inverse-time O.C. relays were involved.

- In the investigation of DG's impact on the harmonic emissions, the main focus was on the DFIG-based wind farms. The harmonic contents of DFIG-based wind farms were analyzed and it was shown that DFIG-based wind systems generated both integer and inter-harmonics. Moreover, an accurate model was presented based on a double Fourier series of sinusoidal PWM pulse train. The main advantage of this model is that it contains only voltage sources and impedances, and there is no need for detailed modelling of the power electronics for harmonic analysis. Furthermore, simulations and analysis showed that DFIGs converters can generate large characteristic harmonic currents and voltages. However, the DFIG's filter prevented the propagation of harmonics in the network. In addition to characteristic harmonics, simulations showed that non-characteristic harmonics can appear in the DFIG's outputs which were caused by converters' control systems. These non-characteristic harmonic components appeared in the lower frequencies (lower than 1kHz) and could not be calculated in the presented model. Nevertheless, the amplitudes of these harmonic were low enough to be neglected.

### **6.2 Suggestions for future work**

The suggestions for extending and modifying this research are as follows:

- The current restricting strategy proposed in Chapter 3 for IBDGs could be implemented on an experimental set-up and its effectiveness could be explored through laboratory tests.
- The field discharge circuit proposed in Chapter 4 for SMDGs could be designed for and applied to an experimental set-up. Laboratory tests could be conducted to show the effectiveness of this method in restricting the SMDG's current's contribution to the fault, and this method's effect on the stator's current components, field current and voltage could be compared to the effects achieved in the simulation.

## Chapter 6: Conclusions and Future Work

- For the modified field discharge circuit proposed in Section 4.8 of Chapter 4, a strategy could be established to determine  $R_0$ ,  $T_1$  (the period in which  $R_0$  is in the circuit) and the ratings of the bypass switch  $S_0$ , based on the LVRT requirements imposed by grid codes.
- As was mentioned in Chapter 4, AVR is another tool for controlling the machine's field and, consequently, for controlling the machine's output current. The AVR's ability to reduce the machine's output current during the fault could be examined and compared with the ability of the field discharge circuit.
- Conducting field measurements and harmonic analysis of the data for harmonic emissions of DFIG-based wind farms could support the analysis provided in Chapter 5. Besides, field measurements could provide a more realistic insight into the non-characteristic harmonic components and their levels in these farms. Furthermore, such data could be used to develop stochastic harmonic models, which are more suitable for estimating non-characteristic harmonics.

# Chapter 7

## References

- [1] A. piccolo and P. Siano, “Evaluating the Impact of Network Investment Deferral on Distributed Generation Expansion”, IEEE Trans. on Power Systems, pp 1559-1567 vol. 24, No. 3, August 2009.
- [2] J. M. Guerrero, F. Blaabjerg, T. Zhelev, K. Hemmes, E. Manmasson, S. Jemei, M. P. Comech, R. Granadino, J. I. Frau, “ Distributed Generation: Toward a New Energy Paradigm”, IEEE Industrial Electronics Magazine, pp 52-64, vol. 4, issue 1, March 2010.
- [3] M. Triggianese, F. Liccardo and P. Marino, “Ancillary Services Performed by Distributed Generation in Grid Integration” Clean Electrical Power, 2007. Proceedings. International Conference. 2007, pp.164 – 170.
- [4] IEEE 1547 – 2003, IEEE Standard for Interconnecting Distributed Resources with Electric Power System, 2003.
- [5] Standard For The Interconnection Of Generators To ATCO Electric’s Distribution System, [Online] Available: [http://www.atcoelectric.com/Services/Business-to-Business/Power-  
Producers/Documents/generator\\_interconnect\\_guide.pdf](http://www.atcoelectric.com/Services/Business-to-Business/Power-Producers/Documents/generator_interconnect_guide.pdf)
- [6] Technical Requirements For Connecting Distributed Resources To The Manitoba Hydro Distribution System, [Online] Available: [http://www.hydro.mb.ca/customer\\_services/customer\\_owned\\_generation/co  
nnecting\\_distributed\\_resources.pdf](http://www.hydro.mb.ca/customer_services/customer_owned_generation/connecting_distributed_resources.pdf)
- [7] Guide For Generator Interconnection To The Wires Owner Distribution System, ENMAX Power Corporation, [Online] Available: [http://www.enmax.com/NR/rdonlyres/2CB5C535-F6DF-44F8-8E40-  
229D1D7178B1/0/Attachment\\_A\\_ENMAX\\_Distributed\\_Generator\\_Interco  
nnection\\_Guide.pdf](http://www.enmax.com/NR/rdonlyres/2CB5C535-F6DF-44F8-8E40-229D1D7178B1/0/Attachment_A_ENMAX_Distributed_Generator_Interco<br/>nnection_Guide.pdf)

## Chapter 7: References

- [8] C. Rahmann, H. J. Haubrich, A. Moser, R. Palma-Behnke, L. Vargas and M. B. C. Salles, “Justified Fault-Ride Through Requirements for Wind Turbines in Power Systems”, IEEE Trans. Power Systems, vol. 26, no.3, pp. 1555–1563, Aug. 2011.
- [9] E.ON Netz grid code—High and extra high voltage., E.ON Netz GmbH, Bayreuth, Germany. [Online]. Available: <http://www.eon-netz.com/Ressources/downloads/enenarhseng1.pdf>
- [10] Wind Turbines Connected to Grids With Voltages Above 100 kV—Technical Regulation for the Properties and the Regulation of Wind Turbines, Elkraft System and Eltra Regulation, 2004, Draft version TF 3.2.5.
- [11] E.Troester “New German Grid Codes for Connecting PV Systems to the Medium Voltage Power Grid”, in 2nd International Workshop on Concentrating Photovoltaic Power Plant, 2009.
- [12] Technical Guideline - Generating Plants Connected to the Medium-Voltage Network, Bundesverband der Energie- und Wasserwirtschaft e.V.(BDEW), Berlin, June 2008.
- [13] NERC Task Force on Integration of Variable Generation - Task 1.7: Low Voltage Ride-Through Requirements [Online] Available: [http://www.nerc.com/docs/pc/ivgtf/Task%2017%20work%20plan%20final%20\(2\).pdf](http://www.nerc.com/docs/pc/ivgtf/Task%2017%20work%20plan%20final%20(2).pdf)
- [14] J. Keller and B. Kroposki, “Understanding Fault Characteristics of Inverter-Based Distributed Energy Resources” A report to National Renewable Energy Resources (NREL), Jan. 2010.
- [15] I. El-Samahy and E. El-Saadany, “The Effect of DG on Power Quality in a Deregulated Environment”, in Proc. IEEE Power Engineering Society General Meeting, 2005, pp 2969-2975.
- [16] J. A. Martinez and J. Martin-Arnedo, “Impact of Distributed Generation on Distribution Protection and Power Quality”, in Proc. IEEE Power & Energy Society General Meeting (PES '09), 2009, pp 1-6.
- [17] B. Hussain, S. M. Sharkh and S. Hussain, “Impact Studies of Distributed Generation on Power Quality and Protection Setup of an Existing

## Chapter 7: References

- Distribution Network”, in Proc. International Symposium on Power Electronics Electrical Drives Automation and Motion (SPEEDAM), 2010, pp 1243-1246.
- [18] Fei Wang, J. L. Duarte, M. A. M. Hendrix and P. F. Ribeiro, “Modeling and Analysis of Grid Harmonic Distortion Impact of Aggregated DG Inverters”, IEEE Trans. Power Electronics, vol. 26, No. 3, pp 786-797, Mar. 2011.
- [19] X. Zhou, J. Linag, W. Zhou and X. Jin, “Harmonic Impact of Inverter-based Distributed Generations in Low Voltage Distribution Network”, in Proc. 3rd International Symposium on Power Electronics for Distributed Generation Systems (PEDG), 2012, pp 615-620.
- [20] A. F. Abdul Kadir, A. Mohamed and H. Shareef, “Harmonic Impact of Different Distributed Generation Units on Low Voltage Distribution System,” in Proc. IEEE International Electric Machines & Drives Conference (IEMDC), 2011, pp. 1201-1206.
- [21] IEEE Recommended Practice for Protection and Coordination of Industrial and Commercial Power Systems, IEEE Std. 242-2001.
- [22] P. P. Barker and R. W. De Mello, “Determining the Impact of Distributed Generation on Power System: Part 1- Radial Distribution Systems,” in IEEE Power Engineering Society Summer Meeting, 2000, vol. 3, pp. 1645-1656.
- [23] “Impact of Distributed Resources on Distribution Relay Protection,” A report to the Line Protection Subcommittee of the Power System Relay Committee of the IEEE Power Engineering Society, prepared by working group D3, 2004.
- [24] S. Chaitusaney and A. Yokoyama, “An Appropriate Distributed Generation Sizing Considering Recloser-Fuse Coordination,” in Proc. IEEE/PES Transmission and Distribution Conference and Exhibition: Asia and Pacific, 2005, pp 1-6.
- [25] H. Cheung, A. Hamlyn, L. Wang, C. Yang and R. Cheung, “Investigations of Impact of Distributed Generation on Feeder Protection,” in IEEE Power and Energy Society General Meeting, 2009, pp. 1-7.

## Chapter 7: References

- [26] S. Chaitusaney and A. Yokoyama, “Impact of Protection Coordination on Sizes of Several Distributed Generation Sources,” in Proc. 7th Int. Conf. Power Engineering Conference 2005, vol. 2 pp.669 – 674.
- [27] M. Baran and I. El-Markabi, “Fault Analysis on Distribution Feeders with Distributed Generators,” IEEE Trans. Power System, vol. 20, no. 4, pp 1757-1764, November 2005.
- [28] T. K. Abdel-Galil, A. E. B. Abu-Elnien, E. F. El-saadany, A. Girgis, Y. A.-R. I. Mohamed, M. M. A. Salma, and H. H. M. Zeineldin “Protection Coordination Planning with Distributed Generation,” report to Natural Resources Canada-Energy Technology and Program Sector, June 2007.
- [29] D. Turcotte and F. Katiraei, “Fault Contribution of Grid-Connected Inverters,” in Electrical Power and Energy Conference (EPEC), 2009, pp. 1-5.
- [30] Y. Pan, W. Ren, S. Ray, R. Walling and M. Reichard, “Impact of Inverter Interfaced Distributed Generation on Overcurrent Protection in Distribution Systems,” in Proc. IEEE Power Engineering and Automation Conference (PEAM), 2011, pp 371-376.
- [31] C. A. Plet, M. Graovac, T. C. Green, and R. Iravani, “Fault response of Grid-connected Inverter Dominated Networks,” in Power and Energy Society General Meeting. IEEE, 2010, pp. 1–8.
- [32] X. Yu and Z. Jiang, “Dynamic Current Limiting Control of Voltage Source Inverters,” in Proc. IEEE Int. Electric Machines and Drives Conference, 2009, pp 1664-1668.
- [33] R. J. Bravo, R. Yinger, S. Robles and W. Tamae, “Solar PV Inverter Testing for Model Validation,” in IEEE Power and Energy Society General Meeting, 2011, pp. 1-7.
- [34] S. Chaitusaney, and A. Yokoyama, “Prevention of Reliability Degradation from Recloser–Fuse Miscoordination Due To Distributed Generatio,” IEEE Trans. Power Delivery, vol. 23, no.4, pp. 2545–2554, Oct. 2008.
- [35] P. M. Anderson, Power System Protection. New York: IEEE Press, 1999, pp. 220-222.

## Chapter 7: References

- [36] J. He, Y. W. Li, and S. Munir, "A Flexible Harmonic Control Approach through Voltage Controlled DG-Grid Interfacing Converters," *IEEE Trans. Industrial Electronics*, vol. 59, no.1, pp. 444–455, Jan. 2012.
- [37] J. He, S. Munir, and Y. W. Li, "Opportunities for power quality improvement through DG-grid interfacing converters," *International Power Electronics Conference (IPEC'10)*, in *Proc. IEEE ECCE-Asia*, 2010, pp. 1657-1664.
- [38] H. Li, F. Li, Y. Xu, D. T. Rizy and J. D. Kueck, "Adaptive Voltage Control With Distributed Energy Resources: Algorithm, Theoretical Analysis, Simulation, and Field Test Verification", *IEEE Trans. Power System*, vol. 25, no.3, pp. 1638–1647, Aug. 2010.
- [39] C. A. Plet, M. Graovac, T. C. Green, and R. Iravani, "Fault response of Grid-connected Inverter Dominated Networks", in *Power and Energy Society General Meeting. IEEE*, 2010, pp. 1–8.
- [40] W. H. Kersting, "Radial distribution test feeders," in *Proc. IEEE Power Engineering Society Winter Meeting*. 2001, pp. 908–912.
- [41] AREVA T&D Automation, "Network Protection and Automation Guide", 1st edition, July 2002.
- [42] W. El-Khattam, and T. S. Sidhu, "Restoration of Directional Overcurrent Relay Coordination in Distributed Generation Systems Utilizing Fault Current Limite," *IEEE Trans. Power Delivery*, vol. 23, no.2, pp. 576–585, Apr. 2008.
- [43] J. C. Gómez, and M. M. Morcos, "Coordination of Voltage Sag and Overcurrent Protection in DG System," *IEEE Trans. Power Delivery*, vol. 20, no.1, pp. 214–218, Jan. 2005.
- [44] W. El-Khattam, and T. S. Sidhu, "Resolving the impact of distributed renewable generation on directional overcurrent relay coordination: a case study," *IET Renew. Power Gener.*, vol. 3, no.4, pp. 415–425, 2009.
- [45] C. J. Mozina, "A Tutorial on the Impact of Distributed Generation (DG) on Distribution Systems", in *Proc. Protective Relay Engineers Annual Conference*, 2008, pp.591 – 609.

## Chapter 7: References

- [46] R. A. Walling, R. Saint, R. C. Dugan, J. Burke, and L. A. Kojovic, "Summary of Distributed Resources Impact on Power Delivery System," *IEEE Trans. Power Delivery*, vol. 23, no.3, pp. 1636–1644, Jul. 2008.
- [47] S. Chaitusaney, and A. Yokoyama, "Prevention of Reliability Degradation from Recloser–Fuse Miscoordination Due To Distributed Generatio," *IEEE Trans. Power Delivery*, vol. 23, no.4, pp. 2545–2554, Oct. 2008.
- [48] J. Chen, R. Fan, X. Duan and J. Cao, "Penetration Level Optimization for DG Considering Reliable Action of Relay Protection Device Constrains", in *Proc. Int. Conf. on Sustainable Power Generation and Supply*, 2009, pp.1-5.
- [49] T. K. Abdel-Galil, A. E. B. Abu-Elnien, E. F. El-saadany, A. Girgis, Y. A.-R. I. Mohamed, M. M. A. Salma, and H. H. M. Zeineldin , "Protection Coordination Planning with Distributed Generation" *CANMET ENERGY TECHNOLOGY CENTRE, Varennes, QC, CETC-Varennes 2007-149 (TR)*, 2007.
- [50] H. B. Funmilayo and K. L. Buylar-Purry, "An Approach to Mitigate the Impact of Distributed Generation on the Overcurrent Protection Scheme for Radial Feeders", in *Proc. IEEE Power System Conference and Exposition*, 2009, pp. 1-11.
- [51] F. A. Viawan, D. Karlsson, A. Sannino and J. Daalde, "Protection Scheme for Meshed Distribution Systems with High Penetration of Distributed Generation", in *Proc. Pow. Sys. Conf. on Advanced Metering, Protection Control, Communication, and Distribution Resources*, 2006, pp 99-104.
- [52] I. M. Chilvers, N. Jenkins and P. A. Crossley, "The Use of 11kV Distance Protection to Increase Generation Connected to the Distribution Network", in *Proc. Int. Conf. on Development in Power System Protection*, 2004, vol. 2, pp 551-554.
- [53] D. Uthitsunthorn and T. Kulworawanichpong, "Distance Protection of a Renewable Energy Plant in Electric Power Distribution Systems", in *Proc. Int. Conf. on Power System Technology 2010*, pp. 1-4.
- [54] H. Wan, K. K. Li and K. P. Wong, "An Adaptive Multiagent Approach to Protection Relay Coordination With Distributed Generators in Industrial

## Chapter 7: References

- Power Distribution System”, IEEE Trans. Industry Applications, vol. 46, No. 5, pp 2118-2124, Sept./Oct. 2010.
- [55] J. Ma, J. Li and Z. Wang, “An Adaptive Distance Protection Scheme for Distribution System with Distributed Generation”, in Proc. 5th Int. Conf. on Critical Infrastructures, 2010, pp 1-4.
- [56] M. Baren and I. El-Markabi, “Adaptive Overcurrent Protection for Distribution Feeders with Distributed Generators”, in Proc. Power System Conference and Exposition, 2004, vol. 2, pp 715-719.
- [57] W. El-Khattam and T. S. Sidhu, “Restoration of Directional Overcurrent Relay Coordination in Distributed Generation Systems Utilizing Fault Current Limiter”, IEEE Trans. Power Delivery, vol. 23, No. 2, pp 576-585, Apr. 2008.
- [58] H. Yamaguchi and T. Kataoka, “Current Limiting Characteristics of Transformer Type Superconducting Fault Current Limiter With Shunt Impedance and Inductive Load”, IEEE Trans. Power Delivery, vol. 23, No. 4, pp 2545-2554, Oct. 2008.
- [59] Y. Zhang and R. A. Dougal, “Novel Dual-FCL Connection for Adding Distributed Generation to a Power Distribution Utility”, IEEE Trans. Applied Superconductivity, vol. 21, No. 3, pp 2179-2183, Jun. 2011.
- [60] B. Adkins and R. C. Harley, The General Theory of Alternating Current Machines. London: Chapman and Hall, 1975.
- [61] R. C. Dorf, The Electrical Engineering Handbook, CRC Press, 1997.
- [62] C. A. Gross, Electric Machines. CRC Press, 2007.
- [63] J. Taborda, “Modern Technical Aspect of Field discharge Equipment for Excitation Systems,” in Proc. IEEE Power and Energy Society General Meeting, 2008, pp. 1-8.
- [64] IEEE 1110-1991, IEEE Guide for Synchronous Generator Modeling Practices in Stability Analyses, 1991.
- [65] A. M. El-Serafi, S. O. Faried, “Effect of Field Discharge Resistors on Turbine\_Generator Shaft Torsional Torques,” IEEE Trans. on Energy Conversion, vol. 5, no. 1, pp. 129-136, March 1990.

## Chapter 7: References

- [66] R. Mutukutti, D. Apps, C. Henville, “Field Breaker Tripping Options For Generator Static Excitation Systems with AC Field Circuit Breakers – A Case Study,” in Proc. IEEE Power and Energy Society General Meeting, 2010, pp. 1-6.
- [67] J. R. Hill, A. Hunt, W. J. Joyce, D. H. Tompsett, “Field Suppression of Turbo Alternators,” Proceedings of the IEE – Part A: Power Engineering, vol: 107, Issue: 32, 1960.
- [68] A. Sallaem, O. Malik, Protection of Electric Distribution Systems, Wiley-IEEE, 2011, pp. 163-235.
- [69] ANSI / IEEE C37.18.1979, Standard Enclosed Field discharge Circuit Breakers for Rotating Electric Machinery.
- [70] “Static Excitation Equipments for Gas Turbines,” [online] available at <http://www.lici.com.cn/ASP/download/images/263.pdf>
- [71] G. W. Chang and S. K. Chen, “An Analytical Approach for Characterizing Harmonic and Interharmonic Currents Generated by VSI-Fed Adjustable Speed Drives,” IEEE Trans. Power Delivery, vol. 20, no. 4, pp. 2585–2593, Oct. 2005.
- [72] J. Shen, J. A. Taufiq and A. D. Mansell, “Analytical Solution to Harmonic Characteristics of Traction PWM Converters,” IEE Proc. Electric Power Applications, vol. 144, Issue. 2, pp 158-168, 1997.
- [73] X. Lu, C. Rogers and F. Z. Peng, “A Double Fourier Analysis Development of THD for PWM Inverters: A Theoretical Method for Motor Loss Minimization,” IEEE Energy Conversion Congress and Exposition (ECCE) 2010, pp 1505-1510, 2010.
- [74] J. Hamman and F. S. Van Der Merwe, “Voltage Harmonics Generated by Voltage-Fed Inverters Using PWM Natural Sampling,” IEEE Trans. Power Electronics, vol. 3, no. 3, pp. 297–302, Jul. 1988.
- [75] KUO-HSIUNG TSENG , WEN-SHIOW KAO , YUNG-FU CHENG & SHIN-FU LIN (2004): Analytical Solution to Harmonic Characteristics of Three-Phase PWM Inverter Using 3-D Modulation Model, Electric Power Components and Systems, 32:11, 1105-1120

## Chapter 7: References

- [76] N. Mohan, T. Undeland, and W. Robbins, *Power Electronics: Converters, Applications and Design*, 2nd ed. New York: Wiley, 1995, pp. 226–228.
- [77] M. Stiebler, *Wind Energy Systems for Electric Power Generation*, Springer, 2008, p. 138.
- [78] S. Muller, M. Deicke and Rik W. De Doncker, “ Doubly Fed Induction Generator Systems for Wind Turbines”, *IEEE Industry Application Magazine*, pp 26-33, vol. 8, issue 3, May/June 2002.
- [79] G. Abad, J. Lopez, M. Rodriguez, L. Marroyo and G. Iwanski, *Dobly Fed Induction Machine: Modelling and Control for Wind Energy Generation*,” Wiley, 2011.
- [80] A. Nassif, “Modelling, Measurement and Mitigation of Power System Harmonics,” PhD Dissertation, Dept. Elect. Comp. Eng., Univ. of Alberta, Edmonton, Canada, Fall 2009.
- [81] IEEE Task Force on Harmonic Modelling and Simulation, “Test Systems for Harmonic Modelling and Simulation,” *IEEE Trans. Power Delivery*, vol. 14, no. 2, pp. 579–587, Jul. 1999.

## **Appendix A:**

# **Fault Current Contribution of Induction-Machine DGs**

In this section, the contribution of different types of IMDGs to the fault current is studied, and their impact on the O.C. protection are investigated. Note that Induction Generators (IGs) are mostly used in extraction of wind power. They are also used in the small hydro plants.

In the next sub-section, two types of IGs are introduced, and their output currents during the symmetrical and asymmetrical faults at the generator's terminals are studied by the analytical methods as well as the simulations. In the third sub-section, findings from an experimental research work are presented to confirm the analysis in previous parts. Next, the contribution of IMDGs to the fault current in the distribution system and their impact on the O.C. protection coordination are investigated. Finally, the last sub-section presents the conclusion.

### **A.1 Induction generator's fault current**

Based on their stator and rotor connection to the grid, the IGs can be categorized into three different types. In the first type, the stator is directly connected to the grid, while the rotor is isolated from the grid. In this type, the rotor could be either squirrel cage or wound in which phase windings are connected together through an adjustable external resistance. This type is named Singly-Fed IG (SFIG). In the second type, stator is connected directly to the grid, while the rotor windings are connected to the grid through power electronics converters. In references, this type is named Doubly-Fed IG (DFIG). Finally, in the third type, only the stator is connected to the grid through power electronics converter. In the following paragraphs, the contribution of the first two types to

the fault current is studied. IGs of the third type can be considered as IBDGs which have been covered in the previous section.

### A.1.1 Singly-Fed Induction Generator (SFIG)

IGs in this category have been used in the wind turbines and small hydro plants [1], [2]. In this type of IG, the following set of equations show the relations between machine's voltages, currents and fluxes [3]. Note that  $R_r$  in the wound rotors is the summation of the rotor winding's resistance and the external resistance.

$$v_s = R_s i_s + \frac{d\psi_s}{dt} + j\omega_s \psi_s \quad (\text{A-1})$$

$$v_r = R_r i_r + \frac{d\psi_r}{dt} + j(\omega_s - \omega_r)\psi_r \quad (\text{A-2})$$

$$\psi_s = L_s i_s + L_m i_r \quad (\text{A-3})$$

$$\psi_r = L_m i_s + L_r i_r \quad (\text{A-4})$$

From these equations, currents can be written as functions of fluxes [3]

$$i_s = \frac{1}{L_s - \frac{L_m^2}{L_r}} \psi_s - \frac{L_m}{L_r} \frac{1}{L_s - \frac{L_m^2}{L_r}} \psi_r \quad (\text{A-5})$$

$$i_r = -\frac{L_m}{L_r} \frac{1}{L_s - \frac{L_m^2}{L_r}} \psi_s + \frac{d\psi_r}{dt} + \frac{1}{L_s - \frac{L_m^2}{L_r}} \psi_r \quad (\text{A-6})$$

In addition, rotor and stator total inductances can be written in terms of leakage and mutual inductances as below

$$L_s = L_{s\sigma} + L_m \quad (\text{A-7})$$

$$L_r = L_{r\sigma} + L_m \quad (\text{A-8})$$

Then, stator and rotor currents can be re-written as following [3]

$$i_s = \frac{\psi_s}{L'_s} - k_r \frac{\psi_r}{L'_s} \quad (\text{A-9})$$

$$i_r = k_s \frac{\psi_s}{L'_r} + \frac{\psi_r}{L'_r} \quad (\text{A-10})$$

where  $L'_s$  and  $L'_r$  are stator and rotor transient inductances, respectively, and calculated as following [3]

## Appendix A: Fault Current Contribution of Induction-Machine DGs

$$L_s' = L_{s\sigma} + \frac{L_{r\sigma} L_m}{L_{r\sigma} + L_m} \quad (\text{A- 11})$$

$$L_r' = L_{r\sigma} + \frac{L_{s\sigma} L_m}{L_{s\sigma} + L_m} \quad (\text{A- 12})$$

phase fault at terminals, current at phase a can be obtained as following-During 3 [3]

$$i_a = \frac{\sqrt{2}V_s}{\omega_s L_s'} [e^{-\frac{t}{T_s'}} \cos \alpha - (1-\sigma) e^{-\frac{t}{T_r'}} \cos(\omega_s t + \alpha)] \quad (\text{A- 13})$$

where

$$T_s' = \frac{L_s'}{R_s} \quad (\text{A- 14})$$

$$T_r' = \frac{L_r'}{R_r} \quad (\text{A- 15})$$

$$\sigma = 1 - \frac{L_m^2}{L_s L_r} \quad (\text{A- 16})$$

Currents at phase *b* and *c* can also be obtained by replacing  $\alpha$  with  $(\alpha-2\pi/3)$  and  $(\alpha-4\pi/3)$  in (A- 13), respectively. From (A- 13), ac component of the IG's current during a 3-phase fault can be calculated as below [3]

$$i_{a,ac} = \frac{\sqrt{2}V_s}{\omega_s L_s'} (1-\sigma) e^{-\frac{t}{T_r'}} \cos(\omega_s t + \alpha) \quad (\text{A- 17})$$

As (A- 17) reveals, the ac component of IG's current is damped with the transient time constant  $T_r'$ . Figure A- 1 and Figure A-2 show the ac component of an IG's current and its RMS, respectively, for a typical generator with its parameters obtained from [2] and tabulated in Table A-1. As Figure A- 1 and Figure A-2 show, the ac component of the stator's current is higher than 1p.u. within the three cycles after the beginning of fault (up to 6 p.u. in the first cycle). Then the current reduces to zero. It is due to the fact that the SFIG has no magnetizing source when its terminals are shorted (symmetrical faults). So, when the initial energy stored in the machine's field is discharged, it cannot generate any current, and it has no contribution to the fault.

**Table A-1: Parameters of the simulated SFIG [2]**

Parameter	Value (p.u.)
$L_{s\sigma}$	.1
$L_{r\sigma}$	.098
$L_m$	3.5
$R_s$	.01
$R_r$	.014

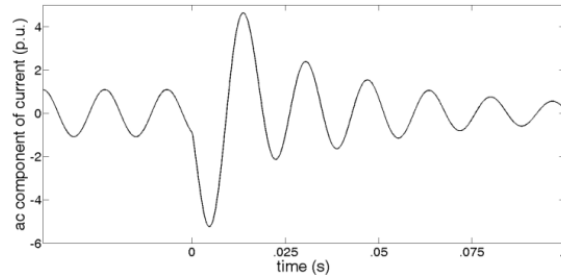


**Figure A- 1: ac component of SFIG's current during 3-phase fault at its terminals**

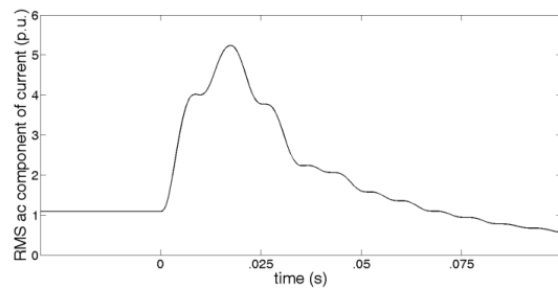


**Figure A-2: RMS ac component of SFIG's current during 3-phase fault at its terminals**

For IGs with wound rotor, when the rotor's external resistance is increased, the rotor's time constant is decreased. So, the short circuit current damps sooner. Also, machine has smaller fault current. Figure A-3 shows the simulated ac component of SFIG's stator's 3-phase fault current for different values of external resistance, and Figure A-4 shows its RMS value.

## Appendix A: Fault Current Contribution of Induction-Machine DGs

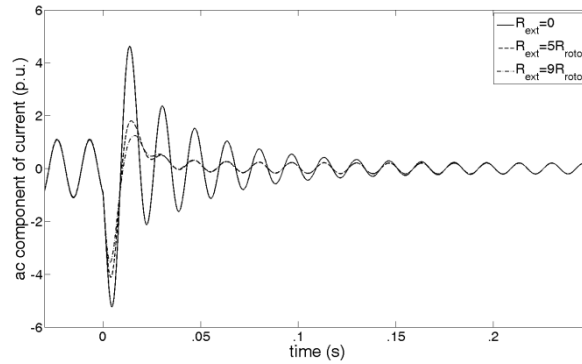


**Figure A-3: The impact of rotor's external resistance on the ac component of SFIG's current during 3-phase fault at its terminals**

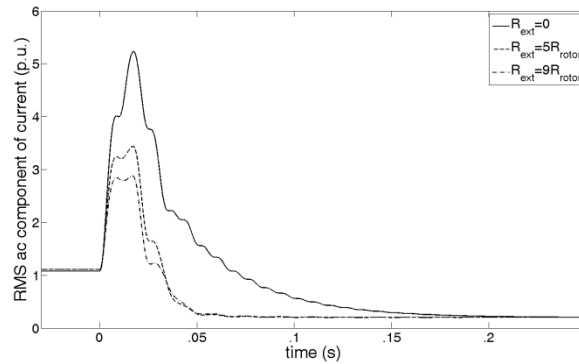


**Figure A-4: The impact of rotor's external resistance on the RMS ac component of SFIG's current during 3-phase fault at its terminals**

In order to achieve a general conclusion about the contribution of SFIGs to the 3-phase fault currents, the electrical circuit parameters of seven commercial IGs have been collected from [4], and their fault currents at the third and fifth cycle after the beginning of the fault have been calculated from (A- 17). Table A-2 summarizes these results. As this table reveals, the contribution of almost all of them in the third cycle after fault is around 2 p.u. which decreases to 1.3 p.u. or less (in most cases), in the fifth cycle after the fault instance.

**Table A-2: Electrical circuit parameters of commercial SFIGs and their contribution to 3-phase fault at terminals [4]**

No.	Manufacturer	P (MW)	$R_s$ (p.u.)	$X_s$ (p.u.)	$R_r$ (p.u.)	$X_r$ (p.u.)	$X_m$ (p.u.)	$I_f$ (p.u.) 3 <sup>rd</sup> cycle	$I_f$ (p.u.) 5 <sup>th</sup> cycle
1	Nordex	1	0.0062	0.0787	0.0092	0.0547	3.642	1.95	0.81
2	Negmicon	1.5	0.0227	0.0795	0.0156	0.0597	3.755	0.82	0.2
3	Negmicon	1	0.0225	0.173	0.008	0.13	3.428	1.84	1.31
4	WindWorld	0.6	0.0197	0.1271	0.0089	0.0956	4.667	2.01	1.21
5	Bonus	0.6	0.0065	0.0894	0.0093	0.1106	3.887	1.99	1.1
6	Bonus	1	0.0062	0.1362	0.0074	0.1123	3.911	2.16	1.48
7	Vestas	1.66	0.0077	0.0697	0.0062	0.0834	3.454	2.93	1.75

For asymmetrical faults, machine’s behaviour is different because in such faults, magnetic field is provided for the IG by the healthy phase(s). In fact, during the asymmetrical faults, higher voltages are induced in the rotor [5], and machine has non-zero steady state current. As an example, Figure A-5 shows the ac components of the stator’s currents of the SFIG for a single-phase solid fault at phase a, and Figure A-6 shows their RMS values.

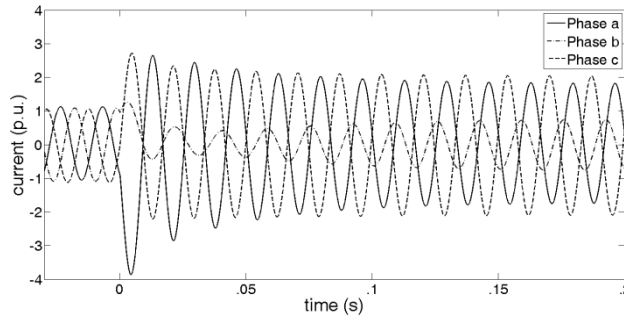


**Figure A-5: ac components of SCIG’s currents during 1-phase fault at phase a**

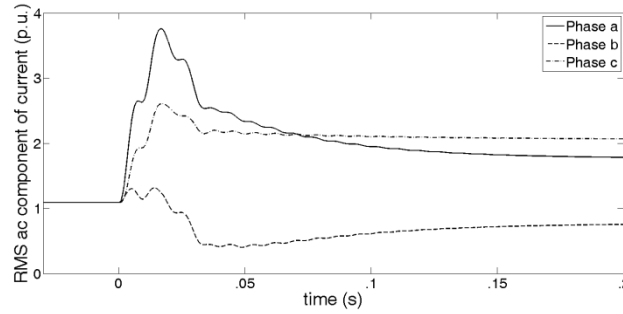


**Figure A-6: RMS ac components of SCIG's currents during 1-phase fault at phase *a***

According to Figure A-5 and Figure A-6, for Line-to-Ground (LG) fault, the ac component of current at the faulty phase increases up to 4 p.u. in the first cycle, and then decreases to the steady state value about 2 p.u. after the third cycle.

### A.1.2 Doubly-Fed Induction Generator (DFIG)

Figure A-7 shows a DFIG with its crowbar protection. According to this figure, this type of IG has a wound rotor which is connected to the distribution system through power electronics converters. With this structure, the DFIG is able to operate at the speed range from -30% to +30%. Besides, the power electronics provide the generator with the ability to control the reactive power independent to its active power. Due to these advantages, almost all IGs manufactured these days to be used in conjunction with wind turbines are DFIGs.

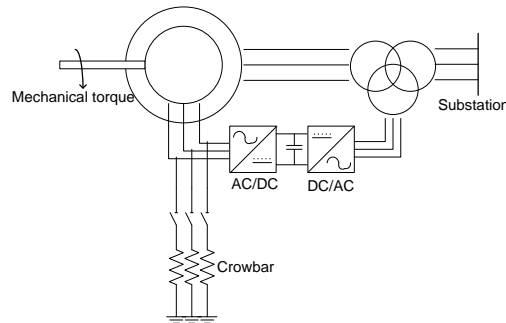


**Figure A-7: DFIG with its crowbar protection**

During the faults in the generator's vicinity, the rotor's winding experiences an excessive current which can damage the machine-side power electronics converter. In order to avoid this risk, the power converter's switches are blocked during such faults, and the rotor is grounded through crowbar resistors. As a result,

## Appendix A: Fault Current Contribution of Induction-Machine DGs

the DFIG's behaviour during the fault is completely similar to the SFIG's behaviour with large external rotor resistance. The Simulation results confirm this idea. Figure A-8 and Figure A-9 the RMS ac component of the DFIG's current during a 3-phase fault at its terminals for slips of +20% and -20%, respectively. Comparison between these figures and Figure A-4 shows that regardless of operating slip, DFIG's response to fault is similar to the wound rotor SFIG's response when it operates at a relatively high slip (high rotor resistance).

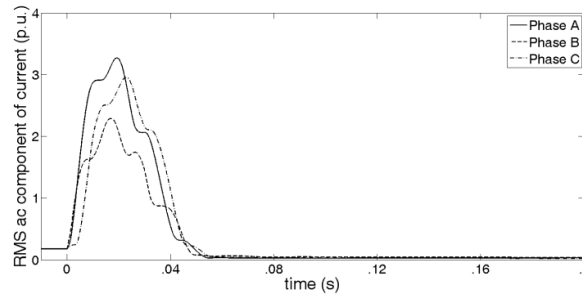


**Figure A-8: RMS ac component of DFIG's current during 3-phase fault at its terminals (Slip=+20%)**

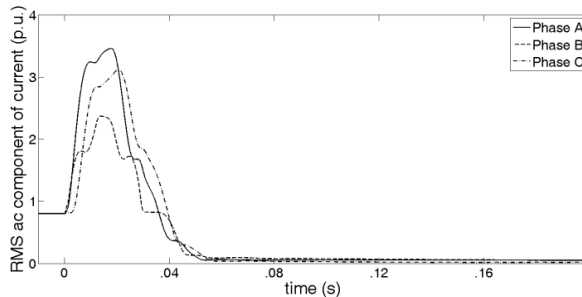


**Figure A-9: RMS ac component of DFIG's current during 3-phase fault at its terminals (Slip=-20%)**

In order to achieve a general conclusion about contribution of DFIGs to 3-phase fault currents, Table A-2 has been re-generated under the assumption that IGs are DFIG this time, and the crowbar resistance is twice the rotor's resistance. As this table reveals, contribution of all the generators to the fault current at the third cycle is less than .7 p.u., and in the 5<sup>th</sup> cycle, they have almost no contribution to the fault current. Also, the comparison between Table A-2 and Table A-3 shows that the crowbar operation highly accelerates the damping of generator's current during the fault.

**Table A-3: Electrical circuit parameters of commercially available IGs [4] and their contribution to 3-phase fault at terminals when considered as DFIG**

No.	Manufacturer	P (MW)	$R_s$ (p.u.)	$X_s$ (p.u.)	$R_r$ (p.u.)	$X_r$ (p.u.)	$X_m$ (p.u.)	$I_f$ (p.u.) 3 <sup>rd</sup> cycle	$I_f$ (p.u.) 5 <sup>th</sup> cycle
1	Nordex	1	0.0062	0.0787	0.0092	0.0547	3.642	0.14	0.01
2	Negmicon	1.5	0.0227	0.0795	0.0156	0.0597	3.755	0.01	0.00
3	Negmicon	1	0.0225	0.173	0.008	0.13	3.428	0.66	0.24
4	WindWorld	0.6	0.0197	0.1271	0.0089	0.0956	4.667	0.44	0.1
5	Bonus	0.6	0.0065	0.0894	0.0093	0.1106	3.887	0.34	0.06
6	Bonus	1	0.0062	0.1362	0.0074	0.1123	3.911	0.69	0.224
7	Vestas	1.66	0.0077	0.0697	0.0062	0.0834	3.454	0.63	0.14

## A.2 Findings from an experimental research work

In this sub-section, the results of experimental short circuit tests on an IG are provided to confirm the results achieved in previous sub-sections. In [6], 3-phase short circuit tests were performed at the terminals of a 415 V 7.5 kW IG in both SFIG and DFIG modes. Figure A-10 and Figure A-11 show the responses of SFIG and DFIG to the fault, respectively [6].

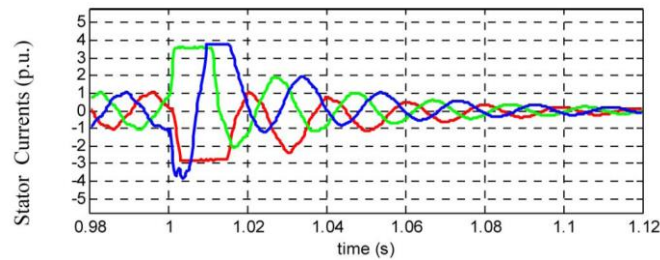


**Figure A-10: SFIG's 3-phase current during an experimental 3-phase fault at its terminals**

[6]

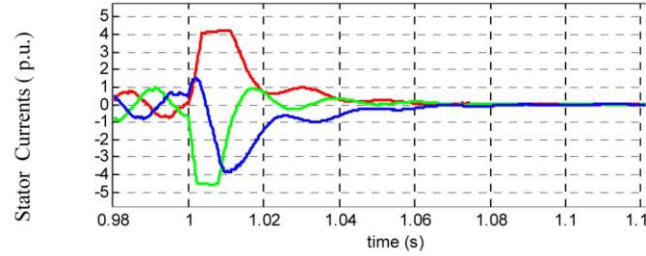


**Figure A-11: DFIG's 3-phase current during an experimental 3-phase fault at its terminals [6]**

As Figure A-10 reveals, SFIG's current reaches up to 4 p.u. in the first cycle after the beginning of fault. However, it decreases quickly so that in the third cycle it is less than 1 p.u. On the other hand, for DFIG (Figure A-11) the current decreases below 1 p.u. in the second cycle after the fault, and in the third cycle, it is almost zero. These results show agreement with the analytical and simulated results. The slight difference is that the simulated waveforms have higher peaks and are smoother than experimental waveforms which is due to neglecting magnetic saturation in simulations.

From the mathematical analysis, simulation and experimental results provided in sub-sections 4.1 and 4.2 it can be concluded that SFIG with no external rotor resistance has the highest peak of fault current and the longest transient time constant (slowest damping and widest contribution time window) in comparison to other IGs. Consequently, in the next section, SFIG is used to determine the impact of IG on the O.C. protection coordination.

### **A.3 Impact on the protection coordination**

In this section, contribution of SFIG, as the worst case, to phase-to-phase and phase-to-ground faults in the distribution system is studied and its impact on the O.C. protection is analyzed. To do so, the sample 25 kV distribution system shown in Figure 4-5 was simulated again. This time, the SMDG was replaced by the SFIG with the parameters tabulated in Table A-1. The protection system and its settings are similar to those presented in 4.3.1.

### A.3.1 Phase-to-phase faults

Similar to the SMDG of the case study presented in 4.3.1, when a SFIG is added upstream of B2, it is suspected to contribute to the fault and increase the fault current which flows through the protection devices. This increase may cause miscoordination between B1 and B2. As an example, consider a fault at F3. When there is no DG, the current through B2 is 4187A which leads to the operation of its short-time delay element, while the current through B1 is 4190A which results in operation of its inverse-time relay. However, when the SFIG is embedded, if it increases the fault current at F3 above 4440A (pick-up current of B1's instantaneous relay), both B1 and B2 will operate simultaneously, and the whole feeder is de-energized.

In order to examine the possibility of such miscoordination, a 9MW SFIG (90% of total load on the feeder) was embedded upstream of B2 (arbitrarily at the substation S) and its contribution to different phase-to-phase faults at F3 were determined. Figure A-12 shows the effect of the SFIG on the 3-phase fault current, and Figure A- 13 shows its effect on the phase *a* to phase *b* fault current.

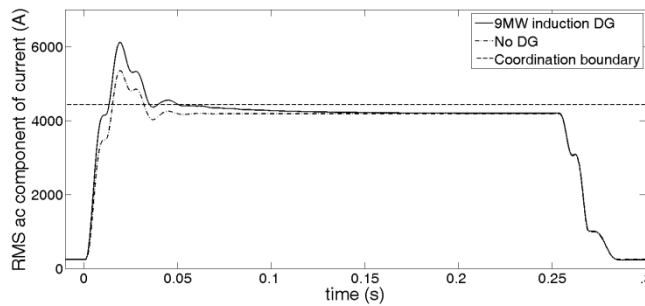


**Figure A-12: Impact of 9MW SCIG on 3-phase fault current**

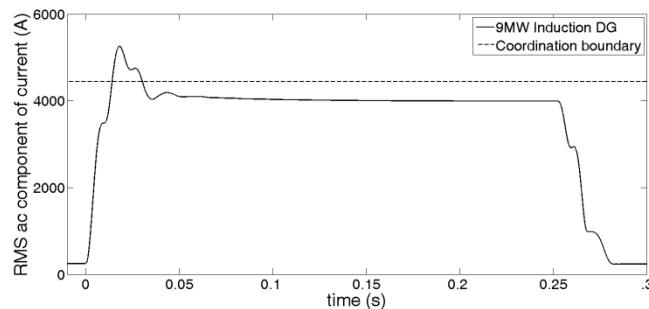


**Figure A- 13: Impact of 9MW SCIG on phase *a*-to-phase *b* fault current**

As both figures illustrate, the fault current decreases below the coordination boundary in less than .05 sec. which means that the coordination maintains in both cases, and the SFIG has no impact on the coordination. It is due to fast damping of the SFIG’s fault current. However, in this case, the SFIG can cause miscoordination at higher capacities, or if the short-time delay elements’ operation time are set below .05 sec.

### A.3.2 Phase-to-ground faults

Table A-4 shows the LG fault current at F3 for different scenarios, and its increment due to the insertion of 9MW SFIG. According to this table, in most cases, in contrast to what was expected, the SFIG decreased the single phase to ground fault few percent. Only in four scenarios in which substation transformer (Ts) at low voltage side has Yg connection, the SFIG has positive contribution to fault, and its maximum contribution is 6.7%.

**Table A-4: Contribution of SCIG to LG fault**

Ts	Fault current (A) (No DG)	Fault current (A) (9MW IG, TIG: DYg)	Incremental current due to IG (%)	Fault current (A) (9MW IG, TIG: YgYg)	Incremental current due to IG (%)
<b>YY</b>	678	665	-1.92	667	-1.62
<b>YD</b>	678	665	-1.92	667	-1.62
<b>YYg</b>	693	676	-2.45	678	-2.16
<b>DY</b>	678	665	-1.92	667	-1.62
<b>DD</b>	678	665	-1.92	667	-1.62
<b>DYg</b>	5528	5900	6.73	5753	4.07
<b>YgYg</b>	3973	4153	4.53	4082	2.74
<b>YgY</b>	678	665	-1.92	666	-1.77
<b>YgD</b>	678	665	-1.92	667	-1.62

In order to investigate the impact of the SFIG on the coordination consider the worst condition in which it has 6.7% contribution, and imagine that B1 and B2 are equipped with inverse O.C. relays (with IEC 60255 characteristic equation) for ground fault protection with the settings tabulated in Table A-5. In this case, when there is no DG, for phase-to-ground fault at F3, B2 operates at .073 sec. and

## Appendix A: Fault Current Contribution of Induction-Machine DGs

B1 operates at .32 sec., and there is a .25 sec. interval between main and back-up protection devices' operation. When a 9MW SCIG is embedded at substation, the ground fault current is increased from 5528A to 5900A. In this case, B2 as the main protection operates at .0728 and B1 as the back-up operates at .319 sec, and still there is a .246 sec. interval between the main and back-up protection, and the coordination maintains.

**Table A-5: ground fault relays' settings**

	<b>I<sub>pick-up</sub> (A)</b>	<b>TSM</b>
<b>B1</b>	80	.05
<b>B2</b>	60	.2

### **A.4 Conclusion**

In this section, the contribution of IMDGs to the fault current was studied, and their impact on the O.C. protection coordination was investigated. The results are summarized as follows:

1. In the first cycle after the beginning of symmetrical faults, IG's current reaches to 6p.u. However, it decreases to zero in the next cycles. During asymmetrical faults, the IG's output current is higher than its rated current with a peak up to 4 p.u. in the first three cycles and the steady state value of 2 p.u. in the next cycles.
2. Due to the short contribution time window in case of phase-to-phase faults, the IG has no impact on O.C. coordination unless there are instantaneous or short-time delay elements with the operation time less than .05 sec. (three cycles) in the protection system, and the IG penetration level is so high, which is not common.
3. In case of phase-to-ground faults, simulations showed that the maximum contribution of the SFIG at very high penetration levels is limited to 7% of original fault current which is not sufficient to cause miscoordination between the main and back-up inverse O.C. ground fault relays.

## Appendix A: Fault Current Contribution of Induction-Machine DGs

4. Due to their advantages, DFIGs become more and more popular, and almost all IGs being installed in the wind plants these days are DFIGs. Besides, it was shown that, due to crowbar protection, DFIG's contribution to the fault current is negligible. So, one can say that embedding IGs in the distribution system is not a concern from the protection coordination point of view.

# **Appendix B:**

## **Fault Current Contribution of Permanent Magnet Synchronous Generators**

Permanent Magnet Synchronous Generators (PMSGs) have been used in three DG applications: wind turbines with full-scale converters, micro-turbines and micro hydro power plants. In the first two applications, PMSG is connected to the grid through an inverter. Consequently, DG's contribution to the grid faults depends on its inverter's control and protection (see Section 3) rather than the PMSG's parameters. In contrast, in the third application, PMSG is directly connected to the grid and directly responds to the grid faults. The main aim of this section is to investigate the response of the direct-connected PMSG to the fault and compare its contribution to fault current with the contribution of regular WFSG which was studied in previous section.

In following paragraphs, an analytical method to calculate PMSG's fault current is presented. Next, comparison between WFSG's and PMSG's responses to faults is presented. Then, a method to estimate the PMSG's contribution to faults for O.C. coordination studies is provided which is followed by the conclusion.

### B.1 PMSG's fault current

Figure B-1 shows the equivalent  $0dq$  circuit of a PM synchronous machine [7]. As this figure reveals, PM is modeled as a  $d$ -axis magnetization current ( $i_m$ ).

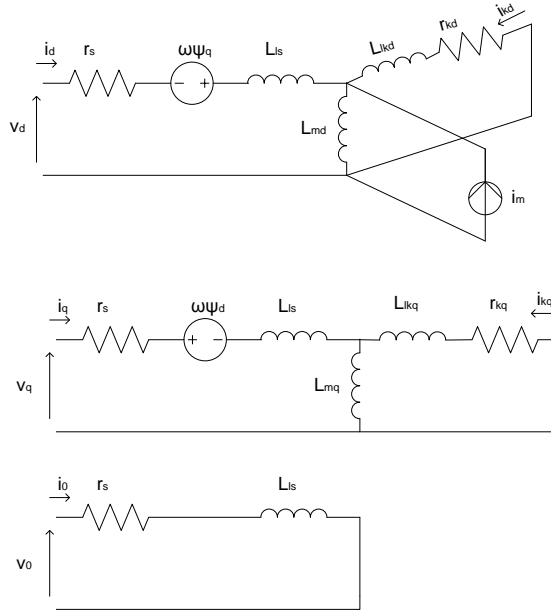


**Figure B-1: Equivalent  $0dq$  circuit of a PM synchronous machine**

According to Figure B-1  $0dq$  voltage equations can be written as follows [7]:

$$\begin{cases} v_q = r_s i_q + \frac{d\psi_q}{dt} + \omega\psi_d \\ v_d = r_s i_d + \frac{d\psi_d}{dt} - \omega\psi_q \\ v_0 = r_s i_0 + \frac{d\psi_0}{dt} \end{cases} \quad (\text{B- 1})$$

where

$$\begin{cases} \psi_q = L_q i_q + L_{mq} i_{kq} \\ \psi_d = L_d i_d + L_{md} i_{kd} + L_{md} i_m \\ \psi_0 = L_s i_0 \end{cases} \quad (\text{B- 2})$$

and

## Appendix B: Fault Current Contribution of Permanent Magnet Synchronous Generators

$$\begin{cases} L_q = L_{mq} + L_{ls} \\ L_d = L_{md} + L_{ls} \end{cases} \quad (\text{B- 3})$$

During a three-phase solid fault at machine's terminal, current can be obtained by equating  $0dq$  voltages with zero. Then, by transforming  $0dq$  currents,  $abc$  currents are obtained. By doing so, AC fundamental component of PMSG's current at phase a can be determined as follows:

$$i_a = U_{mq} \left[ \frac{1}{X_d} + \left( \frac{1}{X_d''} - \frac{1}{X_d} \right) e^{-\frac{t}{T_d}} \right] \cos(\omega t + \theta_0) - U_{md} \left[ \frac{1}{X_q} + \left( \frac{1}{X_q''} - \frac{1}{X_q} \right) e^{-\frac{t}{T_q}} \right] \sin(\omega t + \theta_0) \quad (\text{B- 4})$$

where  $\theta_0$  is the angle between the field and phase a coils' axis at the fault instance and:

$$\begin{aligned} X_d'' &= X_{ls} + \frac{X_{md} X_{kd}}{X_{md} + X_{kd}} \\ X_q'' &= X_{ls} + \frac{X_{mq} X_{kq}}{X_{mq} + X_{kq}} \\ T_d'' &= \frac{1}{\omega r_{kd}} \left( X_{kd} + \frac{X_{md} X_{ls}}{X_{md} + X_{ls}} \right) \\ T_q'' &= \frac{1}{\omega r_{kq}} \left( X_{kq} + \frac{X_{md} X_{ls}}{X_{md} + X_{ls}} \right) \end{aligned} \quad (\text{B- 5})$$

As (B- 4) reveals, PMSG's response can be divided into two periods: sub-transient and steady state.

### B.2 Comparison of PMSG's and WFSG's fault currents

The first and most important difference between PMSG and WFSG is that in the first one the magnetic field is provided by PMs, while in the latter one the magnetic field is provided by a field winding. As a result, an additional time constant  $T'_d$  and an additional operational reactance  $X'_d$  appear in the WFSG's response to fault (see (B- 6)).

## Appendix B: Fault Current Contribution of Permanent Magnet Synchronous Generators

$$i_a = U_{mq} \left[ \frac{1}{X_d} + \left( \frac{1}{X_d'} - \frac{1}{X_d} \right) e^{-\frac{t}{T_d'}} + \left( \frac{1}{X_d''} - \frac{1}{X_d'} \right) e^{-\frac{t}{T_d''}} \right] \cos(\omega t + \theta_0) - U_{md} \left[ \frac{1}{X_q} + \left( \frac{1}{X_q'} - \frac{1}{X_q} \right) e^{-\frac{t}{T_q'}} \right] \sin(\omega t + \theta_0) \quad (\text{B- 6})$$

Comparison between (B- 4) and (B- 6) reveals that the WFSG's response to fault is divided into three periods (instead of two) which are: sub-transient, transient and steady state.

The second difference is that the sub-transient time constant of PMSG could be so short that after one or two cycles, PMSG's fault current reaches its steady state [8]. Moreover, operational reactances of PMSG are typically smaller than the operational reactances of WFSG. In summary:

$$X_{d,PMSG}'' < X_{d,WFSG}'' < X_{d,WFSG}' < X_{d,PMSG}' < X_{d,WFSG} \quad (\text{B- 7})$$

$$X_{q,PMSG}'' < X_{q,WFSG}'' < X_{q,PMSG}' < X_{q,WFSG}' \quad (\text{B- 8})$$

$$T_{d,PMSG}'' < T_{d,WFSG}'' < T_{d,WFSG}' \quad (\text{B- 9})$$

$$T_{q,PMSG}'' < T_{q,WFSG}'' \quad (\text{B- 10})$$

Typical time constants and operational reactances for PMSG and WFSG are collected and tabulated in Table B-1 [8]-[10]:

**Table B-1: Typical time constants and reactances of synchronous generators [8]-[10]**

Parameter	Typical value for PMSG	Typical value for WFSG
$X_d$	0.45 (p.u.)	1.2 (p.u.)
$X_d'$	-	0.35 (p.u.)
$X_d''$	0.13 (p.u.)	0.25 (p.u.)
$X_q$	0.45 (p.u.)	0.9 (p.u.)
$X_q''$	0.13 (p.u.)	0.28 (p.u.)
$T_d'$	-	1.4 sec.
$T_d''$	8 m.sec.	160 m.sec.
$T_q''$	8 m.sec.	160 m.sec.

## Appendix B: Fault Current Contribution of Permanent Magnet Synchronous Generators

According to (B- 4), (B- 6) and Table B-1, for generators with the same size, PMSG has higher output than WFSG in the first one or two cycles after the fault (sub-transient response). Next, PMSG's current decrease to its steady-state value, while WFSG's current starts its transient period. Since  $X_{d,WFSG}' < X_{d,PMSG}$ , for several cycles WFSG's current is higher than PMSG's current. Finally, WFSG also reaches its steady state, and because  $X_{d,PMSG} < X_{d,WFSG}$ , it has lower output current than PMSG's current. For further illustration, one PMSG and one WFSG were simulated in Matlab/Simulink with the parameters tabulated in Table B-1. Figure B-2 shows the output currents of these machines during a three-phase solid fault at terminals, and Figure B-3 shows the RMS ac component of these currents.

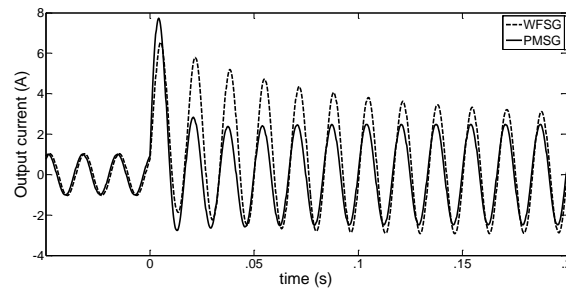


**Figure B-2: Current at phase a for three-phase solid fault at terminals**

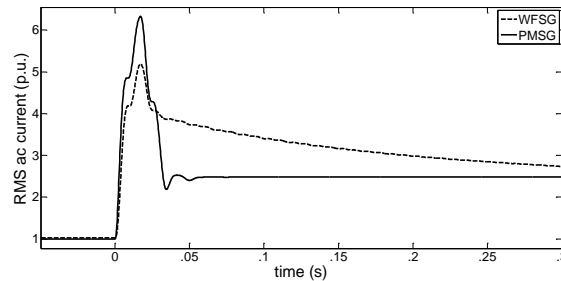


**Figure B-3: RMS ac component of current at phase a for three-phase solid fault at terminals**

As Figure B-3 demonstrates, during the first two cycles, fault current of PMSG is higher than that of the WFSG. Next, after the second cycle, sub-transient responses of generators disappeared, and PMSG's current reached its steady-state value around 2.5 p.u. while transient response of WFSG started with almost 4 p.u. which gradually decreased.

### B.3 Estimation of PMSG's contribution to fault

As Figure 2-3 revealed in Chapter 2, almost all O.C. devices operate after 0.03 sec. (2 cycles after the beginning of fault). Besides, in previous section it was shown that PMSG's sub-transient response disappears in two cycles. As a result, for O.C. coordination studies in distribution system, sub-transient part of machine's response can be neglected. In this case, PMSG's current can be estimated as:

$$i_a = U_{mq} \left[ \frac{1}{X_d} \right] \cos(\omega t + \theta_0) - U_{md} \left[ \frac{1}{X_q} \right] \sin(\omega t + \theta_0) \quad (\text{B- 11})$$

The RMS value of (B- 11) is as follows:

$$i_{a,RMS} = \sqrt{\left[ \frac{U_{mq}}{X_d} \right]^2 + \left[ \frac{U_{md}}{X_q} \right]^2} \quad (\text{B- 12})$$

Now, by neglecting machine's saliency, (B- 12) could be simplified as:

$$i_{a,RMS} = \frac{1}{X_d} \sqrt{U_{mq}^2 + U_{md}^2} = \frac{U}{X_d} \quad (\text{B- 13})$$

where  $U$  is the machine's no-load voltage, and can be estimated as follows (by assuming rated output current at unity power factor during pre-fault and neglecting stator resistance and rotor saliency):

$$U = \sqrt{1 + X_d^2} \quad (\text{B- 14})$$

Now, from (B- 13) and (B- 14):

$$i_{a,RMS} = \sqrt{1 + \left(\frac{1}{X_d}\right)^2} \quad (\text{B- 15})$$

From (B- 15), RMS ac component of current for the PMSG simulated in previous part is obtained as 2.437 p.u. which is close to the simulation result 2.484 p.u.

In order to compare the impact of PMSG and WFSG on the O.C. coordination, it is necessary to consider the O.C. devices' operation time frames. From Table B-1 and Figure 2-3 it can be concluded that the operation of the O.C.

## Appendix B: Fault Current Contribution of Permanent Magnet Synchronous Generators

devices normally coincides with the transient response of WFSG. This part of WFSG's response has a decaying trend and can be estimated as follows:

$$i_{a,RMS} = U \left[ \frac{1}{X_d} + \left( \frac{1}{X_d'} - \frac{1}{X_d} \right) e^{-\frac{t}{T_d'}} \right] \quad (\text{B- 16})$$

As a result (B- 16) should be compared with (B- 13).

If inverse and/or very inverse O.C. devices are involved in the protection ( $t > 3$ ), it is hard to compare (B- 13) and (B- 16). However, Figure B-3 reveals that in this period, the contribution of PMSG and WFSG are almost the same.

If extremely inverse or short-time delay elements are involved in the coordination (scenarios in which miscoordination is more likely to happen),

$e^{-\frac{t}{T_d'}} \approx 1$  and consequently for WFSG:

$$i_{a,RMS} = \frac{U}{X_d'} \quad (\text{B- 17})$$

where  $U$  can be estimated by (B- 14). As a result:

$$\frac{i_{RMS,PMSG}}{i_{RMS,WFSG}} = \frac{\sqrt{1 + X_{d,PMSG}^2}}{\sqrt{1 + X_{d,WFSG}^2}} \times \frac{X_{d,WFSG}'}{X_{d,PMSG}} \quad (\text{B- 18})$$

Now, by inserting typical values from Table 1, in such time frame

$\frac{i_{RMS,PMSG}}{i_{RMS,WFSG}} = 0.6$ . In other words, the contribution of PMSG is 60% of the

contribution of WFSG with the same size.

### B.4 Limiting PMSG's fault current

In previous sections, it was shown that the PMSG's response to fault can be divided into two periods. The sub-transient response is too quick to impact the O.C. coordination. As a result, this part focuses on limiting the steady state response of PMSG.

## Appendix B: Fault Current Contribution of Permanent Magnet Synchronous Generators

By substituting (B- 19) and (B- 20) in (B- 17), it is shown that the ac component of PMSG's current is equal to the ratio of its  $d$ -axis flux to its inductance.

$$U = \omega\psi_d \quad (\text{B- 19})$$

$$X_d = \omega L_d \quad (\text{B- 20})$$

$$i_{a,RMS} = \frac{\psi_d}{L_d} \quad (\text{B- 21})$$

As (B- 21) reveals, a large inductance can restrict PMSG's current during a fault. So, one way to limit PMSG's current is to consider a large  $L_d$  for machine, during design procedure. Another way is weakening its flux during the fault. Flux adjustment requires an additional mechanism to be implemented in the machine. This mechanism could be either utilizing an auxiliary field winding or a mechanical mechanism. These machine's fault current limiting streams are reviewed in the following sections.

### B.4.1 PM machines with large leakage inductance

The idea of designing PM machines with large inductance has been proposed and used in designing fault-tolerant machines. These machines should meet specific requirements such as high power density and high reliability to be appropriate for aerospace and automotive applications [11]-[14]. In fault-tolerant PM machines, using PM ensures high power density. Besides, fault current should be limited to the rated current to prevent machine's damage during the short circuit which is a reliability requirement.

In [15],[16] the PM machine's short circuit current has been calculated as follows:

$$i_a(t) = \frac{\omega\psi}{Z_{sc}} \sin(\omega t - \phi_{sc}) \quad (\text{B- 22})$$

## Appendix B: Fault Current Contribution of Permanent Magnet Synchronous Generators

Where  $\omega\psi\sin(\omega t - \phi_{sc})$   $\omega\psi\sin(\omega t - \phi_{sc})$  is the back EMF due to the PM flux linkage  $\psi$ , and  $Z_{sc} = \sqrt{R^2 + (\omega L)^2}$  is the phase impedance. Since in practice  $R \ll \omega L$ , magnitude of fault current can be estimated as follows:

$$i_{a,RMS} = \frac{\psi}{L} \quad (\text{B- 23})$$

which is consistent with the result achieved in previous section. Based on (B- 23), [11]-[24] have concluded that a fault tolerant machine should be designed so that its per-unit inductance is equal to its per-unit flux linkage. In addition, mutual inductance between phases should be negligible to avoid fault propagation [11]. So, this large inductance is mainly leakage inductance.

Although it may sound difficult to achieve a PM machine design which provides large leakage inductance, in [13] it has been shown that even for small PM machines large leakage inductance is easily achievable. According to [17], the desired leakage inductance can be gained by controlling depth and width of slot opening.

Nevertheless, such design associates with a major disadvantage which is increase in machine's flux that requires wider stator teeth [13]. Additional tooth width and deeper reactance slots can increase machine weight by 15% [19].

### **B.4.2 PM machines with auxiliary excitation**

One way to control the PMSG's flux is to add an auxiliary field winding with adjustable supply to regulate the total air-gap flux. These PM machines with additional field windings are called Hybrid Excitation Synchronous Machines (HESMs). In following paragraphs, HESMs are divided into two categories, based on the location of auxiliary winding, and advantages and disadvantages of them are reviewed.

#### **a. PM machines with auxiliary excitation on the rotor**

This category includes the PMSGs with auxiliary field winding mounted on their rotors. Figure B-4 shows a simple example of this type. As it can be seen in

## Appendix B: Fault Current Contribution of Permanent Magnet Synchronous Generators

this figure, rotor is separated to two independent parts, PM and wound field [25]. Each part of the rotor induces a back EMF, and depending on the direction of field current, these two EMFs can either boost or cancel each other.

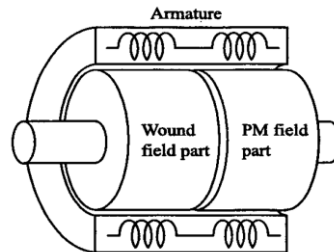


**Figure B-4: HESM with separated rotors on the same shaft [21]**

There are also other types of HESMs in which rotor is not separated to two distinguished parts, i.e. both field winding and PMs are mounted on the same rotor part. These machines have more complicated rotor structures, and depending on the path of the flux generated by the auxiliary winding, they are classified into two subcategories [22]:

- Series flux path
- Parallel flux path

In HESMs with series flux path, the flux generated by auxiliary winding passes through PMs. Series flux HESMs have simpler structure than parallel ones, and good flux weakening capability up to 50% [22]. However, there is a risk for irreversible demagnetization [23].

On the other hand, in HESMs with parallel flux path, the flux generated by PM and the one generated by auxiliary field winding have different paths. In contrast to series flux path HESMs, there is a wide variety of structures for these machines [23]. However, these structures are more complicated than series ones either for analysis or for manufacturing [22].

Regardless of being series or parallel flux path, HESMs with field winding on the rotor, has a major drawback. These machines require brushes and slip rings or rotary diodes to supply the auxiliary winding mounted on rotor.

**b. PM machines with auxiliary excitation on the stator**

This category includes machines in which PMs are mounted on the rotor, while the auxiliary field winding is embedded in the stator. Major advantage of such design is that these machines do not require brushes and slip rings. Nevertheless, both rotor and stator structures are complicated in these machines.

Figure B-5 shows the structure of the consequent-pole PM machine proposed in [26]. As it can be seen, rotor includes both iron poles and magnets. Besides, stator is divided into two parts, and a circumferential DC field winding is embedded between these two parts. The flux provided by PMs combines with the flux provided by auxiliary winding in the air-gap. Depending on the direction of excitation current, flux generated by winding can boost or weaken the PM flux. There is no risk of demagnetization, and low Amp-turn is required for air-gap flux control [26]. However, complicated structure causes manufacturing problems [26].

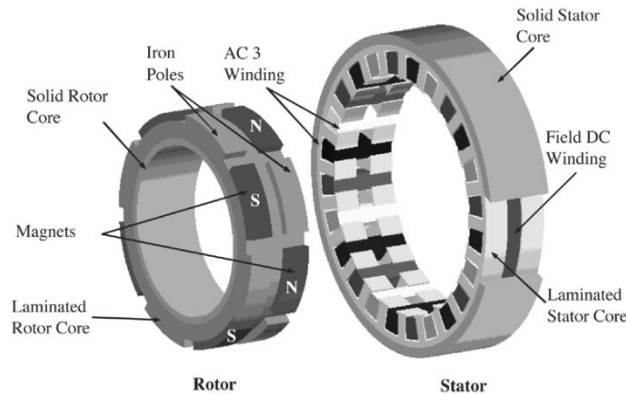


**Figure B-5: Consequent-pole permanent magnet machine [26]**

Regardless of the location of auxiliary winding, all HESMs suffer from the following disadvantages:

- Embedding an auxiliary field winding increases machine’s weight, and hence, decreases machine’s power density.
- An independent power source and converter are needed to supply DC field.

## Appendix B: Fault Current Contribution of Permanent Magnet Synchronous Generators

- In contrast to regular PMSGs, HESMs have complicated structures which cause associated manufacturing difficulties.
- The dynamic behaviour of HESMs during the faults is not available in the literature, and it is not determined whether or not the flux regulation mechanism is fast enough to restrict machine's contribution to fault.

### B.4.3 PM machines with mechanically adjustable flux

Machines in this category have variable mechanical structures. These machines have at least one additional mobile part, in comparison to regular PMSGs, which regulate the flux by its displacement. These mobile parts weaken the flux by adding a leakage path or misaligning the flux path [27]. For further illustration, two examples of machines in this category are introduced in the following paragraphs.

Figure B-6 shows a PMSG with flux adjustment capability [28]. As it can be seen in this figure, two movable flux-shortening iron plates are placed in both sides of the rotor. The air-gap flux can be regulated by adjusting the distance between these iron plates and the PM rotor. When flux weakening is needed, the iron plates are pushed toward the PM rotor by actuators. As a result, flux leakage paths are provided by these plates, and the air-gap flux is reduced.

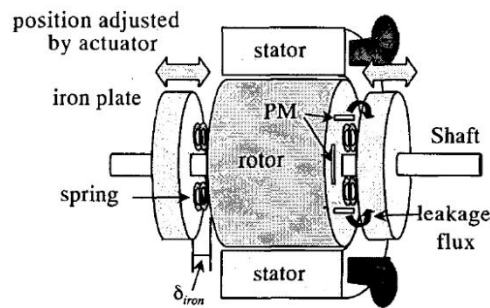


**Figure B-6: Variable flux PMSG with movable flux-shortening iron plates [28]**

As another example, Figure B-7 [29] shows the structure of a mechanically adjustable-flux PMSG when it works in full air-gap flux mode [29]. As it can be seen in this figure, the machine has two separated PM rotors mounted on a screw

## Appendix B: Fault Current Contribution of Permanent Magnet Synchronous Generators

thread shaft. One of these rotor parts can be misaligned by an actuator. In this case, less flux linkage is experienced by the stator. Figure B-8 shows this machine when the air-gap flux is nullified [29].

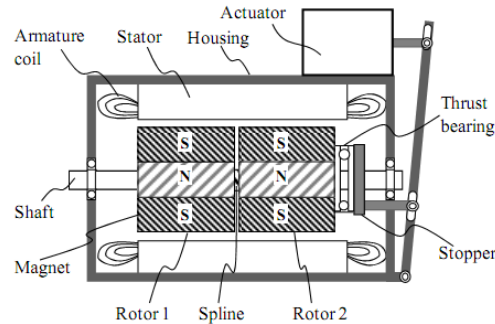


**Figure B-7: Variable flux PMSG with two rotors on a screw thread shaft in maximum air-gap flux operation mode [29]**

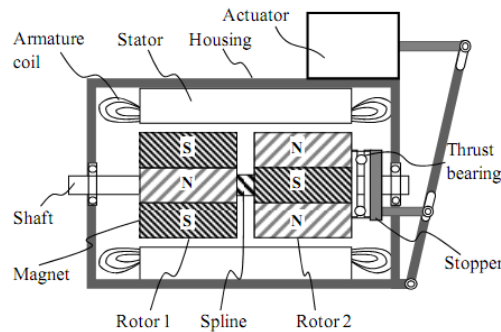


**Figure B-8: Variable flux PMSG with two rotors on a screw thread shaft in nullified air-gap flux operation mode [29]**

Regardless of the adjusting mechanism, mechanically adjustable-flux PMSGs suffer from the following disadvantages:

- These machines usually have more complicated structures than regular PMSGs.
- Due to the fact that the flux adjustment requires displacement of mechanical parts, these machines have relatively long response time.
- Actuators and other additional parts require maintenance, and lower the machine's reliability.

## B.5 Conclusion

The PMSG's response during the fault and its contribution to the fault current were studied in this section. It was shown that:

1. The response of these machines to fault is divided into two periods: sub-transient which disappears after the second cycle of fault, and the steady state which coincides with the operation of O.C. devices.
2. In the first two cycles after the fault, PMSG has higher contribution than WFSG. Next, PMSG starts its steady-state response. In this period, which coincides with the typical operation interval of O.C. devices, the contribution of PMSG is lower than the contribution WFSG at the same size.
3. PMSG's are relatively small machines with the contribution up to 250% their rated current. This contribution is remarkably less than the contribution of WFSGs in scenarios where miscoordination is more likely to happen. As a result, PMSGs may not be a concern for O.C. protection coordination.
4. Amongst all the PMSG's fault current limiting methods, is the most suitable one, due to the following reasons:
  - It does not require actuator or brushes and slip rings. So, it does not impact the machine's reliability and does not demand for additional maintenance.
  - Limited fault current is an inherent property in machines with enlarged leakage reactance, and it does not need fault detection and trigger mechanisms and is not affected by response time, delay, etc.
  - Enlarging PMSG's leakage reactance can be achieved by choosing suitable values for machine design parameters and it does not need complicated rotor and stator structures.

## Appendix B: Fault Current Contribution of Permanent Magnet Synchronous Generators

- This method does not need additional power source/converter to supply auxiliary winding or actuators.
- The only penalty of large PMSG's leakage reactance is an increase in machine's weight up to 15%.

## References of Appendices

- [1] E. Muljadi, N. Samaan, V. Gevorgian, J. Li and S. Pasupulati, "Short Circuit Current Contribution for Different Wind Turbine Generator Types," IEEE Power and Energy Society General Meeting, 2010, pp. 1–8.
- [2] W. Freitas, C. M. Vieira, A. Morelato, L. C. P. da Silva, V. F. da Costa and F. A. B. Lemos, "Comparative Analysis Between Synchronous and Induction Machines for Distributed Generation Application," IEEE Trans. Power System, vol. 21, no. 1, pp 301-311, February 2006.
- [3] J. Morren and S. W. H. de Haan, "Short-Circuit current of Wind Turbines With Doubly Fed Induction Generator," IEEE Trans. Energy Conversion, vol. 22, no. 1, pp 174-180, March 2007.
- [4] A. G. G. Rodrigez, "Improvement of Fixed-Speed Wind Turbine Soft Starter Based On A Sliding Mode Controller," PhD Dissertation, Dept. Elect. Eng., Univ. of Seville, Seville, Spain, March 2006.
- [5] J. Lopez, E. Gubia, P. Sanchis, X. Roboam and L. Marroyo, "Wind Turbines Based on Doubly Fed Induction Generator Under Asymmetrical Voltage Dips," IEEE Trans. Energy Conversion, vol. 23, no. 1, pp 321-329, March 2008.
- [6] G. Pannell, D. J. Atkinson and B. Zahawi, "Analytical Study of Grid-Fault Response of Wind Turbine Doubly Fed induction Generator," IEEE Trans. Energy Conversion, vol. 25, no. 4, pp 1081-1091, December 2010.
- [7] C. Ong, Dynamic Simulation of Electric Machinery Using Matlab/Simulink, Upper Saddle River, NJ Prentice Hall, 1998
- [8] K. W. Klontz, T. J. E. Miller, M. I. McGlip, H. Karmaker, and P. Zhong, "Short-Circuit Analysis of Permanent-Magnet Generators," IEEE Trans. Industry Applications, vol. 47, no. 4, pp 1670-1680, 2011.
- [9] Test Procedures for Synchronous Machines IEEE Standard 115, 1994
- [10] E. W. Kimbark, Power System Stability, Piscataway, NJ: IEEE Press, 1995

- [11] N. Bianchi, S. Bolognani, and M. Dai Pre, "Design and tests of a fault-tolerant five-phase permanent magnet motor," in Proc. IEEE Power Electron. Spec. Conf., Jun. 2006, pp. 1–8.
- [12] N. Bianchi and S. Bolognani, "Strategies for the Fault-Tolerant Current Control of a Five-Phase Permanent-Magnet Motor," IEEE Trans. Industry Applications, vol. 43, no. 4, pp 960-971, 2007.
- [13] B. C. Mecrow, A. G. Jack, J. A. Haylock and J. Coles, "Fault-tolerant permanent magnet machine drives," IEE Proc.-Electr. Power Appl., Vol. 143, No. 6, pp. 431-436, November 1996.
- [14] T. Raminosa and C. Gerada, "A comparative study of permanent magnet - synchronous and permanent magnet - flux switching machines for fault tolerant drive systems," IEEE Energy Conversion Congress and Exposition, 12-16 Sept. 2010, pp. 2471-2478.
- [15] C. Bianchini, E. Fornasiero, T. N. Matzen, N. Bianchi, and A. Bellini, "Fault detection of a five-phase permanent-magnet machine," in Proc. 34th Annu. IEEE IECON, 2008, pp. 1200–1205.
- [16] J. Chai, J. Wang, K. Atallah, and D. Howe, "Performance comparison and winding fault detection of duplex 2-phase and 3-phase fault-tolerant permanent magnet brushless machines," in Conf. Rec. IEEE IAS Annu. Meeting, Sydney, Australia, Sep. 2007, pp. 566–572.
- [17] B.C. Mecrow, A. G. Jack, D. J. Atkinson, S. Green and G. J. Atkinson, "Design and Testing of a 4 Phase Fault Tolerant Permanent Magnet Machine for an Engine Fuel Pump", Electric Machines & Drives Conf., Vol. 2, June 2003, pp. 1301–1302.
- [18] N. Bianchi and M. Dai Prè, "Use of the star of slots in designing fractional-slot single-layer synchronous motors," Proc. Inst. Elect. Eng.—Elect. Power Appl., vol. 153, no. 3, pp. 459–466, May 2006.

- [19] J. A. Haylock, B.C. Mecrow, A. G. Jack and D. J. Atkinson, "Operation of fault tolerant machines with winding failures," in Proc. IEEE Int. Electr. Mach. and Drives Conf., 1997, pp. MC3/10.1–MC3/10.3.
- [20] B. Welchko, T. Jahns, W. Soong, and J. Nagashima, "Ipm synchronous machine drive response to symmetrical and asymmetrical short circuit faults," IEEE Transactions on Energy Conversion, vol. EC–18, Jun. 2003.
- [21] N. Naoe and T. Fukami, "Trial production of a hybrid excitation type synchronous machine," in Conf. Rec. IEEE-IEMDC, Cambridge, MA, Jun. 17–20, 2001, pp. 545–547.
- [22] R. Owen, Z.Q. Zhu, J.B. Wang, D. A. Stone, and I. Urquhart, "Review of variable-flux permanent magnet machines," Int. Conf. on Elec. Machines and Systems, 20-23 August, 2011, Beijing.
- [23] Y. Amara, L. Vido, M. Gabsi, E. Hoang, A. H. Ben Hamed, and M. Lécivain, "Hybrid excitation synchronous machines: Energy-efficient solution for vehicles propulsion," IEEE Trans. Veh. Technol., vol. 58, no. 5, pp. 2137–2149, Jun. 2009.
- [24] G. Henneberger, J. R. Hadji-Minaglou, and R. C. Ciorba, "Design and test of permanent magnet synchronous motor with auxiliary excitation winding for electric vehicle application," in Proc. Eur. Power Electron. Chapter Symp., Lausanne, Switzerland, Oct. 1994, pp. 645–649.
- [25] D. Fodorean, A. Djerdir, I. A. Viorel, and A. Miraoui, "A double excited synchronous machine for direct drive application—Design and prototype tests," IEEE Trans. Energy Convers., vol. 22, no. 3, pp. 656–665, Sep. 2007.
- [26] J. A. Tapia, F. Leonardi, and T. A. Lipo, "Consequent-pole permanentmagnet machine with extended field-weakening capability," IEEE Trans. on Industry Applications, vol. 39, No 6, pp. 1704-1709, Nov./Dec. 2003.

- [27] A. D. Akemakou and S. K. Phounsombat, "Electrical machine with double excitation, especially a motor vehicle alternator," U.S. Patent 6 147 429, Nov. 14, 2000.
- [28] H. Wang, Y. Wang, X. Liu, G. Cao and J. Fan, "Design and Performance Evaluation of Compound Permanent Magnet Generator With Controllable Air-gap Flux," IET Electr. Power Appl., 2011, Vol. 5, Iss. 9, pp. 684–690
- [29] L. Ma, M. Sanada, S. Morimoto, & Y. Takeda, "Advantages of IPMSM with adjustable PM armature flux linkage in efficiency improvement and operating range extension," Proceedings of the Power Conversion Conference, 2002. PCC Osaka 2002, vol.1, pp.136-141, 2002